High Temperature Phase Transitions of Actinide Dioxides

Robert Böhler

sierke

HIGH TEMPERATURE PHASE TRANSITIONS OF ACTINIDE DIOXIDES

HIGH TEMPERATURE PHASE TRANSITIONS OF ACTINIDE DIOXIDES

Proefschrift

ter verkrijging van de graad van doctor
aan de Technische Universiteit Delft,
op gezag van de Rector Magnificus prof. ir. K. C. A. M. Luyben,
voorzitter van het College voor Promoties,
in het openbaar te verdedigen op maandag 8 december 2014 om 12:30 uur

door

Robert BÖHLER

Diplom-Ingenieur, Universität Stuttgart
geboren te Karaganda, Kazachstan.

Dit proefschrift is goedgekeurd door de promotoren :

Prof. dr. H. T. Wolterbeek
Prof. dr. R. J. M. Konings

Samenstelling promotiecommissie:

Rector Magnificus,	voorzitter
Prof. dr. R. J. M. Konings,	Technische Universiteit Delft, promotor
Prof. dr. H. T. Wolterbeek,	Technische Universiteit Delft, promotor
Dr. D. Manara,	JRC, European Commission
Prof. dr. S. Bechta	Kungliga Tekniska högskolan Stockholm
Prof. dr. G. Pottlacher,	Technische Universität Graz
Prof. dr. B. J. Thijsse,	Technische Universiteit Delft
Dr. R. P. C. Schram,	NRG Petten
Prof. dr. P. Dorenbos,	Technische Universiteit Delft

An electronic version of this dissertation is available at
http://repository.tudelft.nl/

Bibliografische Information der Deutschen Nationalbibliothek

Die Deutsche Bibliothek verzeichnet diese Publikation in der Deutschen National-
bibliografie; detaillierte bibliografische Daten sind im Internet über http://dnb.ddb.de
abrufbar.

Robert Böhler
High Temperature Phase Transitions of Actinide Dioxides

CONTENTS

1

INTRODUCTION TO ACTINIDE
DIOXIDE MELTING

In science if you know what you are doing you should not be doing it.
In engineering if you do not know what you are doing you should not be doing it.
Of course, you seldom, if ever, see either pure state.

Richard Wesley Hamming [1]

Scientifically speaking, phase transitions such as melting are complex processes and universal models describing the solid, the melt and the melting process are lacking. From an engineering point of view, melting is an interesting phenomena, because it is directly observable and directly measurable.

In so far as human nature is often fascinated by extremes, melting draws attention because it is one of the extreme situations for a material, which one can observe. Materials presenting very high melting points are already appealing because of the inherent challenge in finding their melting temperatures, without even considering their usefulness for all kind of applications. This challenge grows especially with materials whose melting temperatures are above usual temperature detection/heating ranges and maybe also feature other physicochemical properties, which may complicate the measurements itself.

1.1. APPLICATIONS OF ACTINIDE DIOXIDES

THE melting temperatures of the metallic actinides are not particularly exceptional, as other elements melt at much higher temperatures. But together with non metallic elements, the compounds present different properties, as in the example of the widely used ceramic actinide dioxides [1], whose melting transition temperature are among the highest values throughout all known materials. The most striking difference to more

---

[1]The Art of Doing Science and Engineering: Learning to Learn (1997)

common materials is surely the radioactive nature of the actinides. Due to the strong alpha radiation emitted by most of the actinides, handling in a secure environment (glove boxes or hot cells) is absolutely necessary for any material testing. The constraints have restricted investigations to only a few laboratories in the world, and limited also the amount of data on many actinide compounds.

The most important application of actinide compounds is the generation of energy in nuclear power plants. Although being now in use for decades, changing conditions and demands in the world have required a constant research and development on the concepts of each component. Such new concepts were defined and summarised for the Generation IV reactor types. Several countries united and agreed on a common nuclear energy development and formed the Generation IV International Forum [2]. New reactor concepts try to exclude disadvantages of former reactor types while bringing advances in terms of safety and economics. Such improvements include: (i) sustainability of resources, (ii) economics, (iii) safety and reliability, and (iv) proliferation resistance. These points are achieved by making the nuclear fuel cycle more efficient, minimising the amount of waste generated, and improving reactor concepts and fuel materials.

The choice of nuclear fuel cycle has a large impact on the long-term sustainability of the nuclear energy option. Limited resources and the continuous research for long term waste storage require more knowledge on (potential) fuel materials. In this context reprocessing and closed fuel cycles can include also concepts as partitioning and transmutation and are discussed together with reactor concepts.

Actinide oxide fuels have remained the preferred option in new designs and have therefore stayed in the focus of nuclear research. Moreover, oxide fuels are used in reactors all over the world, most commonly as uranium dioxides (UO_2) or as a mixed uranium - plutonium dioxide (Pu-MOX). Other actinide dioxides form in the fuel as minor constituents during the fission process. However, these minor actinides (Np, Am, Cm) contribute to the long term radiotoxicity of the fuel to a high extent [3]. Thorium, besides, is used in its dioxide form as an alternative to uranium based fuels. Generally, thorium resources are more abundant than uranium, but none of its isotopes are fissionable and it has to be used in conjunction with another material as a fuel. Thorium dioxide (ThO_2) is relatively inert and does not oxidise further, unlike uranium dioxide [4]. It has a higher thermal conductivity and lower thermal expansion than UO_2, as well as a much higher melting point [5]. Thorium-based reactor fuels would be a poor source for fissile material in terms of proliferation significance, but need uranium and plutonium isotopes (U-233, U-235 or Pu-239) for starting a chain reaction. Opposed to uranium based fuels, it needs to be first irradiated and reprocessed. But generally mixed oxides containing thorium are less investigated at high temperatures.

But a parameter like melting is crucial for the safe usage of such materials. The melting temperature is indeed one of the material properties which defines the safety of the nuclear fuel [6]. A high melting temperature is preferably combined with high thermal conductivity to have a safe margin to melting. In contrast to other fuel types such as nitrides, carbides, fluorides, etc., oxides fuels have the advantage of a fair chemical stability and comparatively well established preparation processes.

1.2. METHODS FOR MELTING TEMPERATURE MEASUREMENTS

MELTING experiments on actinide dioxides have two purposes: one is a general scientific interest in the materials' behaviour, also connected to the 5f electronic state in the actinides; the second is the safety of nuclear plants with these materials as fuels. Both cannot easily be investigated experimentally at the same time, as nuclear plant accidental conditions are difficult to mimic on the one hand in a laboratory environment. On the other materials are affected in multiple ways during an core accident. The aim is therefore to provide fundamental material properties. This data can be further used to derive material phase diagrams, which determine the material's performance.

The experimental techniques can be either of static or dynamic kind. While in static methods, conditions of temperature, pressure, volume are kept stable, dynamic methods detect changes with variation of these parameters. Static measurements are feasible at high temperature only in systems stable enough not to decompose, not to change stoichiometry or not to show a non-congruent state before reaching equilibrium conditions. In the case of actinide dioxides these conditions are only partly fulfilled. In dynamic measurements changes during the phase transition in properties such as electrical conductivity, thermal expansion or optical characteristics can be exploited. The most common dynamic technique for melting experiments is a thermal analysis of the heating and/or cooling process in which the rate of heating/cooling is analysed. Changes are caused during a phase transition by absorption or release of the latent heat (ΔH_{fus}). In a temperature vs. time profile, or thermogram, ΔH_{fus} will cause a change in gradient or even a complete thermal arrest.

In the traditional thermal arrest techniques applied for materials melting below approximately 2700 K, electrical furnaces are generally used as heat sources. Temperature can be measured by means of traditional thermocouples, or using optical pyrometers, if the temperatures of interest are above 2500 K. When thermocouples are employed, contamination of the specimen with foreign materials can represent a considerable problem. As for the optical pyrometer, both the holder and the specimen must be shaped in such a way that black-body conditions are achieved (optical emissivity as close as possible to unity), or alternatively, the sample's optical emissivity must be known. Containerless conditions should be ideally achieved in order to avoid possible interaction of sample with the holder which can lead to undesired changes in melting temperature. Levitation techniques are in principle methods of investigation satisfying containerless conditions, but require on the other hand an bigger experimental effort compared to the setup used in this study.

The present approach uses a remote laser heating method which allows quasi containerless conditions where interaction is minimised. The molten material only in contact with the same material in the solid state. Due to the possible high power laser heating, short duration experiments are possible, limiting possible reactions of the liquid. Pyrometry is used for detecting the phase transition temperatures. In the absence of black-body conditions, radiance spectroscopy allows an estimation of the emissivity of the samples, and therefore a calculation of the true temperature.

The accuracy with which a phase diagram is experimentally determined depends on two main issues: the accuracy of the temperature measurement, and the accuracy in characterising the sample composition at the exact moment when the phase transition

occurs. But an in-situ material characterisation is yet not feasible at the melting temperatures of the actinide dioxides. Several characteristic methods were used in these studies investigating composition and stoichiometry before and after the melting experiments. The surface was investigated by Raman spectroscopy, Scanning Electron Microscopy (SEM) and Energy Dispersive X-ray spectroscopy (EDX). With X-ray Diffraction (XRD) a more general analysis of the bulk material was possible, while with X-ray Absorption Near Edge Structure (XANES) spectroscopy was obtained information on the charge/valence state of the materials under investigation.

1.3. MELTING TEMPERATURES OF REFRACTORY OXIDES

R EFRACTORY oxides show a high thermal stability, but the chemical stability of these materials at high temperature is sometimes doubtful and therefore melting points, as for example, for calcium oxide (CaO) or magnesium oxide (MgO), can be controversial [7]. The chemical stability around the melting point depends strongly on the reaction between the sample and its environment, enhanced by exchange of oxygen. This problem appears also in the case of actinide oxides which can raise, in conjunction with traditional heating techniques, the suspicion that available results may be affected by such interactions.

Several actinide oxides and mixed systems were investigated to different extents in the past. The industrial interest in uranium has driven extensive studies of the phase diagram. The recent application of the quasi containerless laser heating method to UO_{2+x} [8] has shown disagreement with earlier studies using more traditional methods. In the case of PuO_2 this melting technique has also revealed a temperature hundreds of Kelvin higher than evaluated before [9]. ThO_2 on the other hand has already been investigated with a laser heating approach [10], showing and confirming the highest melting temperature among the actinide dioxides. The deviations are mostly assigned to the reactivity of the materials with their environment. These interactions can be linked to the different oxygen potentials of the actinide dioxides, increasing from ThO_2 (most stable) with the atomic number of the actinide. NpO_2 has not been investigated with such a fast quasi containerless melting technique before. However, other actinide dioxides (as e.g.: PaO_2, AmO_2) are very unstable and decompose before even reaching high temperatures, so that characterisation of pure materials could only be possible with further developments of the experimental techniques.

Mixed actinide systems form a solid solution throughout the whole composition range and within all phases. The melting and solidification transition is expected to behave as an ideal pseudo-binary mixture. Surprisingly, the mixed uranium-plutonium dioxide (($U, Pu)O_2$) does not seem to follow such ideal behaviour in a first laser melting study [11]. Thermodynamic modelling of the phase diagram [12] has explained this effect in terms of a non-congruent and non-stoichiometric melting phase transition for pure dioxides and ($U, Pu)O_2$. To date, only compositions with high plutonium content were investigated with a laser heating method.

The mixture ($U, Th)O_2$ has the advantage of not being very radioactive. Therefore this system was already the topic of several studies with first evidence of a minimum in the melting transition close to pure UO_2 [13]. ($Pu, Th)O_2$ has only recently become interesting industrially, and its high temperature behaviour has seen little investigation.

Only two thermodynamic assessments have existed so far, using a melting temperature for PuO_2 much below the temperature measured with the current technique.

These three mixed actinide systems present a complete picture in terms of diversity of material properties among the actinides. They combine the largest difference in melting transition of the end-members, together with different possible oxidation states of the metals, as well as, the largest difference in the ionic radii of the metals. These differences may explain next to the different oxygen potentials of the end-members the unexpected minimum found in these pseudo binary solid solutions.

1.4. ENHANCING ACTINIDE DIOXIDE MELTING POINT DATA

THE research described in this thesis addresses the melting point determination and the inherent difficulties for refractory materials, with special focus on the actinide dioxides and some of their solid solution systems. The chosen investigation method - a laser melting approach with a thermal arrest method and optical temperature measurement - has proven itself in the past with similar tests on other refractory materials [8, 11, 14, 15]. To ensure material characterisation including composition and stoichiometry, different material analysis methods were applied on fresh, heated but not melted, and re-solidified material.

High temperature phase change determinations are subject to possible large uncertainties. Chapter 2 presents calcium monoxide (CaO) as an example of a disputed melting transition temperature for a refractory material. In addition, the determination of the emissivity with this experimental setup and the refinement of the laser melting technique in terms of the efficiency of the heating cycles are also described.

Chapter 3 fills the gap in knowledge for the determination of the melting temperature of stable actinide dioxides with a laser heating approach. NpO_2 has been measured with a higher melting temperature than the earlier published values. A review of the updated actinide dioxide melting temperatures is presented in chapter 4. The melting temperatures are compared with other material properties for possible similarities and correlations. The Lindemann melting criterion is in particular used to interpolate between known values and extrapolate to the theoretical melting points of PaO_2, CmO_2 and AmO_2.

The chapters 5 to 7 describe the melting and solidification behaviour of three mixed actinide oxide systems. These materials allow a parameter study with different properties of the end-members (ionic radii, melting temperature, stability/oxygen potential) for a better understanding of such actinide mixed systems. First, the $(U, Pu)O_2$ system is presented throughout all compositions, allowing a more complete picture for this material. Within the $(U, Th)O_2$ investigation, the melting point of ThO_2 was confirmed, as well as, the already presented minimum in the solidification temperature. In the study of $(Pu, Th)O_2$, a minimum temperature was also found, as for the other two mixed systems. Due to the large differences in the end-members, segregation effects were also identified in the re-solidified material. With the assistance of thermodynamic optimisation of phase diagrams, the minimum temperature was interpreted by changing the perspective from a pseudo binary system to a ternary (metal-metal-oxygen) system.

Finally, the most important findings, improvements, and a short outlook are presented in a summary & conclusion.

1

REFERENCES

[1] W. E. Lee, M. Gilbert, S. T. Murphy, and R. W. Grimes, *Opportunities for Advanced Ceramics and Composites in the Nuclear Sector,* J. Am. Ceram. Soc. **96**, 2005 (2013).

[2] Generation IV International Forum, *A Technology Roadmap for Generation IV Nuclear Energy Systems*, Tech. Rep. (USDOE Office of Nuclear Energy, 2002).

[3] P. Carbol, D. Wegen, and T. Wiss, *5.16 - Spent Fuel as Waste Material,* in *Compr. Nucl. Mater.*, edited by R. J. Konings (Elsevier, Oxford, 2012) pp. 389–421.

[4] M. S. Wickleder, B. Fourest, and P. K. Dorhout, *Thorium,* in *Chem. Actin. Trans. Elem.*, edited by L. R. Morss, N. M. Edelstein, and J. Fuger (Springer Netherlands, 2011) pp. 52–160.

[5] C. Guéneau, A. Chartier, and L. V. Brutzel, *2.02 - Thermodynamic and Thermophysical Properties of the Actinide Oxides,* in *Compr. Nucl. Mater.*, edited by R. J. Konings (Elsevier, Oxford, 2012) pp. 21–59.

[6] D. Olander, *Nuclear fuels - Present and future,* J. Nucl. Mater. **389**, 1 (2009).

[7] C. Ronchi and M. Sheindlin, *Melting point of MgO,* J. Appl. Phys. **90**, 3325 (2001).

[8] D. Manara, C. Ronchi, M. Sheindlin, M. Lewis, and M. Brykin, *Melting of stoichiometric and hyperstoichiometric uranium dioxide,* J. Nucl. Mater. **342**, 148 (2005).

[9] F. De Bruycker, K. Boboridis, P. Pöml, R. Eloirdi, R. Konings, and D. Manara, *The melting behaviour of plutonium dioxide: A laser-heating study,* J. Nucl. Mater. **416**, 166 (2011).

[10] C. Ronchi and J.-P. Hiernaut, *Experimental measurement of pre-melting and melting of thorium dioxide,* J. Alloys Compd. **240**, 179 (1996).

[11] F. De Bruycker, K. Boboridis, R. Konings, M. Rini, R. Eloirdi, C. Guéneau, N. Dupin, and D. Manara, *On the melting behaviour of uranium/plutonium mixed dioxides with high-Pu content: A laser heating study,* J. Nucl. Mater. **419**, 186 (2011).

[12] C. Guéneau, N. Dupin, B. Sundman, C. Martial, J.-C. Dumas, S. Gossé, S. Chatain, F. D. Bruycker, D. Manara, and R. J. Konings, *Thermodynamic modelling of advanced oxide and carbide nuclear fuels: Description of the U-Pu-O-C systems,* J. Nucl. Mater. **419**, 145 (2011).

[13] R. Latta, E. Duderstadt, and R. Fryxell, *Solidus and liquidus temperatures in the UO_2-ThO_2 system,* J. Nucl. Mater. **35**, 347 (1970).

[14] C. Utton, F. De Bruycker, K. Boboridis, R. Jardin, H. Noel, C. Guéneau, and D. Manara, *Laser melting of uranium carbides,* J. Nucl. Mater. **385**, 443 (2009).

[15] H. F. Jackson, D. D. Jayaseelan, D. Manara, C. P. Casoni, and W. E. Lee, *Laser Melting of Zirconium Carbide: Determination of Phase Transitions in Refractory Ceramic Systems,* J. Am. Ceram. Soc. **94**, 3561 (2011).

2

ON THE MELTING BEHAVIOUR OF CALCIUM MONOXIDE UNDER DIFFERENT ATMOSPHERES

Dario MANARA, Robert BÖHLER, Luca CAPRIOTTI, Andrea QUAINI, Zhaohui BAO, Konstantinos BOBORIDIS, Lelio LUZZI, Arne JANSSEN, Philipp PÖML, Rachel ELOIRDI, Rudy J.M. KONINGS

The melting behaviour of calcium monoxide has been revisited by quasi-containerless laser heating under controlled atmosphere. The current results suggest that the large discrepancy in the literature data for the melting temperature of CaO is probably linked to the influence of the environmental oxidising/reducing conditions. The CaO solidification point measured in this work is (3222 ± 25) K in an oxidising environment, in agreement with previous research performed under similar conditions. In a reducing atmosphere, the liquid/solid transition occurs at a slightly, but systematically lower, less accurately reproducible temperature, (3192 ± 40) K. These phase transition temperatures are not depending on the external pressure, up to 0.3 MPa. In the latter case, radiance and optical spectroscopy measurements revealed a more abundant formation of colour centres, i.e. a higher concentration of oxygen defects in the material, which can affect the thermodynamic stability of the solid at very high temperatures. A similar behaviour may be expected to occur in multi-component material systems including CaO.

2.1. Introduction

$\mathbf{T}$HE main goal of the present work is the reassessment of the melting point of CaO and its dependence on the environmental conditions. Known for centuries as a geological material and a disinfectant, CaO (also called calcia or burnt-lime) is a common alkaline-earth oxide with fcc NaCl crystal structure [2]. CaO is produced by dissociation of $CaCO_3$ upon heating, according to the well known equilibrium [2]:

$$CaCO_3 \rightarrow CaO + CO_2 \tag{2.1}$$

Equilibrium 2.1 is easily reversible at room temperature, which makes CaO relatively unstable in contact with the CO_2 of the air. Reaction 2.1 occurs whenever lime-based minerals are brought to high temperature. Knowledge about the high-temperature behaviour of calcia is therefore paramount for the study of number of these minerals under extreme conditions, especially in relation to their mechanical stability, optical properties and equation of state [3, 4].

On the other hand, very numerous applications justify the great technological interest of CaO, that make its chemical industry production second only to that of H_2SO_4 [2]. Broadly employed in the chemical and construction industries, it can also be used as a source of heat when put in contact with water: an exothermal reaction occurs with a production of calcium hydroxide. Furthermore, recent studies on Inert Matrix Nuclear Fuel (IMF) [5, 6] suggest calcia also as a stabilising element for this innovative anti-proliferation nuclear fuel.

An especially interesting property is that it can withstand temperatures above 1800 K without dissociating or melting that is, it can be considered as a refractory material.

2.1.1. The controversial melting point of CaO

The melting/freezing point of CaO is certainly higher than all the International Temperature Scale 1990 (ITS90) established references [7]. It had even been studied as a new higher temperature standard reference [8], save for the obvious large discrepancy in the available experimental data. The existing values for the melting temperature of CaO vary between 2833 K and 3223 K [8–13] (Table 2.1). Lower melting temperatures were generally obtained with traditional crucible heating techniques. With the sole exception of the solar furnace heating experiments performed by Noguchi et al. [9], where the clear

T_m (K)	Reference	Experimental approach
2863	Noguchi et al. (1966)	Solar furnace (uncertain)
2890	Panek (1979)	Electrical furnace
2833	Shevchenko (1979)	Electrical furnace
3223	Foex (1966)	Solar furnace
2886	Hlaváč (1982)	Electrical furnace
3178	Yamada (1985)	Solar furnace
3200	NIST JANAF	Review
3222	This work	Laser heating

Table 2.1: CaO melting temperatures reported in the literature.

thermal arrest observed above 3100 K was arbitrarily attributed to a liquid/gas transition rather than a solid/liquid one, experimental methods in which the contact between burnt lime samples and their containment was limited systematically yielded higher values. This observation led Foex [12] and Yamada et al. [8] to the conclusion that the reported lower melting/solidification temperatures did not correspond to pure CaO, but rather to compositions that largely reacted with their containment. Consequently, the high melting/freezing point measured by these latter Authors has been retained in the JANAF Tables [14], which report for CaO (3200 ± 50) K.

If the 1986 study by Yamada et al. [8] is the latest experimental work available, further discussion on the calcia melting behaviour can be found in more recent literature about phase diagram studies of the CaO system [15] or thermodynamic optimisation (CALPHAD) of systems including CaO as an end member [16–25]. In particular, Pelton et al. [16, 17] criticised the high melting point of burnt lime reported in the JANAF tables, noticing the good agreement between data reported at lower temperature, and the fact that a lower melting point would be thermodynamically more consistent with phase equilibria assessed for multi-component systems including CaO. In this interpretation, the higher-temperature phase transition reported by Foex [12] and Yamada et al. [8] was attributed to CaO boiling rather than melting. More authors [16, 18–20] recently accepted the viewpoint of Pelton et al., whereas others [21–25] used in their phase diagram assessment the JANAF data. The reasons of the existing discrepancies and controversy can be understood in the light of the complex high temperature behaviour of calcia, from both an optical and chemical viewpoints.

2.1.2. OPTICAL PROPERTIES CaO

CaO exhibits a particular optical behaviour when it is heated beyond a temperature ranging between 2000 K and 2200 K. It then emits a dazzling bright white light called limelight or Drummond light, known since the beginning of the 19th Century [26, 27], and already largely used in high-power light sources, film projection and illuminating devices without any physical explanation of of the involved phenomena. The most recent assessment of this subject is due to Kubarev [27], who experimentally observed a rather abrupt evolution of calcium oxide from an optically hardly absorbing body to an almost ideal black body in a temperature range from 2000 K to 2300 K (see Appendix I). Materials with this behaviour can be called semitransparent, although the term is probably somewhat misleading. The optical phenomenon is in fact more precisely related to a low-absorptivityhigh absorptivity transition. The material can be either highly transparent or highly reflective, depending of the photon energy, in its low absorptivity state. When the critical temperature identified by Kubarev [27] was reached, the emissivity ϵ_λ (equal to the absorptivity within the validity of Kirchhofs law) [28] of calcium oxide increased by a factor of about ten, which implied a complete change of the whole optical behaviour of this material. Considering $\epsilon_\lambda \approx 1$ at high temperature, Kubarev obtained a reasonable value of 0.1 at low temperature, which was in agreement with emissivity values found for other white oxides.

The only possible technique to measure phase transitions at T > 2500 K is optical pyrometry, based on the detection of the sample thermal radiance. Optical pyrometers measure the radiance temperature T_λ, which can only be converted into real tempera-

ture T if the samples emissivity ϵ_λ is known, as indicated by Eq. 2.2 [28]:

$$\frac{1}{T} = \frac{1}{T_\lambda} + \frac{\lambda}{c_2} \cdot \ln \epsilon_\lambda \qquad (2.2)$$

where a value of 14,388 μmK is used [28] for the fundamental constant c_2 (cf. Appendix I). It can therefore be understood how a sudden change in emissivity makes it particularly difficult to measure stable thermograms on a calcia specimen heated beyond the melting point, unless the sample itself is either contained in another black-body shaped material (with, however, a high contamination risk), or shaped itself as a black body cavity (which however induces a large uncertainty due shape loss upon melting). The first approach was adopted in research based on crucible furnace heating [10, 11], the latter by Yamada et al. [8], Noguchi et al. [9] and Foex [12] who employed a solar furnace heating technique. In the current work, the sample surface is directly measured in parallel to the sample emissivity, which allows an in situ determination of the sample real temperature.

Further details about radiance emission of a hot sample are given in Appendix I.

2.1.3. CHEMICAL PROPERTIES

The most fundamental high-temperature chemical property of calcia for the present study is the solubility of oxygen in liquid Ca. Calcium is well known to exist only as a pure metal or a divalent cation. Nonetheless, Bevan and Richardson [29] estimated that above the Ca + CaO eutectic temperature (1107 K ± 1.5 K), liquid calcium can dissolve oxygen up to an oxygen atomic fraction x(O) = 0.130.15 at 1523 K, whereas the solubility experimentally observed by Zaitsev and Mogutnov [19] at temperatures closer to Ca boiling (approximately 1800 K) are of the order of x(O) = 0.10. No experimental information is available beyond such temperature range up to the melting point of CaO.

Recently, the thermodynamic calculations of Lindberg and Chartrand [20] showed that the mentioned liquidus line, representing the solubility of oxygen in liquid calcium at equilibrium with CaO, can be prolonged at temperatures higher than the boiling point of Ca, in the hypothesis that the formation of gas is suppressed. This metastable liquidus, which can be observed, for example, by suitably increasing the ambient pressure and/or by performing very fast heating/quenching cycles, extends until the CaO melting point. On the other hand, it is commonly accepted [20] that even in equilibrium with atmospheric pressure liquid CaO dissolves more excess calcium than excess oxygen, i.e. it exists on a narrow composition range extending from approximately x(O) = 0.48 to x(O) = 0.5 (Fig. 2.1). The corresponding phase boundaries are therefore consistent with the existence of slightly hypostoichiometric liquid, freezing at the invariant temperature where solid and liquid CaO are in equilibrium with gaseous Ca (S + L + G line in the inset). This invariant temperature is slightly lower than the congruent CaO melting point.

The chemical behaviour of calcium oxide in the proximity of the congruent melting point becomes, under such conditions, less simple than one would expect for a line compound. For example, the existence of hypostoichiometric liquid CaO can open new questions: the effective congruent melting and freezing composition of this compound, the possibility to quench to lower temperature a defective solid starting from the melt, the behaviour of CaO in mixed systems with other oxides, metals or more general com-
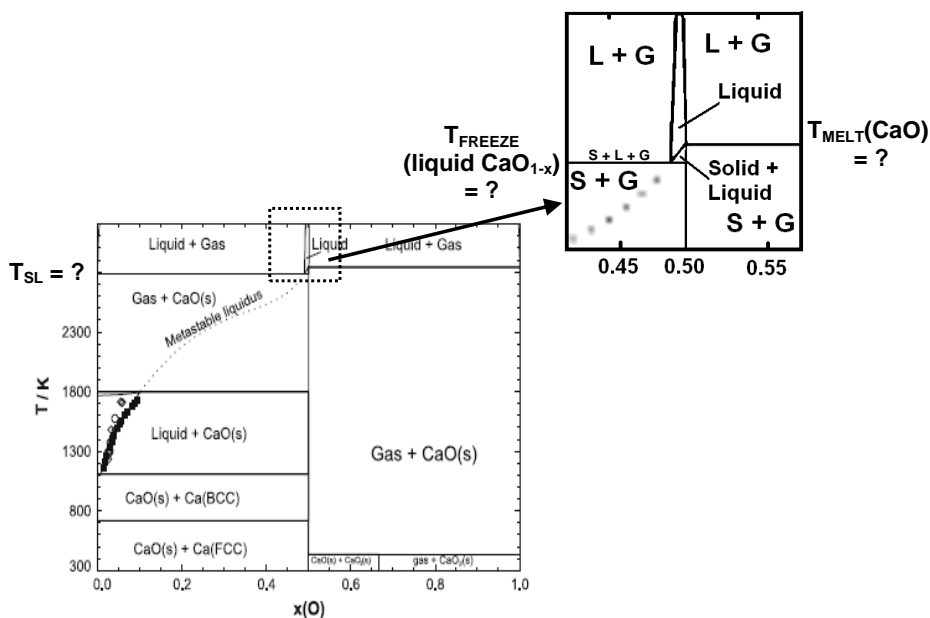
Figure 2.1: The CaO binary phase diagram at 1 atmosphere (after the thermodynamic optimisation by Lindberg and Chartrand) [20]. The solid/liquid transition temperature (TSL) is still controversial. To be noted, in the inset, that the extrapolated phase boundaries are consistent with the existence of a slightly hypostoichiometric liquid, freezing at the invariant temperature where solid and liquid CaO are in equilibrium with gaseous Ca (S + L + G line in the inset graph). This invariant temperature is slightly lower than the congruent CaO melting point.

pounds, the vapour equilibria under different atmospheres etc.

In the present research, the melting behaviour of calcia is studied under different atmospheres. It is experimentally demonstrated that only under highly oxidising conditions (oxygen, air, compressed air) is the melting/solidification point of this compound reproducible with an acceptable accuracy. Under other atmospheres (inert, vacuum, highly reducing), the observed melting point decreases by an often irregular extent.

2.2. MATERIALS AND METHODS

2.2.1. SAMPLE PREPARATION

Starting material for the current analysis was commercial Alfa Aesar 99.998% CaO powder. The impurity level was therefore considered to have a negligible effect on the melting behaviour studied in this work, at least within the uncertainty limits of the current approach.

In order to remove $CaCO_3$ possibly formed in contact with atmospheric CO_2, the powder was heat treated at 1800 K in an Ar flux. Successively, it was cold-pressed into cylindrical pellets of 8 mm in diameter and 24 mm thick. The resulting pellets were sintered at 1800 K in an argon flux for 8 h. Samples were then stored under inert atmosphere (dry argon or primary vacuum) until their melting/freezing point measurements.
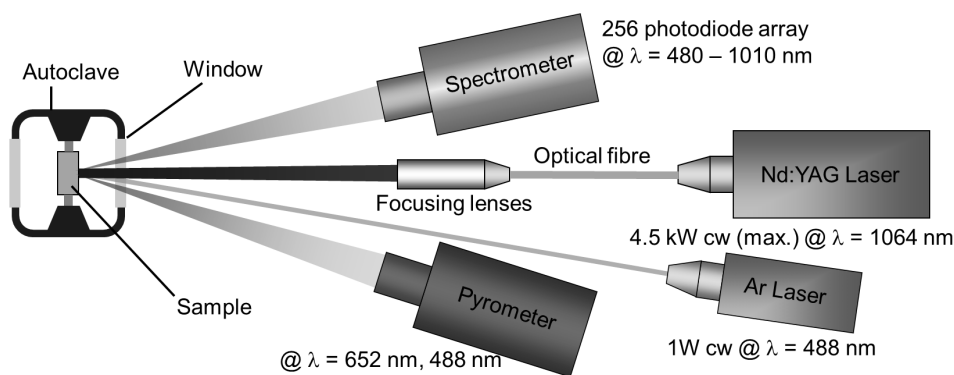
Figure 2.2: The experimental set-up used in the current research for laser heating CaO under controlled atmosphere.

2.2.2. VERY HIGH TEMPERATURE HEATING CYCLES CaO

CaO samples were mounted in a controlled-atmosphere cell closed by a gasproof quartz window 10 mm thick. Physical contact to their mount was limited by using three or four radially arranged graphite screws to hold them in place. Problems such as vast sample vaporisation and interaction with its containment, typically encountered at high temperatures, were greatly reduced or completely ruled out thanks to the high measurement speed and its containerless character. It was moreover possible to study the effect, on the observed phase transitions, of the gas nature and pressure (up to 0.3 MPa) inside the experimental cell.

The specimens were studied at very high temperature by laser heating combined with fast pyrometry (Fig. 2.2) [30] . The heating agent was a Nd:YAG 4.5 kW cw laser radiating at 1064.5 nm, programmable with a complex power/time profile. The laser beam, conveyed by fibre optics, impinged on an approximately circular area of 8 mm in diameter on the vertical sample surface. Such geometry was chosen in order to minimise interference between the possible formation of a vapour plume from the hot surface and the optical measurement of temperature. The sample surface was heated beyond melting for variable time durations (from a few tens ms to a few seconds). This time scale was short enough for the liquid mass to be held in place by the surface tension. The corresponding depth of the molten pool varied from a few μm to about 100 μm.

The invariance of the recorded phase transition temperatures with the dwelling time in the liquid state could thus be checked, to study possible segregation or non-congruent vaporisation phenomena. The sample was let cool naturally at the end of the high power laser pulse. Cycles of three successive heating pulses beyond melting were performed in each experiment. In between them, the sample could be alternatively cooled to room temperature, or kept at an intermediate temperature, higher than the semitransparent transition temperature assumed to be approximately 2150 K, by irradiating it with the same laser but at a lower power. The second situation was preferred because it allowed a better mechanical stability of the sample throughout repeated shots, and therefore to an improved result reproducibility over successive shots.

In fact, the material absorptivity sudden increase easily causes an uncontrollable temperature excursion more than a thousand K above the melting point (see Fig. 2.4), accompanied by massive vaporisation and cracking of the sample. Preheating the sample at a temperature around the semitransparent transition allowed a better control of the material behaviour throughout the heating cycles. This could be obtained by irradiating the specimen with a constant laser beam power of 100 W, delivering a surface power density of approximately 200 W cm^2. Higher power pulses, reaching up to 1000 W cm^2 (depending on the pulse duration) were then sent to the specimen in order to heat it beyond melting.

Finite element simulations of the heating cycles [31], supported by micro-imaging of the quenched samples, ensured that at the beginning of the cooling process homogeneous temperature was produced in the laser irradiated area for a depth of a few tens μm. Thermal analysis was then performed on the natural cooling stage of the cycle.

The sample temperature was measured on a spot of 0.5 mm in diameter at the centre of the laser-heated area by means of a pyrometer equipped with a fast logarithmic amplifier (settling time of about 10 μs to 1% of log output) and operating at 655 nm [30]. It was calibrated against a standard tungsten-ribbon lamp in the range of 18002500 K, ensuring traceability to the International Temperature Scale of 1990 [32, 33]. The calibration was linearly extrapolated beyond this temperature, and its validity, as well as the quality of the optical windows and the alignment, were tested by measuring in situ the melting radiance temperatures of molybdenum and tungsten (2530 K and 3207 K, respectively, at 653 nm) [7].

For the measurement of the normal spectral emissivity NSE (ϵ_λ in Eq. 2.2), a further spectro-pyrometer, based on a linear array of 256 Si photodiodes, was used to record the sample thermal radiance in the range of 4881011 nm. This instrument allows a more complete spectral analysis, whereby its main disadvantage is in the poorer time resolution (one spectrum per millisecond at best) [30]. Due to low signal-to-noise ratio, moreover, only the range 550 - 920 nm was useful for the current measurements.

A photodiode operating at 649 nm was calibrated up to 2500 K using the tungsten–ribbon lamp and this calibration was transferred to a "tubular cavity variable temperature graphite blackbody furnace" up to 3300 K. The remaining photodiodes were then calibrated with this blackbody, allowing a conversion of output signal to spectral radiance over the entire useful wavelength range.

The measured radiance spectra recorded on calcia in the vicinity of the melting / solidification point were fitted by least-squares regression to Plancks distribution law for blackbody radiance, modified by a wavelength- and temperature-dependent function assumed to represent the normal spectral emissivity. Although such an approach is known to be affected by low numerical accuracy [34], compared to other techniques, it can be considered as acceptable for high emissivity materials, like calcia at high temperature, which are known to follow a grey body (GB) behaviour (NSE quasi-independent of λ). Such a behaviour has been confirmed with the present measurements, yielding for freezing CaO in air $\epsilon_{BG} = 0.92 \pm 0.05$ for 0.655 μm $\lambda \leq 0.92$ μm, in agreement with previous data [27] and recent ab-initio calculations of CaO optical properties [35].

Fig. 2.3 shows an example application of this procedure to a thermogram recorded during a laser heating pulse on a CaO sample under argon. Each full circle of the re-

2
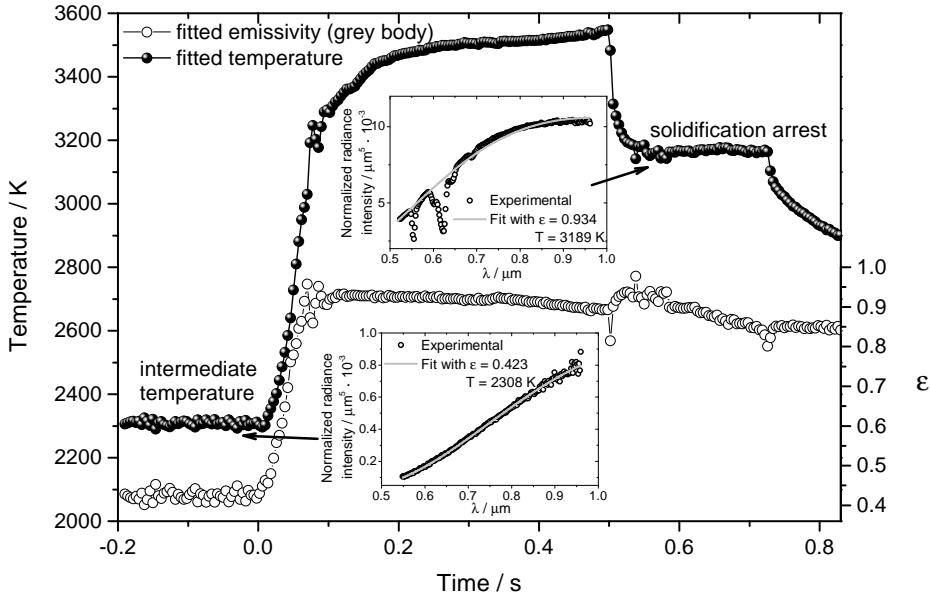
Figure 2.3: Application of the current radiance spectral analysis procedure to a thermogram recorded during a laser heating pulse on a CaO sample under argon. Each full circle of the reported thermogram (temperature-vs.-time curve) represents the temperature giving, together with the corresponding emissivity value (open circle in the emissivity-vs.-time curve), the best fit for the radiance spectrum recorded at a given time, with an accumulation time of 4 milliseconds per spectrum. The two insets show examples of radiance spectra recorded one at an intermediate temperature of approximately 2300 K (slightly above the low-absorptivityhigh absorptivity transition) and one at the beginning of the solidification thermal arrest. Analytical curves fitting the experimental spectra are shown, too. One such spectrum was recorded and fitted per each experimental point (circle) displayed

ported thermogram (temperature vs. time curve) represents the temperature giving, together with the corresponding emissivity value (open circle in the emissivity vs. time curve), the best fit for the radiance spectrum recorded at a given time. An accumulation time of 4 milliseconds per spectrum was set in this particular example. The two insets show examples of radiance spectra recorded one at an intermediate temperature of approximately 2300 K (slightly above the low-absorptivityhigh absorptivity transition) and one at the beginning of the solidification thermal arrest. Analytical curves fitting the experimental spectra are shown, too.

The broad absorption bands observed in the high temperature radiance spectra were not considered in the fitting procedure, and are extensively discussed further in this paper. A clear transition in the emissivity is observed, in fair agreement with the data reported by Kubarev [27]. However, it should be noted that the lower emissivity values are possibly affected by unquantifiable uncertainty due to parasite laser radiation reflected into the spectro-pyrometer (see further Section 2.3.1). Most important for the current study was the high-emissivity value (0.92 ± 0.05), characteristic of CaO at temperatures close to melting and beyond. This emissivity value has been used to transform radiance into real temperature through Eq. 2.1 in pyrometer–recorded thermograms around the

melting transition. More mathematical details about emissivity analysis are given in Appendix I.

2.2.3. POST-MELTING SAMPLE CHARACTERISATION

Number of experimental methods was used to characterise calcia samples after the laser heating/melting/freezing cycles. Melted specimens were recovered for post - melting analysis by scanning electron microscopy (SEM, JSM-5610, JEOL®, Tokyo, Japan) and energy-dispersive X-ray spectroscopy (EDX). Cross - sections through melted surfaces were prepared for microstructural analysis and imaged unetched. Higher - magnification transmission electron microscopy (TEM) images of the melted/refrozen material were also taken thanks to a TECNAI® microscope.

Raman spectra were recorded by means of a Jobin-Yvon® T64000 confocal spectrometer with notch filters and single grating (mono configuration). This system is equipped with a microscope for confocal micro-Raman measurements. Spectra were acquired with a Peltier cooled CCD matrix, with a resolution of 1 cm^{-1}. A 488 nm Ar+ laser was used as impinging light source, with a power, on the sample surface, variable between 0.1 mW and 10 mW. Spectra were recorded with a 0 geometry (on the reflected beam).

X - ray diffraction (XRD) was performed in this work using a Bruker® D8 Advance diffractometer (Cu-K$_{\alpha 1}$ radiation) with a 2Θ range of 10 - 120 ° using 0.009° steps with 2 s of count time per step at operating conditions of 40 kV - 40 mA. The XRD instrument was equipped with a Lynxeye 3° linear position sensitive detector. TOPAS 4.2 software was used for Rietveld refinement of the experimental XRD pattern.

X - ray photoelectron spectroscopy (XPS) was used to study the oxidation state of the final material, quenched from temperatures close to melting. All XPS spectra were recorded using a Mg K$_\alpha$ excitation radiation at 1253.6 eV in an UHV chamber with a background pressure of about 5 x 10^{-10} mbar. The instrument used in this case was the Omicron EA-125 hemispherical deflection analyser with a resolution of 0.5 eV. The system was calibrated using the Au-4f$_{7/2}$ of a sputter-cleaned polycrystalline AU standard set to a binding energy (BE) of 84.0 eV. The kinetic energy of photoelectrons (PE) were analysed at constant analyser energy scan mode with a pass energy of 20 eV. The detailed scans were performed at medium magnification mode with an angular acceptance of ±4°. The area analysed with this configuration is 3 mm in diameter.

2.2.4. UNCERTAINTY ANALYSIS

The most significant uncertainty sources have been combined, according to the independent error propagation law [30], to yield relative uncertainty bands corresponding to one standard deviation (1-k coverage factor). These uncertainty sources concern the current temperature scale definition δT (i.e. the uncertainty in the pyrometer calibration), the NSE assessment δT$_{\epsilon\lambda}$ and the experimental data dispersion (1σ standard deviation) on the current phase transition radiance temperature data δT$_{\epsilon m}$, this latter being the main source of uncertainty:

$$\delta T_m = \sqrt{\delta T^2 + \delta T_{\epsilon\lambda}^2 + \delta T_{\epsilon m}^2} \qquad (2.3)$$

The high relative uncertainty bands reported in the next section should not surprise when one considers the extreme conditions under which the current data have been

measured, and the factors potentially affecting the radiance measurements. In particular, one can assume that the main uncertainty causes are here the sample surface morphology, the onset of vaporisation and surface sputtering and the possible metastable supercooling of liquid below the equilibrium freezing temperature. These phenomena can be minimised by setting a suitable pressure and atmosphere in the sample-holding vessel, and by properly choosing the laser power–time profile.

2.3. RESULTS

2.3.1. HEATING-COOLING CYCLES
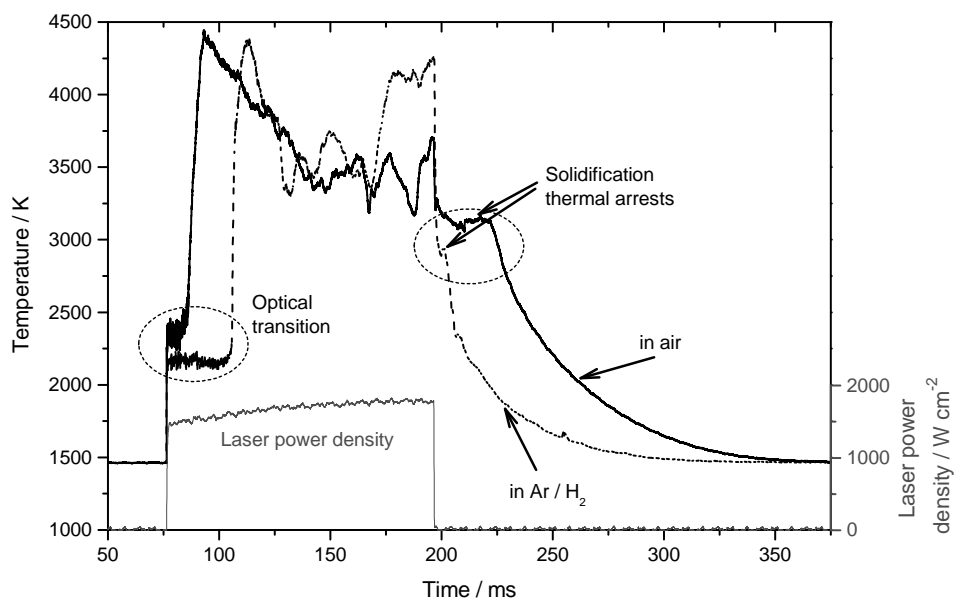
Figure 2.4: Typical thermograms recorded on CaO in air and in Ar + 6% H$_2$ at 0.655 μm. Effects of the absorption bands (see Fig. 2.6) have been taken into account by correcting the emissivity used to obtain the true temperature curves. To be noted the optical transition around 2150 K on the heating stage, where CaO transforms from mostly reflecting (low emissivity) to a highly absorbing (high emissivity), and the irregular features of the thermogram when the sample is fired to very high temperature.

Fig. 2.4 shows two thermograms measured on a CaO sample under compressed air or argon + 6% hydrogen (both at 0.3 MPa) with a single high-power (close to 1500 W cm^{-2}) heating pulse conceived to overcome the low absorptivity-high absorptivity limit for this material.

The dynamics of melting and freezing under the current conditions can be figured out by interpreting the recorded thermogram with the help of heat and mass transport simulations of the same kind of processes reported in previous publications [31, 36]. A first apparent thermal arrest can be observed on heating at a radiance temperature around 2150 K. This corresponds to the mentioned low absorptivity-high absorptivity optical transition. More precisely, the observed behaviour here seems to be consis-

tent with a high reflectivity→high absorptivity transition, at least at the near-infrared laser wavelength. It is actually obvious from the thermogram shape, that CaO mostly reflects the impinging laser radiation at temperatures lower than the optical transition point. In fact, the thermogram shape reproduces, in the first part of the experiment, the shape of the heating laser power profile. Some of the laser radiation is then certainly reflected into the pyrometer which detects it as parasite radiation, probably too intense to be properly filtered by the pyrometers optical path.

It can be seen from the thermogram, that after the sample has absorbed enough energy to overcome such optical transition, its temperature starts to increase very rapidly, reaching almost 4500 K in a few milliseconds. Because of the conditions far from the thermal equilibrium in this stage of the experiment, the possible crack formation and interaction between the laser beam fraction reflected into the pyrometer detector and the thermal radiation emitted by the sample, features on the heating flanks of the thermogram were generally ignored for the present analysis. Even a thermal arrest corresponding to melting was only very seldom observed under the current conditions. In fact, the uncontrollable formation of cracks on the surface and the massive vaporisation (the boiling point - probably corresponding to a slight inflection sometimes observed around 3450 K - was certainly overcome) were likely to play a major role in the entire heating process, and particularly on the very irregular features of the thermogram after the maximum temperature was reached. Nonetheless, the very high maximum temperature was still moderate enough for the sample to remain integral throughout the experiment. It was therefore possible to clearly identify the freezing thermal arrests on the cooling flanks of the thermogram. There, also some super-cooling can be seen. This phenomenon has to be ascribed to the high cooling rate, which hinders the crystal nucleation in liquid calcium oxide. Solidification starts at the bottom of the molten pool formed on the sample surface, where the solid interface fosters growth of solid inside the liquid cooled below the equilibrium freezing temperature. Only when the growing solid reaches the upper, free liquid surface (the one seen by the pyrometer), the recorded temperature starts to rise until the equilibrium freezing temperature is reached.

As mentioned in Section 2.2.2, an alternative approach to the melting/freezing cycles consisted in keeping the sample at an intermediate temperature, higher than the semi-transparent transition temperature, by irradiating it with a lower power of the laser beam between two high-power pulses. It was observed that such an approach gave a better stability of the sample throughout repeated shots. Fig. 2.5 reports three successive thermograms recorded under the latter conditions. Their shape is more ordinary, with neither sudden heating to extremely high temperature, nor irregular features during the sample dwelling beyond melting. Under these conditions, the melting/freezing arrests were observed at slightly higher temperature, and their repeatability was largely improved, too. It can also be noticed in Fig. 2.5 that during the high-power laser pulses the sample surface temperature tended to plateau at an almost constant value depending on the experimental conditions. Such a value was systematically different for the samples heated under air (around 3600 K) and those heated under argon-hydrogen (around 3450 K). This behaviour can probably be related to the onset of boiling in the two different experimental conditions, although such assumption should be confirmed by further research.

The set of data obtained with the second approach was obviously more suitable for

2
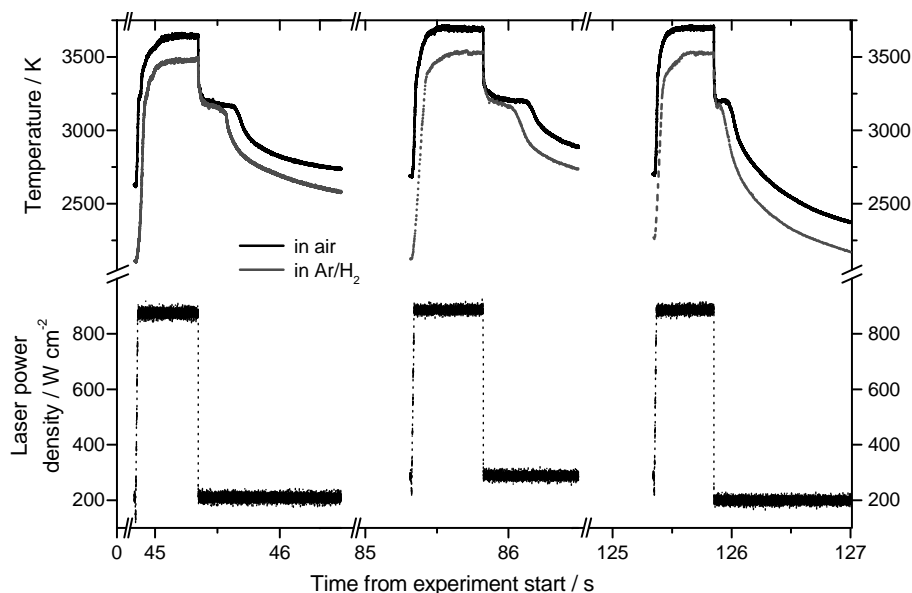
Figure 2.5: A sequence of three laser heating pulses performed on CaO in air and in Ar + 6% H₂ at 0.655 μm. Effects of the absorption bands (see Fig. 2.6) have been taken into account by correcting the emissivity used to obtain the true temperature curves. The heating laser power was maintained at 50 W cm2 in between the high-power pulses. In this way, the sample (solid or re-solidified) was not allowed to cool below the optical transition point.

any statistical analysis. However, data obtained with single laser pulses followed by natural cooling to room temperature were somewhat instructive, in that they showed that the observed solidification points were lower under those poorly-controlled conditions.

2.3.2. RADIANCE MEASUREMENTS

If very high-temperature radiance measurements are generally awkward due to the extreme conditions, in calcia the situation is even more complicated because of the well-known existence of F and F$^+$-centre luminescence [37–44].Such a phenomenon is related to the fact that photon irradiation of calcia samples excites emission and absorption bands due to photo-electronic transitions in oxygen vacancies with one (F$^+$) or two (F) free electrons, mostly detectable in the UVvis range [43]. Radiance spectra recorded on liquid and solidifying CaO under oxidising and reducing atmospheres are shown in Fig. 2.6. Because beyond the semitransparent threshold the emissivity of calcia is very close to 1 [27], these spectra are very close to Planck black-body spectra at the solid / liquid transition temperature. However, clear absorption bands can be observed in the visible range.

These bands are more numerous and intense for samples melted under a reducing atmosphere, which agrees well with the darker colour displayed by such samples after the heating cycles (see Fig. 2.6). From a pyrometric viewpoint, it would therefore be preferable to measure the radiance of calcia away from spectral windows affected by
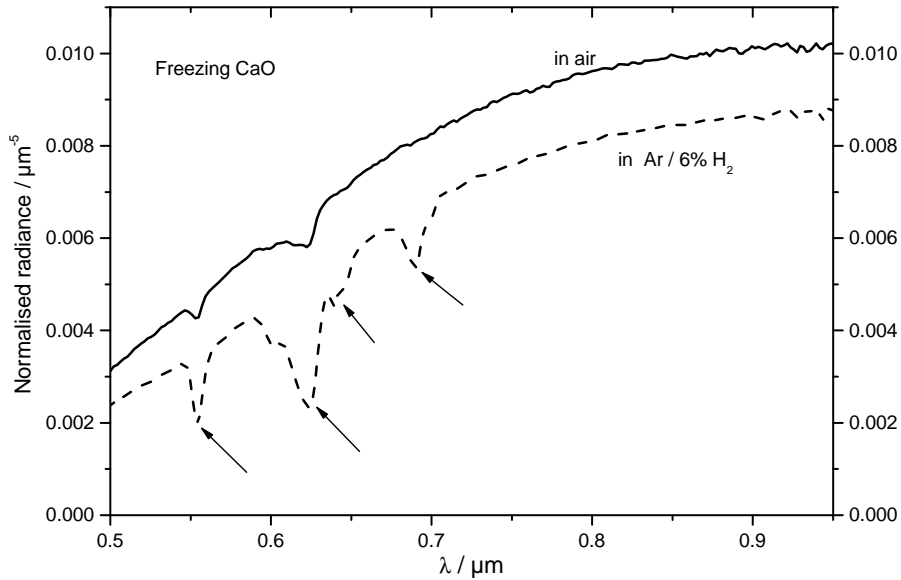
Figure 2.6: Radiance (Planck) spectra of solidifying CaO in air (solid line) and in Ar + 6% H$_2$ (dashed line). Absorption bands are clearly visible between 0.55 μm and 0.7 μm, more intense and numerous in the sample heated in Ar/H$_2$, where they correspond to the creation of oxygen defect-related colour centres and darkening of the material.

these absorption bands, in order to avoid unpredictable emissivity excursions. It is important to remark that an absorption peak is visible just around 0.65 μm, a wavelength typically used in radiance thermometry, only in samples heated under a reducing atmosphere.

2.3.3. MELTING/FREEZING BEHAVIOUR UNDER DIFFERENT ATMOSPHERES

Experiments were repeated on different CaO samples under different atmospheric conditions and with different laser pulse shapes. The vessel was filled with either compressed air or argon in order to operate under an oxidising or reducing atmosphere, respectively. In general, the observed solidification temperatures were reproducible within the reported uncertainty bands, those measured under a reducing atmosphere (3192 K ± 40 K) being slightly, but systematically lower and more uncertain than those measured under air (3222 K ± 25 K) (Fig. 2.7). For samples melted under a reducing atmosphere, thermograms measured by the spectro-pyrometer in the near-infrared range (750 nm ≤ λ ≤ 900 nm) were used in the statistics together with those recorded at 0.65 μm in order to rule out the risk of unquantifiable effects of emissivity variations due to the onset of the absorption bands displayed in Fig. 2.6. For the same reason, thermograms recorded by the fast pyrometer at 0.655 μm from CaO solidifying in Ar/H$_2$ were corrected (cf. Eq. 2.2) with ϵ_λ = 0.85 (instead of ϵ_λ = 0.95 used in the other cases).

When the sample was heated under an oxidising atmosphere, the detected melting temperatures resulted comparable with those measured by Yamada et al. [8] Since

2
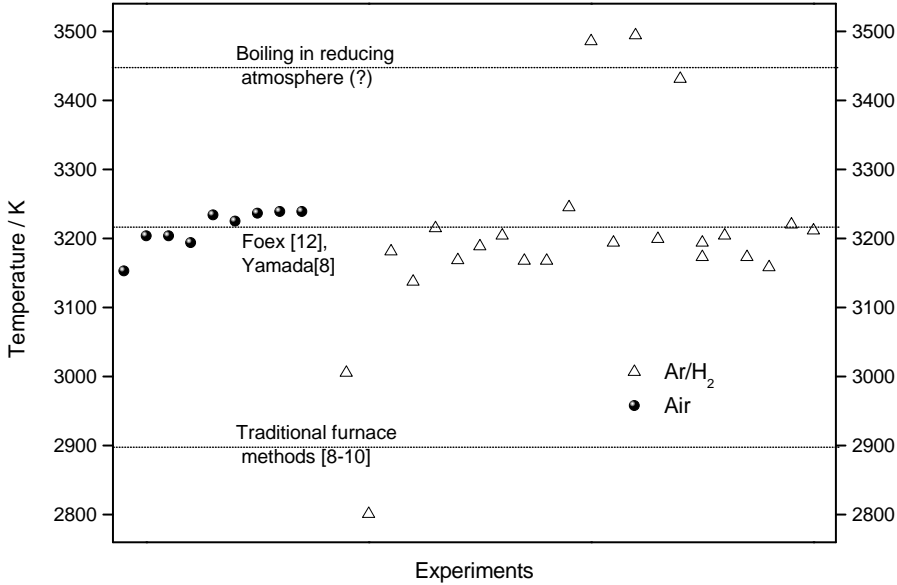
Figure 2.7: The current solidification point data of CaO compared with literature results. Further inflections occasionally observed at higher temperature and possibly attributable to boiling/condensation in reducing conditions are also reported.

also the latter authors performed their melting/freezing cycles under air (at atmospheric pressure, 0.1 MPa), it is reasonable to conclude that under these conditions, stoichiometric CaO was most probably stabilised and maintained throughout the heating cycle, and a congruent melting transition was observed. It is also worth noticing that the fair agreement between the current thermal arrests, recorded under compressed air at 0.3 MPa, and those observed by Yamada at atmospheric pressure corroborates their attribution to solidification rather than boiling. One would in fact expect a much more evident dependence of a boiling point on the external pressure, whereas the melting/solidification point variation due to a change on the external pressure of a few tenths of a MPa should be negligible [4].

A further inflection was occasionally detected at higher temperature (around 3450 K) only in thermograms recorded under a reducing atmosphere (Ar + 6% H_2 at 0.3 MPa). These inflections, reported in Fig. 2.7, have been tentatively assigned to CaO boiling / condensation under a reducing atmosphere. Such attribution would be in fair agreement with the observation, mentioned above, that in laser pulse series the temperature tended to be stabilised around 3450 K under pressurised argon + 6% hydrogen (Fig. 2.5).

The solidification arrest observed in samples melted under a reducing atmosphere was only in a couple of cases comparable with the set of lower melting/freezing data reported in the literature [9–11], these cases always corresponding to single laser pulses, and not series of shots between which the sample was kept at an intermediate temperature above 2000 K. In the vast majority of the current experiments, the solid/liquid transition was observed at a higher temperature. Under reducing atmosphere, it was slightly (a

few tens Kelvin), but systematically lower than that measured under air and affected by a considerably poorer reproducibility. It is possible, therefore, that liquid calcia samples were more sensitive, under these latter conditions, to reduction in contact with the experimental atmosphere, leading, upon solidification, to the formation of a solid richer in oxygen defects. Correspondingly, the resulting colour of such refrozen material is dark greyblack as opposed to the bright white obtained in the case of CaO melted and re-solidified under air (Fig. 2.8a and b). The kinetics and effectiveness of such a reduction would largely depend on the sample surface morphology and the experimental parameters (laser beam intensity, atmosphere, heating duration etc.), explaining the poor reproducibility.

(a)   (b)
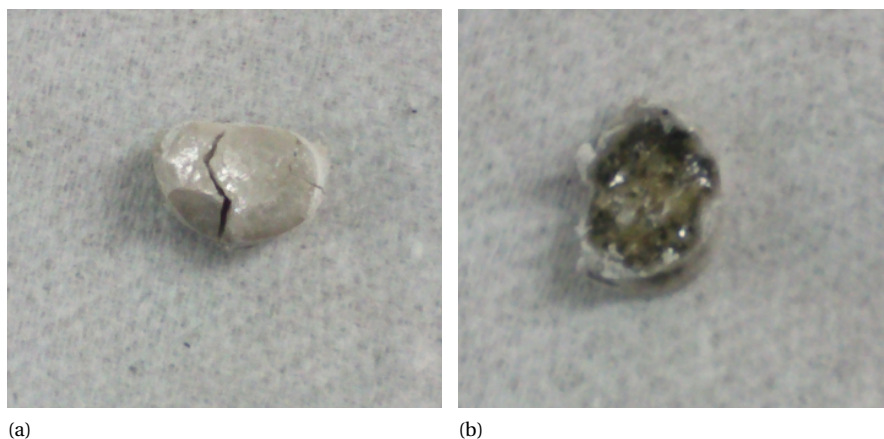
Figure 2.8: Photos of CaO samples laser melted and refrozen in air (a) and in Ar + 6% H_2 (b)

2.4. DISCUSSION

THE current experimental results show that the melting/solidification (and, probably, boiling) behaviour of calcium oxide is influenced by the atmosphere in which the solid/liquid transition occurs. The maximum transition temperature slightly higher than 3200 K can be consistently reproduced only under strongly oxidising conditions. In this case, also the original colour of calcia (bright white) is maintained throughout the heating/cooling cycle. Under reducing conditions, instead, the refrozen material results considerably darkened with respect to the fresh one (cf. Fig. 2.8). This latter phenomenon can be attributed to the formation of more colour centres (F or F^+ centres) related to oxygen defects in the re-solidified oxide. Correspondingly, although absorption bands are always observed in CaO at very high temperature, more of them, and with a higher intensity, can be seen in the material heated beyond melting under reducing conditions (cf. Fig. 2.6). The corresponding liquid solidifies at a slightly lower and less reproducible temperature. In particular, the presence of additional absorption bands in the darkened material close to 0.650 μm and 0.710 μm can be attributed to slight temperature-dependent evolutions of F^+ centre modes already reported else-

where [43, 44]. The temperature dependence of such modes has already been addressed
in earlier publications, although never at temperatures close to CaO melting [39, 41].

(a)   (b)
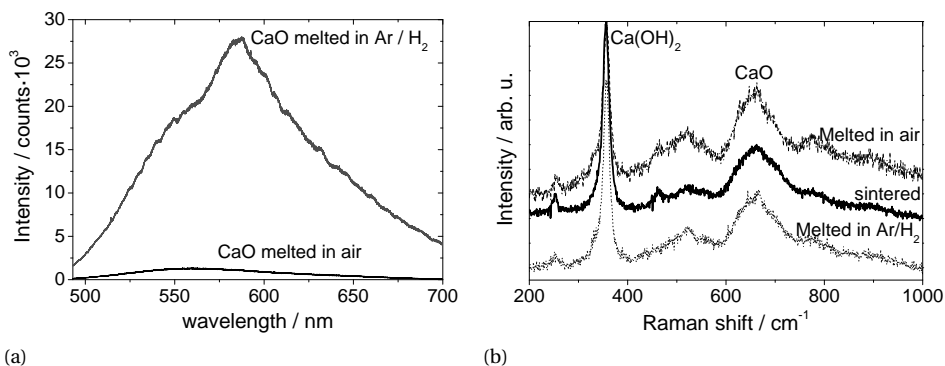
Figure 2.9: (a) Room temperature luminescence spectra recorded on the current calcia samples melted and
refrozen in air and Ar/H$_2$ by using the 0.488 μm line of an Ar$^+$ laser to excite the luminescence, and a Jobin
Yvon T64000 Raman spectrometer to detect it. (b) Raman spectra of calcia samples studied in the present
research with the same laser source.

In addition, room temperature luminescence spectra have been recorded on the cur-
rent calcia samples melted and refrozen in air and Ar/H$_2$ by using the 0.488 μm line of
an Ar$^+$ laser to excite the luminescence, and a Raman spectrometer to detect it (in a sim-
ilar way as in Ref. [40]). Such luminescence spectra showed that only the broad and
intense absorption band attributed to the 3 T$_{1u}$ $\rightarrow$ 1A$_{1g}$ transition around 0.585 μm [41–
44] was clearly visible in darkened samples melted in a reducing atmosphere, with an
evident shoulder detectable around 0.550 μm. The last feature corresponds to the only
weak and very broad band visible in the luminescence spectrum of calcia heated under
air (Fig. 2.9a). This characterisation is consistent with the formation of oxygen defects in
calcia melted and refrozen in a reducing atmosphere, similarly to other irradiation tech-
niques (laser, neutrons, electrons) employed for the creation of colour centres. Leaving
for another paper a more detailed analysis of such colour centres at high temperature,
here it is essential to remark that there seems to be a relation between their formation,
possible oxygen losses and the melting behaviour (cf. the inset in Fig. 2.1).

On the other hand, no significant differences can be appreciated in the Raman spec-
tra of the same samples (Fig. 2.9b). Characteristic bands [45] due to a Raman active com-
bination of transversal optical and acoustic phonons around 530 cm^{-1} and the transver-
sal optical phonon at 655 cm^{-1} are visible in all cases, confirming that the onset of oxy-
gen defects has no direct effect on the vibrational modes of CaO. It can also be noted that
in all samples a clear Raman peak at 363 cm^{-1} shows that the surface is contaminated
with Ca(OH)$_2$ [46] as a result of the prompt reaction with humidity at room tempera-
ture. However, calcium hydroxide decomposes [47] at around 700 K, ensuring that such
contamination had no effect on the current melting behaviour study.

The formation of colour centres is mostly related to the existence of Frenkel and
Schottky defects in the CaO crystal [44], with therefore hardly any influence on the over-

all composition of the material. Such a behaviour can be related to the phase boundaries extrapolated by Lindberg and Chartrand [20] concerning the equilibria between oxygen-defective liquid calcia, solid CaO and gaseous Ca (here reported in Fig. 2.1), where it is shown that the presence of oxygen defects thermodynamically stabilises liquid CaO at temperatures lower than that of congruent melting. The current experimental observations would be in fair qualitative agreement with those high-temperature phase boundaries but for the actual values of the invariant temperature at which CaO melts congruently (3222 K ± 25 K in the current assessment) and that of coexistence between solid CaO, liquid CaO_{1-x} and gaseous Ca (3192 K ± 40 K).
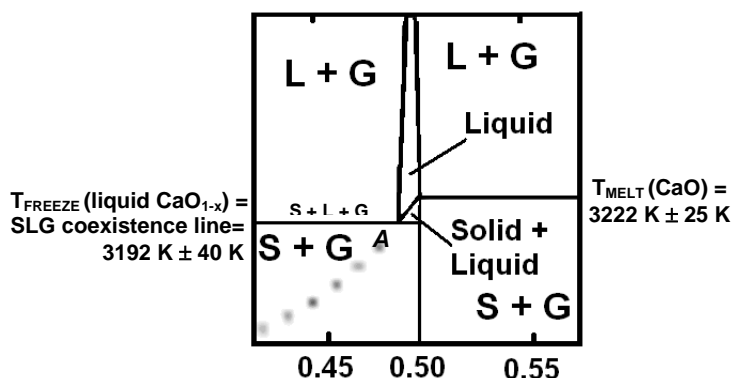
Figure 2.10: Tentative phase boundaries of the CaO system in the vicinity of the congruent CaO melting point according to the present investigation.

The inset of Fig. 2.1 is updated in Fig. 2.10 with the invariant temperatures assessed in the present research. The determination of the oxygen content x(O) corresponding to the invariant eutectic point denoted as A in Fig. 2.10 still constitutes an open challenge, which could not be resolved by the additional post-melting material characterisation performed in the present research. Calcia samples melted and refrozen both under oxidising and reducing conditions have been studied by Raman spectroscopy, XPS, XRD and transmission electron microscopy. The main results of such characterisation are compared in Figs. 2.11-2.13. XRD showed the formation of non-negligible traces of $Ca(OH)_2$ on the darkened sample surface. This observation is consistent with the fact that a more abundant oxygen defect concentration catalyses prompt reaction of CaO with even small traces of humidity. However, none of the employed techniques showed consistent differences between the two types of samples attributable to the formation of metallic calcium or to different oxygen contents.

To summarise, the current experiments seem to confirm, from a slightly different viewpoint, the conclusions already drawn by Foex [12] and Yamada [8]: stoichiometric liquid CaO freezes congruently at around 3200 K under an oxidising atmosphere and nearly container-less conditions. This also confirms the melting/freezing point reported in the JANAF Tables [14]. Moreover, the current investigation shows in a straightforward fashion that the melting behaviour of calcium oxide is not only dependent on the even-

2
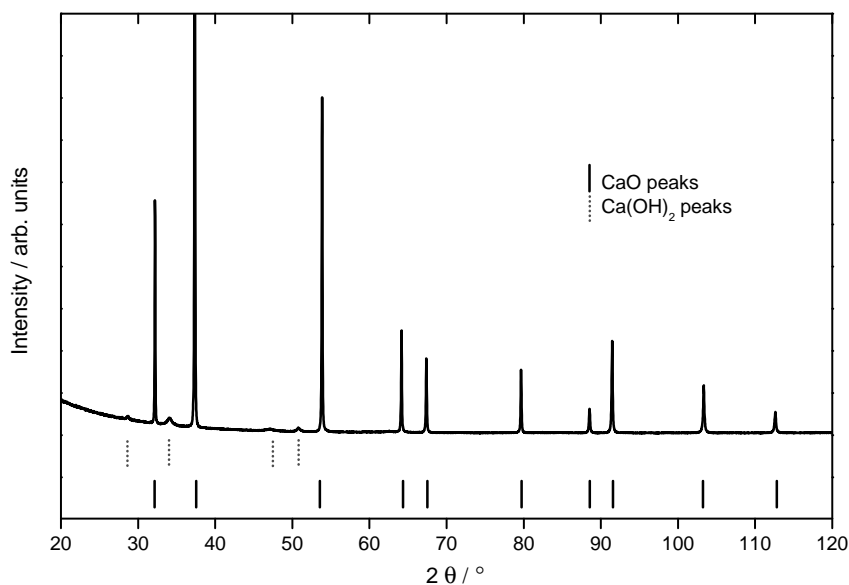
Figure 2.11: X-ray diffraction patterns of CaO samples laser melted and refrozen in Ar + 6% H_2 compared to the well known XRD peaks of burnt lime (vertical straight lines faced centred cubic, space group Fm$\bar{3}$m, a = 0.481056(2) nm). No clear differences are detectable, with the exception of broad peaks consistent with the formation of Ca(OH)$_2$ traces (estimated to a maximum of 5 wt%) on the sample surface (hexagonal, space group P$\bar{3}$m1, a = 0.35912(10) nm, c = 0.49171(2) nm).

tual interaction between sample and its containment, as it was concluded by Foex [12] and Yamada [8], but also on the atmosphere in which the heating/cooling cycles are carried out under quasi-container-less conditions. As an additional remark, this implies that the attribution of the observed thermal arrests to a liquid/vapour transition, rather than a solid/liquid one, seems unlikely, due to its negligible dependence on the external pressure.

In the light of the current results, calcium oxide displays a very high temperature behaviour somewhat similar to that of other oxides, such as MgO, CeO$_2$, UO$_2$, PuO$_2$, NpO$_2$, which have been assessed in the last decade [31, 36, 48–50].

One could imagine also for calcium oxide under very high temperature and pressure a situation similar to that reported by Ronchi et al. [51] for the equation of state of UO$_2$: the definition of a liquid/vapour equilibrium under extreme conditions is not reducible, even in a first approximation, to a single line, but rather to a closed curve with different branches corresponding to boiling and saturation conditions, limited by a critical point.

The current remarks can also have a certain impact on the assessment of pseudo-binary and multi-nary phase diagrams in which CaO constitutes one end member [16–25]. The analysis of some of these systems seems better compatible with a lower melting/freezing point of CaO [16, 17]. However, this is in obvious contradiction with the results of the present and other detailed studies performed on the behaviour of pure calcia, results that can be considered to be well established after the current investigation. Such
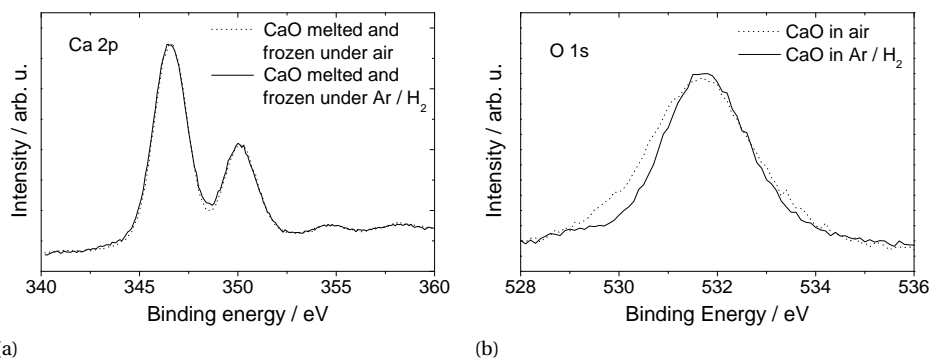
Figure 2.12: X-ray photo-electron spectra (XPS) of Ca 3p (a) and O 2s (b) in CaO samples laser melted and refrozen in air (dotted curves) and in Ar + 6% H_2 (dashed curves). No clear differences are detectable following the formation of colour centres in CaO, nor signs of any possible formation of metallic Ca.
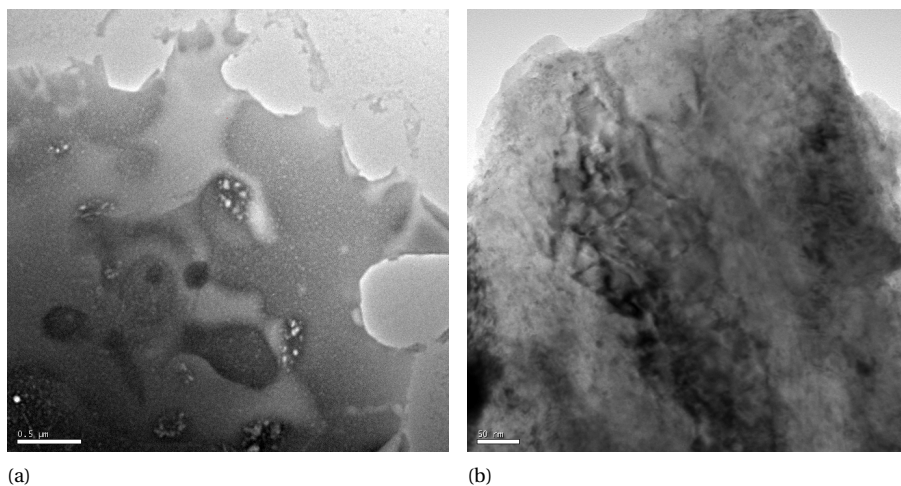
Figure 2.13: Transmission electron microscopy (TEM) images of CaO melted and refrozen in Ar + 6% H_2. No signs of the formation of metallic Ca or defective CaO are detectable.

2

an apparent paradox can be overcome by considering that calcia is most probably richer in defects in such multi-nary phase diagrams in the vicinity of the solid/liquid transition. In fact, the formation of defects and colour centres, resulting in a lower melting/freezing point, is most likely fostered in a mixture of calcia with other oxides or metals. As an example, a similar behaviour was experimentally reported by Foex [12] for the case of SrO, whose melting/solidification point was reduced by over 400 K when measured in a solid solution with just 10 mol% of WO_3. Still, further systematic research is certainly needed on the solid/liquid equilibria of CaO mixed with small amounts of other oxides or metals in order to fully understand the large difference between the high- and low-melting points reported in the literature for pure calcia. These kinds of systems should be analysed taking into account the existence of defective, or even hypo-stoichiometric calcia at very high temperature. Thus supposedly pseudo-binary systems including CaO as one end member and another metal oxide as the other end member should be better studied in the full ternary diagram calcium-metal-oxygen. This reproduces a situation similar to the one recently assessed for the ternary UPuO system, where the pseudo-binary plane UO_2PuO_2 is not sufficient for a complete description of the condensed phase behaviour at temperatures around the melting transition [52, 53].

2.5. CONCLUSION

I N the present work, the melting/freezing behaviour of calcium oxide has been studied by laser heating and fast pyrometry under controlled atmosphere. The influence of the atmospheric conditions on this controversial solid/liquid transition has thus been dealt with for the first time, at least in the authors knowledge. Despite the complex optical behaviour of calcia at increasing temperature, the current research has yielded consistent results that can be summarised in the following conclusions:

CaO melts congruently around 3200 K (3222 K ± 25 K according to the present data) under strongly oxidising conditions (air at atmospheric pressure or compressed up to 0.3 MPa). Under a reducing atmosphere, the solid/liquid transition occurs in calcia at a lower, poorly reproducible temperature at 3192 K ± 40 K.

Although defects have been detected in both cases in the material at high temperature, they are more numerous and their absorption effects more intense in samples heated and cooled under a reducing atmosphere. Such samples even display a much darker colour after the melting/freezing cycle, attributable to the formation of oxygen-defect-related colour centres in the re-solidified material.

The formation of defects in calcia at high temperature, particularly under reducing conditions, leads to a thermodynamic stabilisation of the liquid up to lower temperatures and, consequently, to a depression of the melting/solidification point. This aspect cannot be ignored in the optimisation of pseudo-binary and multi-nary phase diagrams including CaO as one of the end members, particularly in mixed systems where the formation of oxygen defects can be chemically or physically fostered.

This last point, in particular, has already been raised for other metaloxygen systems, and should encourage further research in order to fully explain the large discrepancies existing in the literature data on the melting behaviour of CaO, and understand the complex high-temperature behaviour of refractory oxides in general. Besides a deep comprehension of the safety performance limits of refractory oxides in several technological

applications, such a research field has a potentially high impact in many different disciplines where these compounds are exposed to high temperatures and extreme conditions. For example, data about calcium monoxide melting have a fundamental importance in understating the high temperature behaviour of lime-based minerals. Moreover, the present spectroscopic observation of burnt lime optical properties under different conditions will be useful in the study of rocks and gases containing this compound, and, possibly, also in the determination of the nature of their chemical environment.

2.6. APPENDIX: RADIANCE PROPERTIES

A material at temperature T (in K) exchanges with the surrounding environment a spectral radiance $L_{\lambda bb}$ [28]. For a black-body (defined as an ideal absorber and an ideal emitter) at the thermodynamic equilibrium $L_{\lambda bb}$ obeys Plancks law at any wavelength λ:

$$L_{\lambda bb}(T) = \frac{c_{1L}}{n^2 \cdot \lambda^5} \cdot \left[\exp\left(\frac{c_2}{n \cdot \lambda \cdot T} \right) - 1 \right]^{-1} \tag{2.4}$$

where $c_{1L} = 2hc_0^2$ is the first radiation constant and $c_2 = hc_0k_B$ is the second radiation constant. c_0 is the speed of light in vacuum, h Plancks constant, and k_B Boltzmanns constant. For the purposes of the present work, the index of refraction is always taken to be equal to 1 (being the current medium air or an inert gas close to atmospheric pressure).

For a real body, the radiance intensity exchanged (absorbed or emitted) is related to that of a black-body at the same temperature by the sample emissivity ϵ. This latter is equivalent, at the thermodynamic equilibrium, to the absorptivity a, according to Kirchhoffs theorem. At a fixed wavelength spectral absorptivity a_λ and spectral emissivity ϵ_λ are used instead of the total parameters. Since pyrometers in the present work are always set up near normal to the sample surface, the angle dependence of ϵ_λ is not considered and, emissivity always refers to normal spectral emissivity (NSE). The radiative intensity emitted by a real body of emissivity ϵ_λ is compared to that of an ideal black-body at the same temperature through the following identities:

$$L_\lambda = \epsilon_\lambda \cdot L_{\lambda bb} = \frac{1}{\lambda^5} \cdot \frac{\epsilon_\lambda}{e^{c_2/\lambda T} - 1} = \frac{1}{\lambda^5} \cdot \frac{1}{e^{c_2/\lambda T} - 1} \tag{2.5}$$

T_λ, called the radiance temperature, is the temperature at which a perfect blackbody source would emit the same thermal radiation as the sample under investigation at a given wavelength λ. It is therefore a function of the real sample temperature T, emissivity ϵ_λ and the wavelength. Since the following relation holds (τ_λ being the sample transmissivity and ρ_λ its reflectivity) :

$$\epsilon_\lambda + \tau_\lambda + \rho_\lambda = 1 \tag{2.6}$$

a low-emissivity (low-absorptivity) material is not necessarily only transparent but can also be reflective at the wavelength of interest.

A material whose ϵ_λ is independent of the wavelength is called a grey body (GB). Such behaviour is in general more common to insulators, like calcia and many other oxides, than it is to metallic materials.

In the current research, experimental L_λ curves are fitted by a non-linear parametric function of the type reported in Eq. 2.5. The free parameters are the emissivity ϵ_λ (which can in turn depend on more parameters) and the real temperature T. In the case of melting and freezing CaO, $\exp(c_2/\lambda T) \gg 1$, and Wiens approximation to Plancks law can be applied [28], resulting in Eq. 2.2 of Section 2.1.2:

$$\frac{1}{T_\lambda} = \frac{1}{T} - \frac{\lambda}{c_2} \cdot \ln \epsilon_\lambda \tag{2.7}$$

According to this simpler equation, the regular (close to GB) behaviour of the emissivity of CaO at high temperature can thus be visually checked by plotting the inverse experimental radiance temperature data vs. wavelength. It is then obvious that a GB behaviour will correspond to an increasing straight line in the resulting graph (because $\epsilon_\lambda \leq 1$), and the NSE will be closer to 1 (black body behaviour), the smaller the slope of the curve. Such a visual approach has been used in the current research in order to cross-check radiance data and compensate for the already mentioned poor numerical stability of the emissivity analysis [34].

REFERENCES

[1] D. Manara, R. Böhler, L. Capriotti, A. Quaini, Z. Bao, K. Boboridis, L. Luzzi, A. Janssen, P. Pöml, R. Eloirdi, and R. Konings, *On the melting behaviour of calcium monoxide under different atmospheres: A laser heating study,* J. Eur. Ceram. Soc. **34**, 1623 (2014).

[2] N. N. Greenwood and A. Earnshaw, *Chemistry of the Elements* (Pergamon Press, 1994).

[3] M. B. Boslough, T. J. Ahrens, and A. C. Mitchell, *Shock temperatures in CaO,* J. Geophys. Res. **89**, 7845 (1984).

[4] X. Sun, T. Song, Y. Chu, Z. Liu, Z. Zhang, and Q. Chen, *The high-pressure melting curve of CaO,* Solid State Commun. **150**, 1785 (2010).

[5] C. Hellwig, M. Streit, P. Blair, T. Tverberg, F. Klaassen, R. Schram, F. Vettraino, and T. Yamashita, *Inert matrix fuel behaviour in test irradiations,* J. Nucl. Mater. **352**, 291 (2006).

[6] C. Lombardi, L. Luzzi, E. Padovani, and F. Vettraino, *Thoria and inert matrix fuels for a sustainable nuclear power,* Prog. Nucl. Energy **50**, 944 (2008).

[7] R. E. Bedford, G. Bonnier, H. Maas, and F. Pavese, *Recommended values of temperature on the International Temperature Scale of 1990 for a selected set of secondary reference points,* Metrologia **33**, 133 (1996).

[8] T. Yamada, M. Yoshimura, and S. Somiya, *Reinvestigation of the Solidification Point of CaO by Digital Pyrometry,* J. Am. Ceram. Soc. **69**, C (1986).

[9] T. Noguchi, M. Mizuno, and W. M. Conn, *Fundamental research in refractory system with a solar furnace - ZrO_2 -CaO system,* Sol. Energy **11**, 145 (1967).

[10] Z. Panek, *Melting temperatures of MgO and CaO,* Silikaty **23**, 97 (1979).

[11] V. Shevchenko, L. Lopato, A. Stegny, and V. Gerasimyuk, G.I. Dvernyakov, V.S. Pasichnys, *Liquidus of the HfO$_2$-MgO and HfO$_2$-CaO systems,* Dokl Akad Nauk SSSR, Ser A **8**, 682 (1979).

[12] M. Foex, *Measurement of the solidification points of several refractory oxides by means of a solar furnace,* Sol. Energy **9**, 61 (1965).

[13] J. Hlaváč, *Melting temperatures of refractory oxides,* Pure Appl. Chem. **54**, 681 (1982).

[14] M. Chase, *NIST-JANAF, Thermochemical Tables, Fourth Edition, Part I,* J Phys Chem Ref Data **Monograph**, 729 (1998).

[15] H. A. Wriedt, *The CaO (Calcium-Oxygen) system,* Bull. Alloy Phase Diagrams **6**, 337 (1985).

[16] A. D. Pelton and M. Blander, *Thermodynamic analysis of ordered liquid solutions by a modified quasichemical approach - Application to silicate slags,* Metall. Trans. B **17**, 805 (1986).

[17] P. Wu, G. Eriksson, and A. D. Pelton, *Critical Evaluation and Optimization of the Thermodynamic Properties and Phase Diagrams of the CaO-FeO, CaO-MgO, CaO-MnO, FeO-MgO, FeO-MnO, and MgO-MnO Systems,* J. Am. Ceram. Soc. **76**, 2065 (1993).

[18] D. Jerebtsov and G. Mikhailov, *Phase diagram of CaOAl$_2$O$_3$ system,* Ceram. Int. **27**, 25 (2001).

[19] A. I. Zaitsev and B. M. Mogutnov, *Thermodynamics of the Ca-CaO-CaF$_2$ system,* Metall. Mater. Trans. B **32**, 305 (2001).

[20] D. Lindberg and P. Chartrand, *Thermodynamic evaluation and optimization of the (Ca+C+O+S) system,* J. Chem. Thermodyn. **41**, 1111 (2009).

[21] M. Hillert and W. Xizhen, *Thermodynamic calculation of the CaO-MgO system,* Calphad **13**, 267 (1989).

[22] M. Hillert, B. Sundman, and X. Wang, *An assessment of the CaO-SiO$_2$ system,* Metall. Trans. B **21**, 303 (1990).

[23] W. Huang, M. Hillert, and X. Wang, *Thermodynamic assessment of the CaO-MgO-SiO$_2$ system,* Metall. Mater. Trans. A **26**, 2293 (1995).

[24] B. Hallstedt, *Assessment of the CaO-Al$_2$O$_3$ System,* J. Am. Ceram. Soc. **73**, 15 (1990).

[25] H. Yu, Q. Chen, and Z. Jin, *Thermodynamic assessment of the CaOB$_2$O$_3$ system,* Calphad **23**, 101 (1999).

[26] V. Sokolov, *Calcoluminescence,* Usp Fiz Nauk **47**, 538 (1952).

2

[27] V. V. Kubarev, *Features of the drummond light of calcium oxide,* Opt. Spectrosc. **106**, 242 (2009).

[28] D. P. DeWitt and J. C. Richmond, *Thermal Radiative Properties of Materials,* in *Theory Pract. Radiat. Thermom.*, edited by D. P. DeWitt and G. D. Nutter (John Wiley & Sons, Inc., 1988).

[29] D. Bevan and F. Richardson, *The solution of lime and liquid calcium,* in *Proc. Aust. At. Energy Symp. Peac. Uses At. Energy, Aust. At. Energy Comm.* (1958) pp. 586–587.

[30] D. Manara, M. Sheindlin, W. Heinz, and C. Ronchi, *New techniques for high-temperature melting measurements in volatile refractory materials via laser surface heating,* Rev. Sci. Instrum. **79**, 113901 (2008).

[31] R. Böhler, M. J. Welland, F. D. Bruycker, K. Boboridis, A. Janssen, R. Eloirdi, R. J. M. Konings, and D. Manara, *Revisiting the melting temperature of NpO_2 and the challenges associated with high temperature actinide compound measurements,* J. Appl. Phys. **111**, 113501 (2012).

[32] H. Preston-Thomas, *The International Temperature Scale of 1990 (ITS-90),* Metrologia **27**, 3 (1990).

[33] H. Preston-Thomas, *The International Temperature Scale of 1990 (ITS-90),* Metrologia **27**, 107 (1990).

[34] G. Neuer, L. Fiessler, M. Groll, and E. Schreiber, *Critical analysis of the different methods of multiwavelength pyrometry,* in *Temp. Its Meas. Control Sci. Ind. Vol. 6* (AIP, New York, 1992).

[35] M. Dadsetani and R. Beiranvand, *Optical properties of alkaline-earth metal oxides from first principles,* Solid State Sci. **11**, 2099 (2009).

[36] D. Manara, C. Ronchi, M. Sheindlin, M. Lewis, and M. Brykin, *Melting of stoichiometric and hyperstoichiometric uranium dioxide,* J. Nucl. Mater. **342**, 148 (2005).

[37] K. M. Sancier, D. J. Schott, and H. Wise, *Luminescence of Solids Excited by Surface Recombination of Atoms. IV. Mechanisms of Excitation and Luminescence,* J. Chem. Phys. **42**, 1233 (1965).

[38] B. Henderson, S. Stokowski, and T. Ensign, *Luminescence from F Centers in Calcium Oxide,* Phys. Rev. **183**, 826 (1969).

[39] B. Henderson, Y. Chen, and W. Sibley, *Temperature Dependence of Luminescence of F^+ and F Centers in CaO,* Phys. Rev. B **6**, 4060 (1972).

[40] J. Bates and R. Wood, *Luminescence spectrum of the f-center in CaO,* Phys. Lett. A **49**, 389 (1974).

[41] J. Bates and R. Wood, *High temperature luminescence spectra from F-centers in CaO,* Solid State Commun. **17**, 201 (1975).

[42] J. Feldott and G. Summers, *Photoconductivity and luminescence of electron irradiated CaO,* Phys. Rev. B **16**, 1722 (1977).

[43] J. Park, Y. Chen, G. Williams, R. Williams, and G. Pogatshnik, *Luminescence of F+ centers in CaO crystals under pulsed-laser excitation,* Phys. Rev. B **43**, 11991 (1991).

[44] J. Carrasco, C. Sousa, F. Illas, P. V. Sushko, and A. L. Shluger, *Optical absorption and luminescence energies of F centers in CaO from ab initio embedded cluster calculations.* J. Chem. Phys. **125**, 074710 (2006).

[45] K. Rieder, B. Weinstein, M. Cardona, and H. Bilz, *Measurement and Comparative Analysis of the Second-Order Raman Spectra of the Alkaline-Earth Oxides with a NaCl Structure,* Phys. Rev. B **8**, 4780 (1973).

[46] Z. Padanyi, *The Raman spectrum of Ca(OH)2,* Solid State Commun. **8**, 541 (1970).

[47] P. E. Halstead and A. E. Moore, *The thermal dissociation of calcium hydroxide,* J. Chem. Soc. , 3873 (1957).

[48] C. Ronchi and M. Sheindlin, *Melting point of MgO,* J. Appl. Phys. **90**, 3325 (2001).

[49] M. Zinkevich, D. Djurovic, and F. Aldinger, *Thermodynamic modelling of the cerium-oxygen system,* Solid State Ionics **177**, 989 (2006).

[50] F. De Bruycker, K. Boboridis, D. Manara, P. Pöml, M. Rini, and R. J. Konings, *Reassessing the melting temperature of PuO$_2$,* Mater. Today **13**, 52 (2010).

[51] C. Ronchi, I. L. Iosilevski, and E. S. Yakub, *Equation of State of Uranium Dioxide* (Springer Berlin Heidelberg, Berlin, Heidelberg, 2004).

[52] F. De Bruycker, K. Boboridis, R. Konings, M. Rini, R. Eloirdi, C. Guéneau, N. Dupin, and D. Manara, *On the melting behaviour of uranium/plutonium mixed dioxides with high-Pu content: A laser heating study,* J. Nucl. Mater. **419**, 186 (2011).

[53] C. Guéneau, N. Dupin, B. Sundman, C. Martial, J.-C. Dumas, S. Gossé, S. Chatain, F. D. Bruycker, D. Manara, and R. J. Konings, *Thermodynamic modelling of advanced oxide and carbide nuclear fuels: Description of the U-Pu-O-C systems,* J. Nucl. Mater. **419**, 145 (2011).

3

REVISITING THE MELTING TEMPERATURE OF NPO₂

Robert BÖHLER, **Micheal J.** WELLAND, **Franck**
DEBRUYCKER, **Konstantinos** BOBORIDIS, **Arne** JANSSEN,
Rachel ELOIRDI, **Rudy J.M.** KONINGS, **Dario** MANARA

This work revisits the melting behaviour of neptunium dioxide, an actinide compound which can be produced in the nuclear fuel during operation, and which has an important impact on the nuclear fuel and waste radioactivity especially on the very long term. The present experimental approach employs remote laser heating under controlled atmosphere and fast pyrometry. This technique circumvents problems encountered by more traditional heating techniques, in particular, the reaction between sample and containment at temperatures beyond 2500 K. In addition, only a small amount of sample material is required, which is an advantage with respect to the radioactivity and limited availability of neptunium. The NpO₂ melting/freezing temperature has been measured to be 3070 ± 62 K, much higher than previous values (around 2830 K) obtained by more traditional thermal analysis methods. The large amount of experimental data collected allowed a consistent statistical analysis. It seems likely, although not fully evident from the present results, that the high oxygen potential at temperatures around melting leads to a slightly hypo-stoichiometric congruent melting composition, as already observed in other actinide (ThO₂, PuO₂) and lanthanide oxides (e.g., CeO₂). Finally, a recently developed phase-eld model was used for the simulation of the observed thermograms, allowing a deeper insight in material properties that are difcult to directly measure. For example, a polaron contribution to the high-temperature thermal conductivity, well accepted for the commonly studied actinide oxide UO₂, is shown here to likely be present in NpO₂.

3.1. INTRODUCTION

NEPTUNIUM is the first transuranic element. Its most stable isotope, ^{237}Np (half-life = 2.144·10^6 yr), is formed in a nuclear reactor either by α-decay of ^{241}Am or by neutron capture of ^{235}U

$$^{235}U + n \xrightarrow{\gamma} {}^{236}U + n \longrightarrow {}^{237}U \xrightarrow{\beta^-, 6.75d} {}^{237}Np \ .$$
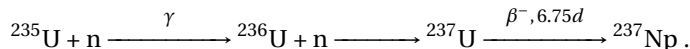
It is therefore produced as a by-product in nuclear reactors. Due to its long half life, it contributes significantly to the long-term activity of nuclear waste, and is therefore one of the most interesting target nuclides for removal by nuclear transmutation like in the minor actinide burndown or deep-burn concepts [2]. Knowledge of properties of Np compounds[3] is therefore important for actinide management technologies, as well as from a fundamental research viewpoint. Particularly, the NpO2 melting temperature is important basic information in the actinide dioxide series, which will possibly help, among other aspects, the understanding of the 5f electron behaviour in these compounds.

Two melting point measurements of NpO$_2$ were published prior to the present work by Chikalla et al. [4] in 1971 and by Richter and Sari [5] in 1987. In both cases, specimens were heated up to the melting point in a resistance furnace and the temperature was measured by pyrometry under blackbody conditions. The melting points reported in these two publications are in excellent agreement, 2830 ± 65 K and 2820 ± 66 K, respectively. Both results may, however, be affected by the high reactivity of the sample, particularly in the liquid phase, at elevated temperature. The present investigation aims at repeating these measurements with an innovative fast heating method, based on high power laser irradiation of the sample coupled with fast multi-channel pyrometry. This method allows the reduction of the heating/cooling duration by orders of magnitude (down to several tens of milliseconds), and the concomitant side effects linked to prolonged high temperatures. Moreover, the atmosphere in which the sample undergoes the solid/liquid phase transition may be controlled.

This technique, developed at the European Commissions JRC-ITU in Karlsruhe (Germany), was already successfully used to study the melting behaviour of some actinide compounds like PuO$_2$ [6], UC [7],UO$_2$ [8], whereby the obtained results were sometimes in disagreement with previous literature data based on more traditional heating techniques. This was especially true for oxides, due to their high oxygen potential at temperatures close to melting, whereas the measurements conducted on carbides often yielded results in good agreement with the existing databases. In this context, it appeared that most actinide-oxygen phase boundaries should be revisited, especially at high temperature [9]. It seemed then of great interest to apply the current experimental approach to neptunium dioxide.

A sound interpretation and thorough exploitation of the current experimental temperature vs. time curves were achieved by simulation with a heat transport and a phase-field model. This is an original theoretical approach derived through the theory of irreversible processes [10].

3.2. Experimental procedure and modelling

3.2.1. Sample preparation

The neptunium dioxide samples were prepared with a mass fraction w(^{235}Np) of 99.87%, traces of ^{241}Am ^{238}Pu with mass fractions less than 0.0002% (measured by alpha spectroscopy), w(W) = 0.0276%, and w(P) = 0.05%. The starting material was a powder. Disks 6 mm in diameter and 1.2 to 1.5 mm in thickness were obtained using a bi-directional press. They were then sintered for 8 h in an Ar/H_2 flux at 1973 K with approximately 1500 ppm of H_2O to densify them, then heat-treated twice in air for 8 h at 1123 K, following Richter and Sari's procedure [5], and for 12 h at 2000 K just before the laser experiments in order to obtain a composition as close as possible to the exact O/Np = 2 stoichiometry. No weight change was observed after a second annealing, and this was considered a satisfactory test that the stoichiometric composition (O/Np = 2) had been reached.

3.2.2. High temperature measurements
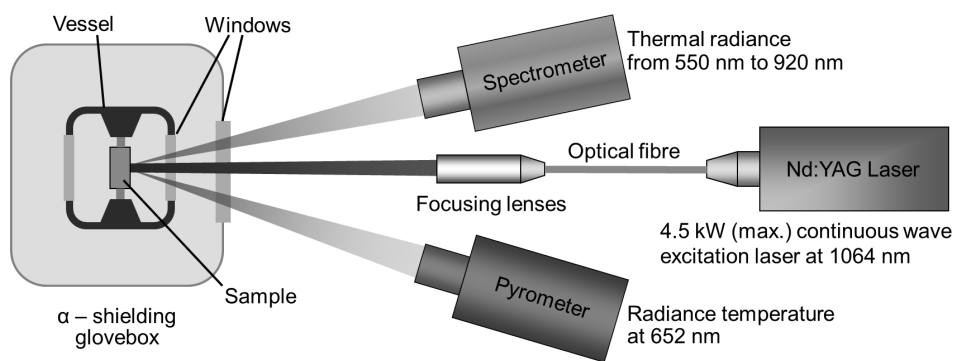
Figure 3.1: A scheme of the experimental apparatus used to conduct the melting experiments by laser heating and fast multi-channel pyrometry in the current work.

The experimental apparatus used in this work is summarised in Figure 3.1 and described in detail elsewhere [11]. The sample was mounted in a pressurized cell with a controlled atmosphere inside a a-shielding glove-box. The contact between the sample and its mount was minimized by using three radially arranged graphite screws to hold the sample in place. The heating agent was a Nd:YAG continuous-wave laser radiating at 1064.5 nm. The laser is programmable with a complex power/time profile of variable duration as short as a few milliseconds and a maximum power of 4.5 kW. Pulses of 70 ms to 720 ms consisted of an initial power ramp, designed to reduce the thermal shock, followed by a constant-power plateau. The sample was heated beyond the melting point and then allowed to cool naturally and re-solidify. Such heating cycles were performed under air, air mixed with argon, and Ar + 2%H_2 slightly pressurized up to 0.3 MPa. Quasi-containerless conditions were achieved by directly heating only a limited area of approximately 3 mm in diameter on the sample surface. The molten volume was therefore contained by the outer periphery of colder solid material, thus, preventing contamination by foreign material. Several experimental parameters could be varied in

order to check the impact of the different factors (atmosphere, heating cycle duration, laser spot size, etc.) on the observed melting behaviour.

The surface radiance temperature in the centre of the heated zone was measured by a pyrometer equipped with a fast logarithmic amplifier, operating at 652 nm. The nominal spot size was approximately 0.5 mm in diameter. The pyrometer was calibrated against a standard tungsten-ribbon lamp in the range 1800 K to 2500 K, ensuring traceability to the International Temperature Scale of 1990 [12]. The validity of the calibration, the quality of the optical windows, the alignment, and the thermodynamic equilibrium conditions on the measurement spot were tested by measuring in-situ the well established melting radiance temperatures of molybdenum, tungsten, and UO$_2$ (2530 K [13], 3207 K [13], and 3040 K [8], respectively, close to 650 nm).

In addition, a spectro-pyrometer, based on a linear array of 256 photodiodes was used to record the thermal radiance emitted by the sample in the range 550nm to 920 nm. This instrument allows a spectral analysis, although with a poorer time resolution (one spectrum per millisecond at best). The photodiode at 649nm was calibrated up to 2500 K using the tungsten-ribbon lamp and this calibration was transferred to a tubular-cavity variable-temperature graphite blackbody-furnace up to 3300 K. The remaining photodiodes were then calibrated with this blackbody, allowing a conversion of their output signal to spectral radiance over the useful wavelength range.

The measured radiance spectra can be fitted in two physically equivalent methods: by a least-squares regression to Planck's distribution law modified by a wavelength and temperature dependent function assumed to represent the (near) normal spectral emittance (NSE), $\epsilon(\lambda, T)$, of NpO$_2$, or by the radiance temperature, $T_r(\lambda)$, measured during the freezing arrest and plotted as a function of wavelength, λ. The obtained curves were then fitted using Wiens approximation of Planck's law, which is accurate to better than 1% for $\lambda T < 3100 \mu m K$

$$\frac{1}{T_r(\lambda)} = \frac{1}{T} - \frac{\lambda}{c_2} \cdot \ln \epsilon(\lambda, T) \,, \tag{3.1}$$

where T is the true temperature, c_2 = 14 388 $\mu m K$ is the second radiation constant. If ϵ is independent of wavelength or at least constant at the wavelengths at which T_r is measured, then plotting $1/T_r$ as a function of λ results in a straight line fit. When extrapolated to zero wavelength [14], it intersects the inverse temperature axis at the inverse true temperature 1/T, as in Eq. 3.1. In the present work, this approximation of the wavelength-independent NSE (greybody behaviour) resulted in a good fit and was therefore adopted. This is also supported by analogy to emittance data of other similar dioxides (such as UO$_2$ [15], and PuO2 [6]). In particular, the emittance values thus obtained for liquid and solid NpO$_2$ agreed well with those already published for UO$_2$ [15] and PuO$_2$ [6]. The best estimate for the greybody-NSE was then used to convert the measured radiance temperature to true temperatures. Since all measurements were taken on liquid or re-solidified material, the surface was considered to be sufficiently smooth, as supported by the good repeatability of the measured radiance temperatures upon freezing.

The melting/freezing temperature of NpO$_2$ was determined from the cooling stage of the recorded thermograms, by locating the corresponding thermal arrest. As often observed in rapid laser-heating experiments of such materials, and confirmed by nu-

merical simulation, the heating stage often occurs too quickly to reveal an observable melting arrest during this phase of the thermal cycle.

3.2.3. MATERIAL ANALYSIS

NpO2 samples were analysed by x-ray diffraction (XRD) on the unmolten and resolidified areas with a diffractometer (Cu-$K_{\alpha 1}$ radiation), using a range 10-120 ° using 0.009° steps. Secondary electron (SE) and backscattered electron (BSE) images were recorded on a scanning electron microscope (SEM) operated at 25 kV.

3.2.4. NUMERICAL SIMULATION

Experimental heating cycles were simulated using a phase-field model to account for the phase change. The model determines the thermal transport coupled with phase stability through a phase-field model which tightly links the kinetic model to equilibrium thermodynamic treatments of the material. Similar models were previously used on thermograms from UO_{2+x}, which melt non-congruently [16].

The phase-field model introduces a scalar state variable φ representing the fraction of the stable phase at each physical point of the system (e.g., $\varphi = 1$ for the liquid, $\varphi = 0$ for the solid, $\varphi \in (0,1)$ for a coexistence of the two). This approach permits a versatile description of the system including representation of phase boundaries with diffuse interfaces, whereas its main drawback is large computational expense, resulting in long calculation times.

The model is described in Eq. 3.2 and 3.3 and was implemented in the finite element method software, COMSOL® Multiphysics:

$$\underbrace{\rho \, c_p \, \frac{\mathrm{D}T}{\mathrm{D}t}}_{\substack{\text{Energy due to} \\ \text{temperature increase}}} = - \underbrace{\rho \, h_{\text{fus}} \, \frac{\mathrm{D}\varphi}{\mathrm{D}t}}_{\substack{\text{Latent heat of} \\ \text{phase change}}} - \underbrace{\nabla \cdot \vec{q}}_{\substack{\text{Heat conduction}}} \, , \tag{3.2}$$

$$\underbrace{\frac{\mathrm{D}T}{\mathrm{D}t}}_{\substack{\text{Rate of} \\ \text{phase change}}} = - \underbrace{\frac{M_\varphi}{T}}_{\substack{\text{Interface} \\ \text{kinetics}}} \left(- \underbrace{\rho \frac{h_{\text{fus}}}{T_{\text{fus}}} (T - T_{\text{fus}})}_{\substack{\text{Approximate change in} \\ \text{entropy at constant volume}}} + \underbrace{\frac{\partial K(\varphi)}{\partial \varphi} - \xi^2 \vec{\nabla}^2 \varphi}_{\substack{\text{Interface shaping terms}}} \right) , \tag{3.3}$$

where c_p represents the constant pressure heat capacity, ρ is the density, q is the conductive heat flux, h_{fus} is the enthalpy of fusion, M_φ is the interface attachment kinetic parameter, T_{fus} is the temperature of fusion, and K and ξ are interface shaping terms required by the phase-field model. Thermal boundary conditions are laser absorption and radiative heat loss. Heat transport in the buffer gas was modelled simultaneously to account for heat loss from the sample.

Many of the material parameters required as input for the model are unknown, especially at the very high temperatures encountered at the liquid state. Missing parameters were therefore extrapolated from lower temperatures or taken from UO_2 when no other information was available. The enthalpy of fusion was calculated using Richards law [17–19]. The material properties used are listed in Table 3.1. Preliminary simulations revealed a discrepancy with the experimental data, which motivated a deeper investigation of the material properties. An important point was noted in the high high temper-

Material property	Unit	Value	Reference
Density at 293 K	$\dfrac{\text{kg}}{\text{m}^3}$	11192.8	Sobolev [19]
Enthalpy of fusion	$\dfrac{\text{J}}{\text{mol}}$	77320	This work
Heat capacity solid	$\dfrac{\text{J}}{\text{mol K}}$	$11.4 + 1.59 \cdot 10^{-1}\ (T/K)$ $-1.33 \cdot 10^{-4}\ (T/K)^2 + 5.21 \cdot 10^{-8}$ $(T/K)^3\ -6.67 \cdot 10^{-12}\ (T/K)^4$	Kurosaki [20]
Heat capacity liquid	$\dfrac{\text{J}}{\text{mol K}}$	$\dfrac{1.3288 \cdot 10^9}{(T/K)^2} + 0.25136$	Fink [21]
Thermal conductivity solid	$\dfrac{\text{W}}{\text{m K}}$	$\dfrac{1}{0.09447 + 1.79710^{-4}(T/K)}$ $+\left(\dfrac{2.024 \cdot 10^{11}}{(T/K)^{5/2}}\, e^{\frac{-16350}{(T/K)}} \right)$	Nishi [22]
Thermal conductivity liquid	$\dfrac{\text{W}}{\text{m K}}$	2.6	Sheindlin [23]
Absorptivity	-	0.829	This work
Emissivity	-	0.829	This work

Table 3.1: Material properties used as input parameters in the simulation. The term in brackets in the solid thermal conductivity is the polaron terms added as discussed in the text.

ature thermal conductivity of NpO_2, which exhibited a downward trend with increasing temperature, whereas UO_2 and MOX typically show an upswing due to polarons [23, 24]. Upon deeper examination, experiments on the thermal conductivity of NpO_2 were preformed only up to 1473 K [22] and show a decreasing trend with temperature, in qualitative agreement with molecular dynamics calculations up to 2200 K [20]. However, the calculations only consider lattice terms, and the measurements are below the threshold of significant polaron contribution in UO_2. Therefore, we add the UO_2 polaron term [21] to the lattice terms for the thermal conductivity of NpO_2.

3.3. Results

3.3.1. Laser heating
Two NpO_2 disks were investigated in the present work. When the sample broke into pieces during the experiment, suitably large fragments were also used as further specimens. In total, more than 40 laser heating experiments were carried out, allowing a meaningful statistical analysis of the results. A clear solidification arrest was detected in a well reproducible temperature range, both over many successive shots on the same specimen and on different samples (Figure 3.2). No indication of segregation or non-congruent evaporation was detectable from such thermal analysis only. Solidification plateaus were sometimes preceded by a dip in temperature as a consequence of under-
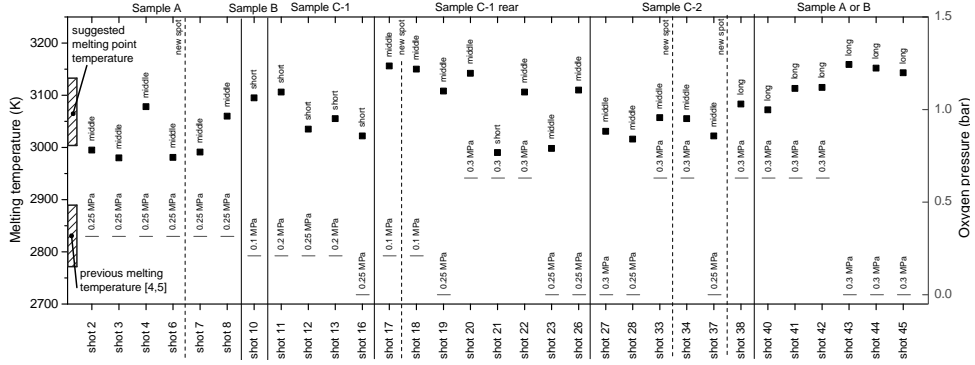
Figure 3.2: An overview of all the solidification points measured in NpO$_2$ samples in this work, together with the partial oxygen pressure and the total pressure set in each experiment. The missing laser irradiation experiments were not taken into consideration for the statistics, but still had an effect on the morphology of the sample surface. Several shots were performed on the same spot on each sample. The experiments are categorized according to the total heating duration (short: t < 100 ms, middle: 100 ms ≤ t ≤ 150 ms, long: t > 150 ms). Older literature values of the NpO$_2$ melting temperature with their uncertainties are compared with the result found in this work (3070 K ± 62 K).
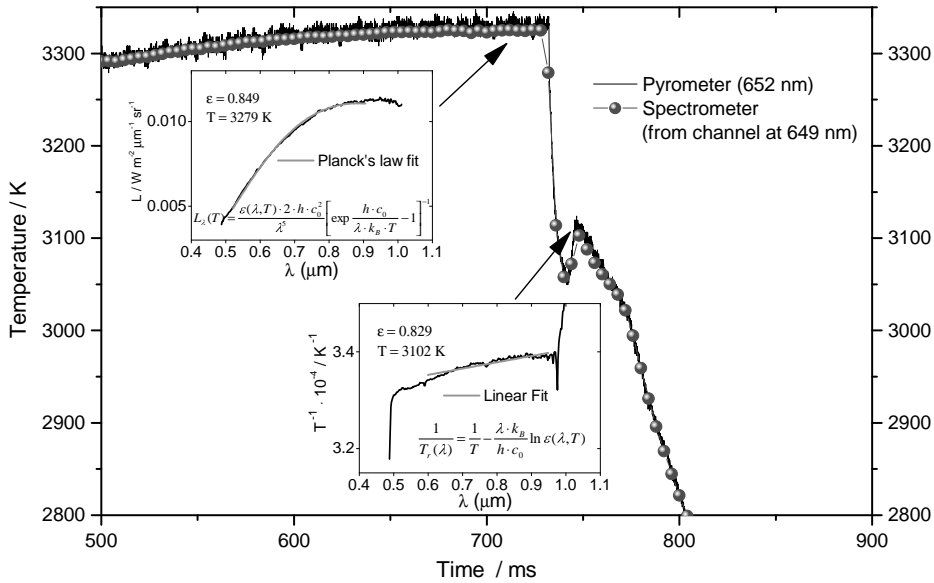
Figure 3.3: Typical thermograms recorded at 649 nm (full circles) and 652 nm (solid line) on a laser heated NpO$_2$ sample (shot 42) by the spectro-pyrometers used in this work, using an average constant emissivity $\epsilon = 0.829$. The two insets show examples of radiance analysis. The first displays a Planck's law fit of an experimental radiance (L$_\lambda$) spectrum recorded in liquid NpO$_2$. The second reports a linear fit derived from Planck's law (Wien's approximation) of the inverse radiance temperature (T$_r^{-1}$) vs. wavelength observed at the NpO$_2$ solidification arrest. Both fits were performed, with temperature and emissivity as free parameters, in wavelength domains limited by the acceptability of the signal-to-noise ratio in the experimental curve. In both cases, a good fit was obtained with emissivity independent of temperature and wavelength (gray-body behaviour). c$_0$ = speed of light in vacuum; h = Planck's constant; k_B = Boltzmanns constant.

cooling at the surface of the sample which was reproduced in simulations described below.

The near-normal spectral emittance of freezing NpO$_2$ derived by multi-channel pyrometry using extrapolation to zero wavelength is reported in Figure 3.3. The radiance temperature spectrum, recorded during the freezing arrest with an integration time of 2 and 4 ms, is well fitted with a greybody (constant) emissivity of 0.829. An emissivity uncertainty of 0.08 (at the two standard deviation level) combined with the data spread and the temperature scale uncertainty (610 K) yields a NpO$_2$ freezing temperature of 3070 K $\pm$ 62 K. Such a temperature was observed to be reproducible, within the given uncertainty limits, over 31 experiments.
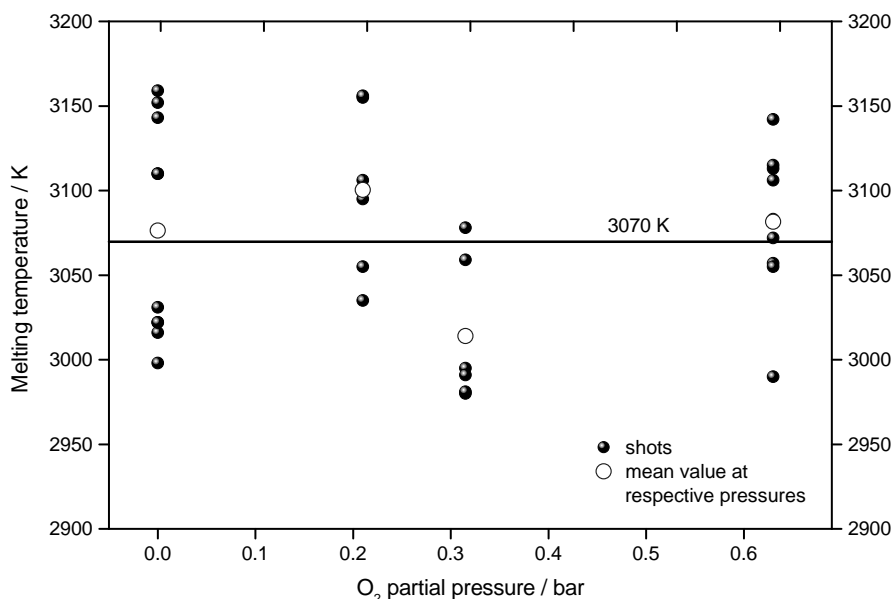
Figure 3.4: An overview of the currently measured NpO$_2$ solidification temperatures as a function of the O$_2$ partial pressure set in the buffer gas. The large empty circles represent the average solidification temperature determined at each oxygen partial pressure. The solid horizontal line represents the overall average solidification temperature.

By varying the atmosphere and the laser pulse power, no systematic variations of the melting point were observed as shown in Figure 3.4. All these effects have therefore been taken into account in defining the aforementioned uncertainty bands associated with the current results.

3.3.2. Material characterisation
The determination of possible permanent composition changes in the samples during the thermal cycles constituted a difficult part of the current investigation. Since no systematic effect linked to a variation of the O/Np ratio could be inferred from the thermal analysis of successive shots, other techniques were employed. Among them, the most

consistent seemed to be XRD, essentially because the dependence of the fcc-NpO_{2-x} lattice parameter on x has already been assessed for 0≤x≤0.04 by Richter and Sari [5]. No clear differences were observed between the diffraction of molten/refrozen neptunium dioxide and that of a not molten sample. The resulting lattice parameters were (5.4356 ± 0.002) Å and (5.4366 ± 0.002) Å, respectively. This corresponds with Richter and Sari [5] for a composition of $NpO_{1.995\pm0.010}$ for the molten and $NpO_{1.990\pm0.010}$ for the non-molten part. These values are very close to the suggested stoichiometric lattice parameter of 5.434 Å in the investigation of Richter and Sari, but a slightly lower O/Np ratio cannot be excluded. Other measurements of the lattice parameter suggest, nevertheless, a value of 5.4333 Å [25], so that the dependence of the composition has to be revisited.

The fact that samples were nearly stoichiometric both before and after laser irradiation was qualitatively confirmed also by SEM analysis. The electron microscope employed in the BSE mode revealed a clean surface throughout the sample, both in the molten/refrozen and in the unmolten regions, without any precipitations of metallic neptunium (Figure 3.5a), as found by Richter and Sari [5] in hypostoichiometric samples. From a morphological viewpoint, micrographs show that the depth of the molten zone was of the order of some tens of micrometers, and it can be separated from the bulk material by a crack parallel to the surface as shown in Figure 3.5b.
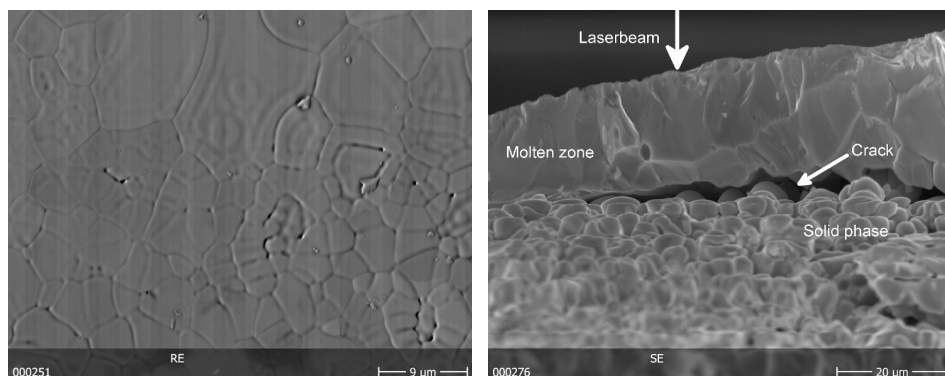
(a) SEM back scattered electron image of a molten and refrozen NpO_2 surface. The image shows a homogeneous surface where no second phases, especially metallic Np [5], can be distinguished by the contrast.

(b) A SEM cross section image of NpO2 laser-melted and refrozen. The surface molten part is clearly detached from the unmolten material underneath by a radial fracture (crack). This kind of cracks can have an important impact on the heat diffusion across of the sample, as they reduce the thermal conductivity.

Figure 3.5: SEM images of NpO_2

3.3.3. SIMULATIONS

The simulated thermogram presented in Figure 3.6 was computed with a 1D model of shot 22, for which the solidification temperature was recorded at 3100 K. Inputting the experimental laser power vs. time profile and using the material properties listed in Table 3.1, the calculated temperature evolution follows qualitatively well with the observed

3
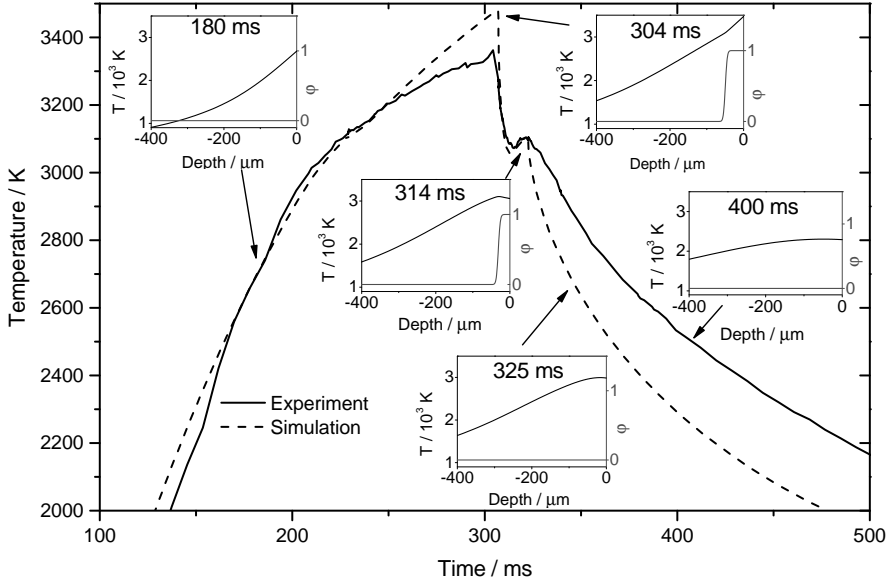
Figure 3.6: Comparison between an experimental thermogram (solid black line) recorded on a NpO$_2$ specimen laser-heated beyond melting (shot 22) and a calculated thermogram (dotted line) obtained from the 1-dimensional phase-field simulation of the same experiment. The insets show the temperature (T) and phase-field parameter (φ) as a function of depth at different time points during the heating-cooling cycle. In each inset, the region with $\varphi = 0$ corresponds to solid and the one with $\varphi = 1$ to liquid neptunium dioxide. The solid/liquid interface domain is characterized by intermediate values: $0<\varphi<1$.

temperatures. The insets in Figure 3.6 show the temperature and phase profiles at the indicated times as functions of depth into the material. The phase profile at 304 ms corresponds well to the depth of the refrozen liquid observed by SEM on a cross section of the sample as shown in Figure 3.6.

The difference in the cooling behaviour following the pulse is primarily attributed to the presence of cracks in the sample, generated by thermal stresses during heating and cooling. The cracks retard heat transport away from the surface, thus, slowing the apparent surface cooling rate.

Considering the uncertainty in the majority of the material properties, the thermogram is reasonably well reproduced, indicating that the properties used, including the polaron term in the thermal conductivity, are at least indicative of their correct values.

3.4. DISCUSSION

THE melting/freezing temperature observed by laser heating on NpO$_2$, 3070 ± 62 K, is more than 200 K higher than the value reported by Chikalla [4] and Richter and Sari [5]. These latter results were obtained by using traditional heating methods (resistance furnaces) with which the NpO$_2$ sample could extensively react with the tungsten containment during the long dwelling time (minutes) at high temperature. On the other hand, in the current work the apparent melting/freezing point did not increase when

performing repeated or longer experiments under oxidizing conditions. Since none of the techniques used to characterize the molten/refrozen material at room temperature gave evidence of any oxygen losses, except the XRD which indicated the possibility of a very slight hypostoichiometry both in the fresh and the laser irradiated materials, it can be concluded that neptunium dioxide melts congruently at a composition of $1.98 \leq O/Np \leq 2$. This agrees fairly well with available thermodynamic assessment of the Np-O phase diagram [5, 26], although the current investigation reveals a much higher melting temperature. Both the extent of the reported uncertainty band (662 K) and the (much larger) difference between the current results and the previous literature data give an idea of the experimental difficulties inherent in the high-temperature investigation of chemically reactive materials like NpO_2.

The qualitative agreement between the experimental and simulated thermograms is acceptable in that the main features of the process are reproduced. The approach constitutes a valuable tool yielding a deeper picture of heating/melting and the cooling/freezing process. In the absence of a flat temperature plateau during solidification, the simulation confirms and explains why the maximum temperature observed is the true freezing temperature of the material.

Another value of the simulation is the strong indication that polarons are present and contribute significantly to the thermal conductivity at high temperatures. With suitable development, the treatment may be used in the inverse problem for material parameter estimation (e.g., the thermal conductivity of liquid NpO_2).

In the end, devising a comprehensive approach (both experimental and theoretical) to obtain a satisfactory picture of all phenomena occurring under extreme experimental conditions constitute the main research challenges in the field of high temperature thermodynamics. This level of understanding is also of paramount importance for the analysis of accidental conditions which can be produced, for example, in a nuclear reactor or in nuclear waste during thermal excursions when insufficient cooling is provided.

Once more, a situation similar to that already observed elsewhere for CaO [27], CeO_2 [28], UO_{2+x}[8], and PuO_2 [6] is reproduced here: the reaction between the sample and its environment, enhanced by exchange of oxygen, probably leads to an apparent freezing temperature very different from the one measured for the well-controlled and well-contained material. The result is of great importance with respect to the behaviour of this sort of oxides, and highlights the impact of temperature and atmosphere on it.

The new value of the melting/solidification temperature for NpO_2 fits well in between the values for its neighbouring actinide oxides (UO_2,PuO_2). However, the general trend of the entire actinide dioxide series, reported in Figure 3.7 [4, 6, 8, 29–32] changes considerably when new values for NpO_2 and PuO_2 are taken into account instead of old ones. Figure 3.7 also shows that the difference between old and new melting temperatures of actinide dioxides increases with the atomic number of the actinide. More importantly, this difference seems to increase with the oxygen potential of the respective dioxide at a given temperature [33]. This shows the suitability of the current approach for the investigation of these materials, particularly in the cases where they display a strong tendency to exchange oxygen with their environment.

It is finally interesting to compare the qualitative behaviour of the room-temperature sublimation enthalpy $\Delta H_{sub}(298)$ [34–38] for the actinide dioxide series with the newly
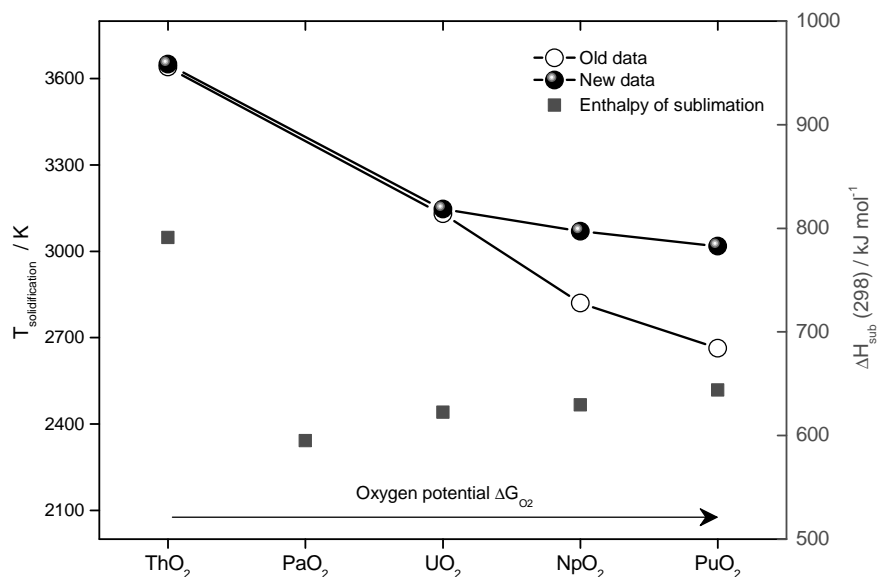
Figure 3.7: Comparison between old (induction furnace heating in a tungsten crucible) [4, 30–32] and new (quasi-containerless laser heating) [6, 8, 29] data points for the melting/solidification temperatures of dioxides of the actinide series. Data for the dioxides of protactinium and trans-plutonium actinides are missing or considered as unreliable. The difference between new and old data points increases with the atomic number of the actinide and the oxygen potential [33] of the corresponding dioxide. Data of the room temperature sublimation enthalpy $\Delta H_{sub}(298)$ [34–38] for the actinide dioxide series are also reported for comparison. Similar to the melting/solidification temperature trend, $\Delta H_{sub}(298)$ is much higher for ThO$_2$ than for the other actinide dioxides, signifying a correspondingly larger cohesion energy of thorium dioxide, which has no f-electrons involved in the formation of molecular orbitals.

assessed melting/freezing points of the same compounds. $\Delta H_{sub}(298)$ is in fact known to be much higher for ThO$_2$ than for the other actinide dioxides (Figure 3.7), signifying a correspondingly larger cohesion energy of thorium dioxide, which has no f-electrons involved in the formation of molecular orbitals. This suggests that new experimental data like the current ones might help a better comprehension of the f-electron behaviour in actinide compounds. Moreover, such behaviour parallels the reported melting/freezing points consistently, and encourages further research in this fascinating domain. For example, even the solid/liquid transition temperature of protactinium dioxide can be estimated to be close to the one of UO$_2$ if the current trend is proven to be correct.

3.5. CONCLUSION

T HE melting behaviour of NpO$_2$ has been revisited in this work by means of fast remote laser heating under controlled atmosphere. The following conclusions can be drawn from the present research:

- Neptunium dioxide melts at (3070 ± 62) K, at a composition between NpO$_{1.98}$ and NpO$_{2.00}$.

- Although it is likely that stoichiometric NpO_2 undergoes oxygen losing processes before melting, no clear effect of the external atmosphere on the liquid/solid transition could be observed in the current work, where a composition close to stoichiometric was maintained, thanks to the short material exposure at high temperature.

- Large disagreement (> 200 K) between the current results and earlier experimental data obtained by W-furnace heating shows that the melting behaviour of neptunium dioxide is largely determined by the interaction between this material and its containment, essentially due to the high oxygen potential of NpO_2; a similar behaviour had already been observed for other similar compounds (e.g., CeO_2, PuO_2).

- Phase-field simulations of the current experiments give good insight into the phenomena occurring during the laser heating cycles.

- Comparison between experimental and simulated thermograms reveals that the high-temperature thermal conductivity of NpO_2 likely behaves similarly to UO_2, where the polaron contribution plays an essential role.

- The melting point trend of actinide dioxides as a function of the actinide atomic number Z can be reassessed with the current data: this trend seems to qualitatively resemble that of the sublimation enthalpies for the same compounds. Thanks to correlations of this type, the melting point of so far unmeasured compounds might be estimated.

These encouraging results motivate further research on the very high temperature behaviour of other materials, whose behaviour might result considerably more complex than it could be believed on the basis of traditional furnace heating experiments only.

REFERENCES

[1] R. Böhler, M. J. Welland, F. D. Bruycker, K. Boboridis, A. Janssen, R. Eloirdi, R. J. M. Konings, and D. Manara, *Revisiting the melting temperature of NpO2 and the challenges associated with high temperature actinide compound measurements,* J. Appl. Phys. **111**, 113501 (2012).

[2] C. Rodriguez, A. Baxter, D. McEachern, M. Fikani, and F. Venneri, *Deep-Burn: making nuclear waste transmutation practical,* Nucl. Eng. Des. **222**, 299 (2003).

[3] J. Fuger, H. Nitsche, and R. Lemire, *Chemical Thermodynamics of Neptunium and Plutonium,* in *Chem. Thermodynamics Ser. Vol. 4* (Elsevier, 2001).

[4] T. D. Chikalla, C. E. McNeilly, J. L. Bates, and J. J. Rasmussen, *High-Temperature Phase Transformations in Some Lanthanide and Actinide Oxides,* Tech. Rep. (Battle North-West Laboratory Report - SA 3818, 1971).

[5] K. Richter and C. Sari, *Phase relationships in the neptunium-oxygen system,* J. Nucl. Mater. **148**, 266 (1987).

[6] F. De Bruycker, K. Boboridis, R. Konings, M. Rini, R. Eloirdi, C. Guéneau, N. Dupin, and D. Manara, *On the melting behaviour of uranium/plutonium mixed dioxides with high-Pu content: A laser heating study,* J. Nucl. Mater. **419**, 186 (2011).

[7] C. Utton, F. De Bruycker, K. Boboridis, R. Jardin, H. Noel, C. Guéneau, and D. Manara, *Laser melting of uranium carbides,* J. Nucl. Mater. **385**, 443 (2009).

[8] D. Manara, C. Ronchi, M. Sheindlin, M. Lewis, and M. Brykin, *Melting of stoichiometric and hyperstoichiometric uranium dioxide,* J. Nucl. Mater. **342**, 148 (2005).

[9] C. Guéneau, N. Dupin, B. Sundman, C. Martial, J.-C. Dumas, S. Gossé, S. Chatain, F. D. Bruycker, D. Manara, and R. J. Konings, *Thermodynamic modelling of advanced oxide and carbide nuclear fuels: Description of the U-Pu-O-C systems,* J. Nucl. Mater. **419**, 145 (2011).

[10] S. R. De Groot and P. Mazur, *Non-Equilibrium Thermodynamics* (Dover, 1985).

[11] D. Manara, M. Sheindlin, W. Heinz, and C. Ronchi, *New techniques for high-temperature melting measurements in volatile refractory materials via laser surface heating,* Rev. Sci. Instrum. **79**, 113901 (2008).

[12] H. Preston-Thomas, *The International Temperature Scale of 1990 (ITS-90),* Metrologia **27**, 107 (1990).

[13] R. E. Bedford, G. Bonnier, H. Maas, and F. Pavese, *Recommended values of temperature on the International Temperature Scale of 1990 for a selected set of secondary reference points,* Metrologia **33**, 133 (1996).

[14] A. S. Tenney, *Radiation Ratio Thermometry,* in *Theory Pract. Radiat. Thermom.*, edited by D. P. DeWitt and G. D. Nutter (John Wiley & Sons, Inc., 1988) Chap. 6, pp. 459–494.

[15] M. Bober, J. Singer, and K. Wagner, *Spectral Reflectivity and Emissivity Measurements of Solid and Liquid UO$_2$ at 458, 514.5 and 647 nm as a Function of Polarization and Angle of Incidence*, Tech. Rep. September (Kernforschungszentrum Karlsruhe - Institut für Neutronenphysik und Reaktortechnik, 1980).

[16] M. Welland, W. Thompson, B. Lewis, and D. Manara, *Computer simulations of non-congruent melting of hyperstoichiometric uranium dioxide,* J. Nucl. Mater. **385**, 358 (2009).

[17] P. Papon, J. Leblond, and P. H. Meijer, *The Physics of Phase Transitions* (Springer, 2006).

[18] L. Epstein, *Ideal solution behavior and heats of fusion from the UO$_2$-PuO$_2$ phase diagram,* J. Nucl. Mater. **22**, 340 (1967).

[19] V. Sobolev, *Modelling thermal properties of actinide dioxide fuels,* J. Nucl. Mater. **344**, 198 (2005).

[20] K. Kurosaki, M. Imamura, I. Sato, T. Namekawa, M. Uno, and S. Yamanaka, *Molecular dynamics studies of neptunium dioxide,* J. Alloys Compd. **387**, 9 (2005).

[21] J. Fink, *Thermophysical properties of uranium dioxide,* J. Nucl. Mater. **279**, 1 (2000).

[22] T. Nishi, A. Itoh, M. Takano, M. Numata, M. Akabori, Y. Arai, and K. Minato, *Thermal conductivity of neptunium dioxide,* J. Nucl. Mater. **376**, 78 (2008).

[23] M. Sheindlin, D. Staicu, C. Ronchi, L. Game-Arnaud, B. Remy, and a. Degiovanni, *Experimental determination of the thermal conductivity of liquid UO[sub 2] near the melting point,* J. Appl. Phys. **101**, 093508 (2007).

[24] J. J. Carbajo, G. L. Yoder, S. G. Popov, and V. K. Ivanov, *A review of the thermophysical properties of MOX and UO$_2$ fuels,* J. Nucl. Mater. **299**, 181 (2001).

[25] D. Taylor, , Br. Ceram. Trans. J. **83** (1984).

[26] H. Kinoshita, D. Setoyama, Y. Saito, M. Hirota, K. Kurosaki, M. Uno, and S. Yamanaka, *Thermodynamic modelling and phase stability assessment of MO_{2-x} oxides with a fluorite structure,* J. Chem. Thermodyn. **35**, 719 (2003).

[27] T. Yamada, M. Yoshimura, and S. Somiya, *Reinvestigation of the Solidification Point of CaO by Digital Pyrometry,* J. Am. Ceram. Soc. **69**, C (1986).

[28] M. Zinkevich, D. Djurovic, and F. Aldinger, *Thermodynamic modelling of the cerium-oxygen system,* Solid State Ionics **177**, 989 (2006).

[29] C. Ronchi and J.-P. Hiernaut, *Experimental measurement of pre-melting and melting of thorium dioxide,* J. Alloys Compd. **240**, 179 (1996).

[30] W. A. Lambertson, M. H. Mueller, and F. H. Gunzel, *Uranium Oxide Phase Equilibrium Systems: IV, UO$_2$-ThO$_2$,* J. Am. Ceram. Soc. **36**, 397 (1953).

[31] R. Latta, E. Duderstadt, and R. Fryxell, *Solidus and liquidus temperatures in the UO$_2$-ThO$_2$ system,* J. Nucl. Mater. **35**, 347 (1970).

[32] W. Lyon and W. Baily, *The solid-liquid phase diagram for the UO$_2$-PuO$_2$ system,* J. Nucl. Mater. **22**, 332 (1967).

[33] C. Guéneau, A. Chartier, and L. V. Brutzel, *2.02 - Thermodynamic and Thermophysical Properties of the Actinide Oxides,* in *Compr. Nucl. Mater.*, edited by R. J. Konings (Elsevier, Oxford, 2012) pp. 21–59.

[34] E. Shapiro, *Vapor Pressure of Thorium Oxide from 2050 to 2250 K,* J. Am. Chem. Soc. **74**, 5233 (1952).

[35] P. Kleinschmidt and J. Ward, *Thermochemical studies on the plutonium fluorides and protactinium ovides,* J. Less Common Met. **121**, 61 (1986).

[36] R. W. Ohse, *High-Temperature Vapor-Pressure Studies of UO$_2$ by the Effusion Method and Its Thermodynamic Interpretation,* J. Chem. Phys. **44**, 1375 (1966).

[37] R. J. M. Konings, O. Beneš, A. Kovács, D. Manara, D. Sedmidubský, L. Gorokhov, V. S. Iorish, V. Yungman, E. Shenyavskaya, and E. Osina, *The Thermodynamic Properties of the f-Elements and their Compounds. Part 2. The Lanthanide and Actinide Oxides,* J. Phys. Chem. Ref. Data **43**, 013101 (2014).

[38] R. J. Ackermann, R. L. Faircloth, and M. H. Rand, *A Thermodynamic Study of the Vaporization Behavior of the Substoichiometric Plutonium Dioxide Phase,* J. Phys. Chem. **70**, 3698 (1966).

3

4

APPLICATION OF THE LINDEMANN MELTING RULE TO ACTINIDE DIOXIDES

Robert Böhler, Christos Apostolidis, Dario Manara, Rudy J.M. Konings

Recent laser heating experiments on actinide dioxides have revealed higher melting temperatures for PuO_2 and NpO_2 than previously reported. These results establish a new the trend in melting temperatures in the actinide series from ThO_2 to PuO_2. Since missing melting data for highly radioactive and chemically unstable compounds (PaO_2, AmO_2, CmO_2) are currently experimentally difficult to obtain, a theoretical approach is proposed here to estimate these values. The Lindemann melting rule is applied in combination with force constant values between actinide metal and oxygen so as to correlate the actinide melting temperature to a bond strength. This relation permits to estimate AmO_2 to melt close to 3000 K, and gives first estimations for CmO_2 and PaO_2.

4.1. Melting of pure actinide dioxides

As it has already been stated, the melting temperature is a crucial fundamental characteristic for a material. With the presented melting temperature of NpO_2 in chapter 3, the measurements for all stable actinide dioxides in standard conditions, which were available for such laser melting experiments, were completed. The laser heating experiments confirmed or revealed new melting temperatures for ThO_2 ([1] and chapter 6), UO_2 ([2] and chapter 5), NpO_2 ([3] and chapter 3) and PuO_2 ([4] and chapter 5) as shown in Fig. 3.7. Nevertheless, the actinide dioxide series is still incomplete as a whole.

Chemically, the dioxide form exists among the actinides from thorium up to californium [5]. However, measurements of the melting points become difficult at the end of the series mainly because of the very limited availability of such materials. Besides, material which can be prepared for such melting experiments in sufficient amounts has a high level of radioactivity and toxicity making bulk measurements such as melting temperature determination highly complicated. Hence, the estimation of the melting points of other pure dioxides such as protactinium (PaO_2), americium (AmO_2) or curium (CmO_2) can only be achieved theoretically so far.

Although industrial applications of the higher actinides are very limited, especially at high temperatures, there is interest in studying the properties of these materials. The special status of the actinides with their [Rn]5f electron state has been the subject of numerous studies but is not yet completed. Knowledge of their melting points may contribute more to a general understanding.

4.2. Analogues with the melting temperature

A general relation between melting temperature and other material properties has not yet been reported successfully. Also numerical simulations are missing or still have large uncertainties in determining the melting transition [6, 7]. Finding an empirical correlation between the melting temperature of the different actinides dioxides and another independent parameter seems to be the most promising approach, since an inter- or extrapolation to missing melting temperatures has no physical meaning.

Such empirical relations were suggested before, as for example a constant ratio between the melting temperature and the linear thermal expansion coefficient, which has been tested on pure elements [8] and was unsuccessfully applied to the actinide dioxides [9]. However it is difficult to apply those relations at high temperature, because the parameters are temperature dependent. Moreover, data availability on actinide compounds is comparatively poor. A comparison with available (thermodynamic) data provides only unclear trends (Fig. 4.1). Due to the experimental difficulties many material properties are obtained with different methods and show a relatively large scatter. Also numerical simulation reproduces such scattering [10].

To establish a physically meaningful correlation for the melting point, one still needs a model to describe melting. The method chosen in this study is the correlation found by Lindemann in 1910 [12]. The Lindemann rule states that a material melts when the amplitude of thermal vibration of the atoms in the crystal lattice exceeds a certain fraction of the interatomic distance. It has been used for melting point estimations for many years, but it has no rigorous physical basis. "*The Lindemann rule has powerful intuitive*
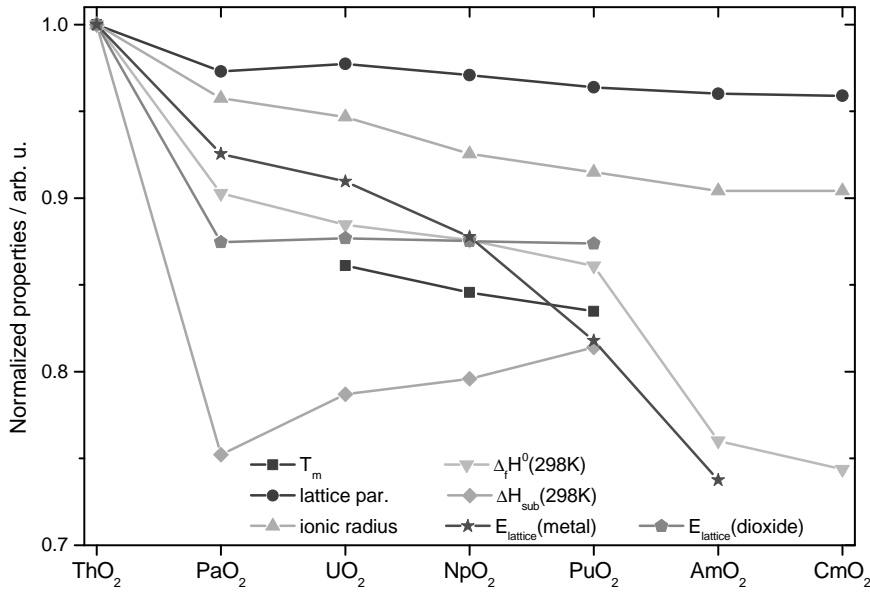
Figure 4.1: Different material properties of some actinide dioxides normalized to their highest value in the series ThO_2-CmO_2. References are for melting temperature: this work; lattice parameter, ionic radius, standard formation enthalpy: [5]; room temperature sublimation enthalpy: see Fig. 3.7; energy of the lattice [11] = formation enthalpy (dioxide/metal) + dissociation energy of oxygen + sublimation enthalpy (metal)

appeal. At high enough temperatures, we can imagine that the crystal must shake itself to pieces."[13] It also does not consider the liquid state as in any thermodynamic model. It has been updated for monoatomic elements [14] and was used in different approaches (e.g.: [8, 15–17]) over the years. Although the success in predicting melting temperatures can be concluded to be limited, it still remains in use on compounds due to the lack of more accurate models.

The Lindemann relation is used in this work in the form [17]:

$$\frac{1}{2}K\Delta x_m^2 = k_B T_m \tag{4.1}$$

$$\frac{1}{2}K(x_{rel} \cdot d_{atom})^2 = k_B T_m \tag{4.2}$$

where K is a force constant for the metal - oxygen stretching in these investigated compounds, Δx_m represents the vibration amplitude of the bond at melting, k_B is the Boltzmann constant and T_m the melting temperature. It is more practical to refer to the relative amplitude, x_{rel}, which is the vibration amplitude, x_m, divided by the interatomic distance, d_{atom}. Hence, the left hand side represents the elastic potential energy of a spring, whereas the right hand side is the thermal energy at melting temperature.

The advantage of this description of the Lindemann rule is that the parameters are not temperature dependent. Force constants for the lattice can be determined at room temperature. The often found equivalent form of Eq. 4.2 using the Debye temperature

[16] is not applicable with the actinide dioxides, since no consistent and comparable dataset is available.

The force constant is obtained from a purely mechanical vibration model of the lattice. The vibration of the molecules can be linked to optical (IR or Raman) active vibrations which can be measured by spectroscopic methods [18]. The metal - oxygen stretching is then completely dependent on the T_{1u} vibration mode, C_{vib}, which is in CaF_2-type fcc crystals infrared (IR) active, and the reciprocal masses, μ, of the atoms.

$$C_{vib}^{IR} \propto \frac{4}{3} K(\mu_{oxygen} + 2\mu_{metal}) \, . \tag{4.3}$$

The vibrations of the oxygen bonds, with the force constant F, in the CaF_2-type lattice can be obtained with the Raman active T_{2g} vibration mode with the model of Shimanoushi [18]

$$C_{vib}^{Raman} \propto \frac{4}{3} (K + 3F)\mu_{oxygen} \, . \tag{4.4}$$

With $C_{vib} = \pi^2 \cdot c^2 \cdot v^2$ the force constants can be directly calculated from the measurement results of the vibration wavenumber, v and the speed of light, c.

Hence, knowing the melting temperatures of several actinide dioxides and the force constants from IR measurements, one can already extra- and interpolate to other dioxides assuming similar melting behaviour.

The vibrations of the oxygen atoms in the CaF_2-type lattice are presumed to maximise in a order-disorder lambda transition (Bredig transition) before the actual melting point of the whole material (as suggested for ThO_2 or UO_2[1, 19]). For the application and use of such a lambda transition with the Lindemann rule, one would need first confirmed data for the transition temperature before an estimation for other values can be done.

4.3. APPLICATION OF THE LINDEMANN RULE

MELTING is defined in the Lindemann expression as the point beyond the bonds are stretched so that the lattice loses its structure. Usually, this stretching reaches up to around 15% of the normal interatomic distances for several materials [13]. For CaF_2, the calculated elongation at melting is about 17.2% (with K = 0.284 mdyne [20], T_m = 1696 K and a bond distance of 2.365 Å). This stretching is here assumed to be similar for the actinide dioxides with the same lattice type.

For the inter- or extrapolation with Eq. 4.2 to actinide dioxides with unknown melting temperatures, one can choose to use the amplitude or the force constant as a reference value. Tab. 4.1 lists the other input parameters for the Lindemann equation which are known for the actinide dioxides. The force constants can be taken from other work to calculate the vibration amplitudes.

Tab. 4.2 and Fig. 4.2 show the values measured at ITU for pure dioxides and estimated values for AmO_2. No trend is visible for the measured force constants K from ThO_2 to PuO_2, which make an interpolation to PaO_2 not obvious. The relative amplitude seems to decrease over the series, with an exceptional small increase for NpO_2. An estimation for AmO_2 was therefore made by extrapolating the decreasing tendency for

Material	Melting temperature	Interatomic distance (An-O)
ThO_2	3624 K	2.424 Å
PaO_2	-	2.358 Å
UO_2	3126 K	2.369 Å
NpO_2	3070 K	2.353 Å
PuO_2	3050 K	2.336 Å
AmO_2	-	2.327 Å
CmO_2	-	2.325 Å

Table 4.1: Known material properties used here in the Lindemann rule. The interatomic distances were taken from [21]; the melting temperatures are from this work.

Compound	K / mdyne/Å	Rel. amplitude	Melting temperature / K
ThO_2	0.4701	0.1903	3624
PaO_2	-	-	-
UO_2	0.4750	0.1799	3126
NpO_2	0.4696	0.1808	3070
PuO_2	0.5068	0.1745	3050
AmO_2	(*0.51*)	(*0.173*)	(*3000*)

Table 4.2: Force constants from IR - measurements performed at the ITU. Estimated values for AmO_2 are in brackets.
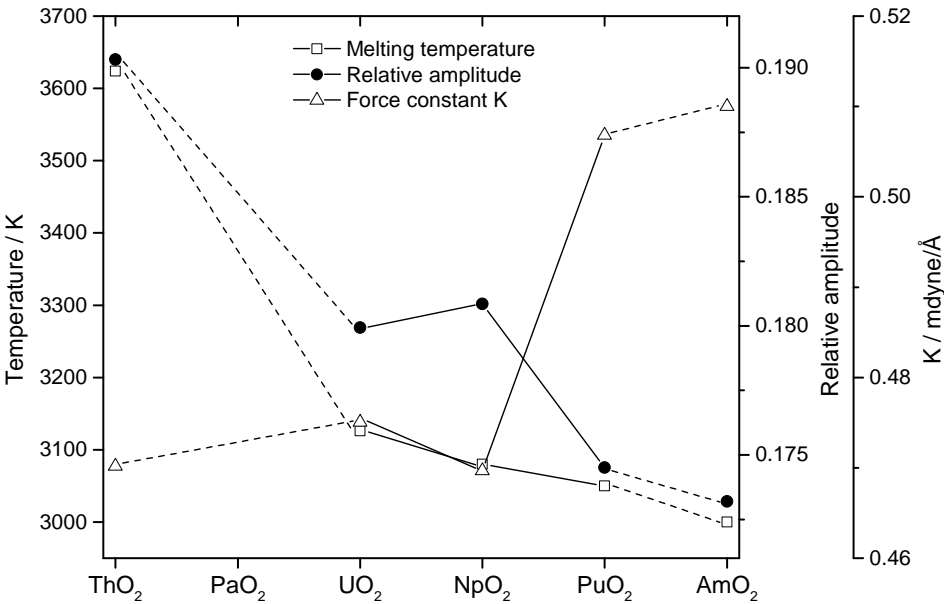

Figure 4.2: Calculated values from ITU measurements with an extrapolation to AmO_2.

Compound	K / mdyne/Å	Rel. Amplitude	Melting temperature / K
ThO_2	0.497	0.1851	3624
PaO_2	0.456	(*0.18*)	(*3043*)
UO_2	0.5	0.1753	3126
NpO_2	0.52	0.1716	3070
PuO_2	0.57	0.1646	3050
AmO_2	0.596	(*0.16*)	(*2992*)
CmO_2	0.518	(*0.155*)	(*2434*)

Table 4.3: Force constants on the basis of Begun et al. [22]. Estimated and calculated values are in brackets.
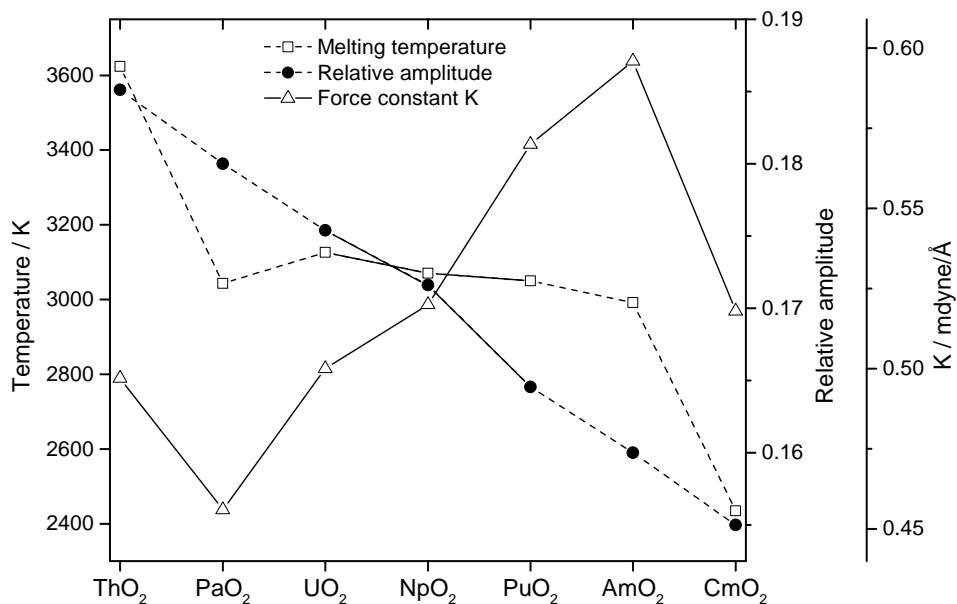
Figure 4.3: Calculated values on the basis of Begun et al. [22]. Values for PaO_2, AmO_2 and CmO_2 were obtained assuming a linear trend in the relative amplitude of the vibration of the metal - oxygen bond.

the relative amplitude and a slightly increasing force constant compared to the other actinide dioxides. This results in a melting temperature of about 3000 K. Nevertheless, the extrapolation chosen for the ITU data has to considered with caution since no rigorous physical basis is considered. By changing the assumed extrapolation slopes for the ITU dataset to more extreme values (0.48 mdyne < K < 0.54 mdyne; $0.160 < x_{rel} < 0.185$), the melting temperatures of AmO_2 may vary by several hundred degrees (2400 K < T_m < 3200 K).

Begun et al. [22] summarized several IR, Raman frequencies and force constants for some actinide dioxides and other iso-structural compounds. The results on actinide dioxides are shown in Tab. 4.3 and Fig. 4.3. Since force constants for all materials were given, only the relative intensity and the melting temperature are left as parameter for Eq. 4.2.

The calculated relative amplitudes from the data of Begun et al. seem to justify a linear trend for the relative amplitude. Following this trend for an interpolation and extrapolation to other dioxides, temperature estimations for PaO_2 (3043 K), AmO_2 (2992 K) and CmO_2 (2434 K) are possible. The value for AmO_2 supports the former assumption for the ITU data set of an increasing force constant and a decreasing relative vibration amplitude. A change in the assumed relative amplitudes ($0.155 < x_{rel} < 0.165$) would change the melting temperature of AmO_2 to $2800 K < T_m < 3180 K$. CmO_2 would follow this extremes accordingly.

More data on ThO_2 and UO_2 is available from Keramidas [20] for the force constant K. These are nearly identical to the data of Begun et al. and therefore do not provide other possibilities for extrapolation without assuming two parameters (K and rel. amplitude) at the same time for other actinide dioxides.

4.4. REVIEW OF THE RESULTS

THE correlation of Lindemann's rule and the force constant makes it possible to obtain the data in a consistent way - here by vibrational spectroscopy. This is often not the case for other (thermal) material properties. Other correlations (Fig. 4.1) or estimations of cohesion energies were not possible to relate to the measured melting points and rarely give a clear trend (e.g. [11, 23]).

The scatter in the measurements and calculation of the force constants and melting temperature can be correlated to the difficulties associated with IR measurements. This deviation relies on the determination of the T_{1u} vibration, which is very low in intensity [24]. Any further calculation of properties such as the Grüneisen parameter or the Debye temperature were not attempted because of the relatively large uncertainty in the current data.

The estimated temperature for AmO_2 fits well in the trend of a decreasing temperature of the actinide dioxides. However it is of theoretical relevance, since the value of about 3000 K is about 2000 K higher than the estimated decomposition temperature and about 1200 K higher than the most stable hypostiometric dioxide [25]. CmO_2 can only be rated to have a lower melting temperature. But consistent data collected by Begun et al. allowed an interpolation to PaO_2 (3043 K).

The assumption of the linear trend of the relative amplitude of the T_{1u} vibration along the actinide dioxide series has so far no rigorous physical background or base. Nevertheless one can assume a stronger cohesion of ThO_2 compared to other actinide dioxides due to the higher melting temperature. This would also justify a higher relative amplitude at melting and a decreasing trend along the series. Also, oxygen potential data for the actinide dioxides reveal a decreasing chemical stability of the dioxides from thorium onwards in the actinide series [5].

On the other hand, the trend of the force constant K is increasing along the series. This means that the bonding between the metal and the oxygen is the stiffer the higher the actinide atomic number z. This seems contradictory to the trends of melting temperatures and presumed cohesion. Moreover it raises the question if the force constant can be related to the chemical stability and cohesion.

Direct conclusions from melting temperatures to the bonding / cohesion energy in the actinide dioxides seem to be very difficult, especially since the electronic structure

of the 5f-dioxides is not yet fully resolved. Conclusions from the electronic structure are therefore also still very uncertain. Effects seen as orbital mixing between the 5f metal electrons and the 2p oxygen electrons starting from PuO_2, presented in a DFT study of the whole actinide dioxide series [26], have to be considered to determine the influence on the cohesion energy and the link to the melting temperature.

REFERENCES

[1] C. Ronchi and J.-P. Hiernaut, *Experimental measurement of pre-melting and melting of thorium dioxide,* J. Alloys Compd. **240**, 179 (1996).

[2] D. Manara, C. Ronchi, M. Sheindlin, M. Lewis, and M. Brykin, *Melting of stoichiometric and hyperstoichiometric uranium dioxide,* J. Nucl. Mater. **342**, 148 (2005).

[3] R. Böhler, M. J. Welland, F. D. Bruycker, K. Boboridis, A. Janssen, R. Eloirdi, R. J. M. Konings, and D. Manara, *Revisiting the melting temperature of NpO_2 and the challenges associated with high temperature actinide compound measurements,* J. Appl. Phys. **111**, 113501 (2012).

[4] F. De Bruycker, K. Boboridis, R. Konings, M. Rini, R. Eloirdi, C. Guéneau, N. Dupin, and D. Manara, *On the melting behaviour of uranium/plutonium mixed dioxides with high-Pu content: A laser heating study,* J. Nucl. Mater. **419**, 186 (2011).

[5] C. Guéneau, A. Chartier, and L. V. Brutzel, *2.02 - Thermodynamic and Thermophysical Properties of the Actinide Oxides,* in *Compr. Nucl. Mater.*, edited by R. J. Konings (Elsevier, Oxford, 2012) pp. 21–59.

[6] T. Arima, K. Idemitsu, Y. Inagaki, Y. Tsujita, M. Kinoshita, and E. Yakub, *Evaluation of melting point of UO2 by molecular dynamics simulation,* J. Nucl. Mater. **389**, 149 (2009).

[7] Y. Zhang and E. J. Maginn, *A comparison of methods for melting point calculation using molecular dynamics simulations.* J. Chem. Phys. **136**, 144116 (2012).

[8] A. V. Granato, D. M. Joncich, and V. A. Khonik, *Melting, thermal expansion, and the Lindemann rule for elemental substances,* Appl. Phys. Lett. **97**, 171911 (2010).

[9] T. Yamashita, N. Nitani, T. Tsuji, and H. Inagaki, *Thermal expansions of NpO_2 and some other actinide dioxides,* J. Nucl. Mater. **245**, 72 (1997).

[10] K. Kurosaki, M. Imamura, I. Sato, T. Namekawa, M. Uno, and S. Yamanaka, *Molecular Dynamics Studies of Minor Actinide Dioxides,* J. Nucl. Sci. Technol. **41**, 827 (2004).

[11] P. J. Kelly and M. S. S. Brooks, *Electronic structure and ground-state properties of the actinide dioxides,* J. Chem. Soc. Faraday Trans. 2 **83**, 1189 (1987).

[12] F. A. Lindemann, *The calculation of molecular vibration frequencies,* Phys. Z. **11**, 609 (1910).

[13] A. Lawson, *Physics of the Lindemann melting rule,* Philos. Mag. **89**, 1757 (2009).

[14] J. Gilvarry, *The Lindemann and Grüneisen Laws,* Phys. Rev. **102**, 308 (1956).

[15] D. Berrebi, L. Gregorian, S. Rabinovich, E. Shasha, and A. Voronel, *Classification of phase diagrams for alkali halide mixtures and the generalized Lindemann criterion,* J. Phys. Condens. Matter **4**, 10139 (1992).

[16] G. H. Wolf and R. Jeanloz, *Lindemann Melting Law: Anharmonic correction and test of its validity for minerals,* J. Geophys. Res. **89**, 7821 (1984).

[17] A. C. Lawson, B. M. Artinez, J. a. Roberts, B. I. Bennett, and J. W. Richardson, *Melting of the light actinides,* Philos. Mag. Part B **80**, 53 (2000).

[18] T. Shimanouchi, M. Tsuboi, and T. Miyazawa, *Optically Active Lattice Vibrations as Treated by the GF-Matrix Method,* J. Chem. Phys. **35**, 1597 (1961).

[19] C. Ronchi and G. Hyland, *Analysis of recent measurements of the heat capacity of uranium dioxide,* J. Alloys Compd. **213-214**, 159 (1994).

[20] V. G. Keramidas, *Raman spectra of oxides with the fluorite structure,* J. Chem. Phys. **59**, 1561 (1973).

[21] L. R. Morss, N. M. Edelstein, and J. Fuger, eds., *The Chemistry of the Actinide and Transactinide Elements* (Springer Netherlands, 2011).

[22] G. Begun, R. Haire, W. Wilmarth, and J. Peterson, *Raman spectra of some actinide dioxides and of EuF_2,* J. Less Common Met. **162**, 129 (1990).

[23] P. J. Kelly and M. S. S. Brooks, *Cohesive properties of CaF_2 and UO_2 in the atomic sphere approximation,* J. Phys. C Solid State Phys. **13**, L939 (1980).

[24] J. Axe and G. Pettit, *Infrared Dielectric Dispersion and Lattice Dynamics of Uranium Dioxide and Thorium Dioxide,* Phys. Rev. **151**, 676 (1966).

[25] P. Gotcu-Freis, J.-Y. Colle, C. Guéneau, N. Dupin, B. Sundman, and R. Konings, *A thermodynamic study of the Pu-Am-O system,* J. Nucl. Mater. **414**, 408 (2011).

[26] I. Prodan, G. Scuseria, and R. Martin, *Covalency in the actinide dioxides: Systematic study of the electronic properties using screened hybrid density functional theory,* Phys. Rev. B **76**, 033101 (2007).

4

5

REVISITING THE MELTING TEMPERATURE OF UO$_2$-PUO$_2$

Robert BÖHLER, Micheal J. WELLAND, Damien PRIEUR, Pelin ÇAKIR, Tonya VITOVA, Ivan PIDCHENKO, Tim PRÜSSMANN, Christoph HENNING, Christine GUÉNEAU, Rudy J.M. KONINGS, Dario MANARA

Recently, novel container-less laser heating experimental data have been published on the melting behaviour of pure PuO$_2$ and PuO$_2$-rich compositions in the uranium dioxide - plutonium dioxide system. It is therefore paramount to check whether data so far used by nuclear engineers for the uranium-rich side of the pseudo - binary dioxide system can be confirmed or not. In the present work, new data are presented both in the UO2-rich part of the phase diagram, most interesting for the uranium - plutonium dioxide based nuclear fuel safety, and in the PuO$_2$ side. The new results confirm earlier furnace heating data in the uranium - dioxide rich part of the phase diagram, and more recent laser-heating data in the plutonium - dioxide side of the system. As a consequence, it is also confirmed that a minimum melting point must exist in the UO$_2$ - PuO$_2$ system, at a composition between x(PuO$_2$) = 0.4 and x(PuO$_2$) = 0.7 and 2900 K ≤ T ≤ 3000 K. Taking into account that, especially at high temperature, oxygen chemistry has an effect on the reported phase boundary uncertainties, the current results should be projected in the ternary U - Pu - O system. This aspect has been extensively studied here by X-ray diffraction and X-ray absorption spectroscopy. The current results suggest that uncertainty bands related to oxygen behaviour in the equilibria between condensed phases and gas should not significantly affect the qualitative trend of the current solid - liquid phase boundaries.

5.1. INTRODUCTION

HIGH temperature phase relationships (and particularly the melting behaviour) in the ternary U-Pu-O system have been thoroughly re-assessed in the last few years with the help of the CALPHAD thermodynamic optimisation approach taking into account the novel experimental data obtained at JRC-ITU by fast laser heating under quasi-containerless conditions and controlled atmosphere [2]. Some of these data displayed a considerable disagreement with respect to the existing literature, such as the melting behaviour of hyper-stoichiometric UO_{2+x} [3], pure PuO_2 [4], and Pu-rich UO_2-PuO_2 mixed oxides [5, 6]. Data reported in earlier literature were obtained by "'traditional"' furnace heating a dissertation is a substantial document in a tungsten [7, 8] (or, sometimes, rhenium [8, 9]) crucible. The large differences with respect to the new JRC-ITU data have been explained on the basis of the elevated oxygen potential [10–13]:

$$\Delta G_{O_2}^{AnO_2} = \bar{\mu}_{O_2}^{AnO_2} = RT \ln a_{O_2}^{AnO_2} . \tag{5.1}$$

In Eq. 5.1, $\bar{\mu}_{O_2}^{AnO_2}$ is the oxygen chemical potential in a generic actinide dioxide (AnO_2), defined as the partial molar Gibbs free energy difference (ΔG_{O_2}) between a molecule of oxygen in its free (gaseous) state and the same oxygen in the dioxide AnO_2. R is the ideal gas constant, T the absolute temperature, and $a_{O_2}^{AnO_2}$ the oxygen activity in the dioxide AnO_2. This latter is defined as the product of the oxygen partial pressure (expressed in atm) by an activity coefficient (generally very close to 1) taking into account non-ideal interactions [12]. A high oxygen potential leads to an oxygen-driven high reactivity of the investigated compounds towards the metallic containment. This would affect most of the furnace results for the very high temperature behaviour of compounds displaying a high $\bar{\mu}_{O_2}$. For example, this assumption is confirmed by the fact that melting/freezing points of actinide oxides obtained by the quasi- containerless laser heating approach agree less with furnace results, the higher the oxygen potential of the investigated compound (Fig. 5.1). For compounds with low oxygen potential (such as ThO_2 and stoichiometric UO_2), the agreement is good.

The $(U, Pu)O_2$ pseudo-binary section of the ternary U-Pu-O system is most interesting for nuclear applications, as mixed uraniumplutonium dioxides (MOX) constitute the main components of the nuclear fuel in many of the currently operational plants. In mixed oxides, it can be assumed that the oxygen potential evolves linearly from one to the other end member, e.g.:

$$\bar{\mu}_{O_2}^{MOX} = x(UO_2) \cdot \bar{\mu}_{O_2}^{UO_2} + x(PuO_2) \cdot \bar{\mu}_{O_2}^{PuO_2} . \tag{5.2}$$

Eq. 5.2 uses the same notation as Eq. 5.1), $x(AnO_2)$ representing the molar fraction of the compound AnO_2 (here An = U, Pu, and x(UO_2) + x(PuO_2) = 1). It can then be expected that the melting behaviour observed by quasi-containerless laser heating of mixed oxides richer in a high-$\bar{\mu}_{O_2}$ end member (PuO_2 in the $(U, Pu)O_2$ system) differs from that observed by traditional furnace heating, whereas a better agreement should be expected for the compositions richer in the low-$\bar{\mu}_{O_2}$ end member (UO_2 in the MOX case).

The present paper reports the main results of an experimental investigation performed at JRC-ITU by laser heating on the whole UO_2-PuO_2 system, in order to check
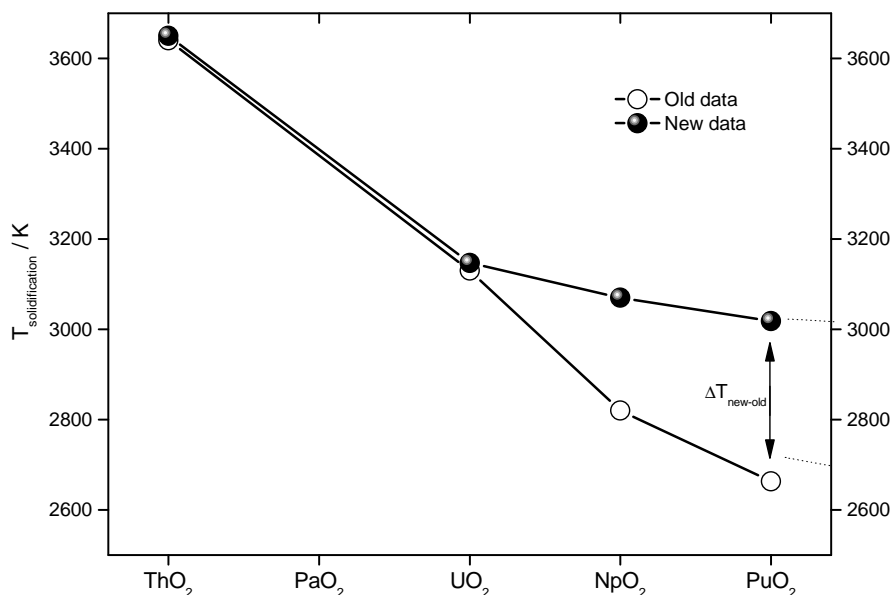
Figure 5.1: The melting/solidification data measured by fast quasi-containerless laser heating in the actinide dioxide series compared with previous furnace heating data [9].

the validity of the above reasoning. Particular attention has been devoted to compositions with $0 \leq x(PuO2) \leq 0.5$, the range of interest for the uranium-plutonium dioxide based nuclear fuel currently used in most reactors.

The main concrete application of this work consists of checking whether data so far used by nuclear engineers for the uranium-rich side of the pseudo-binary dioxide system can be confirmed, since the melting behaviour of pure PuO_2 and PuO_2-rich compositions has been re-assessed in the last few years.

Possible segregation effects during fast heating and cooling across the melting transition have been studied on the whole UO_2-PuO_2 range with the help of powder X-ray diffraction (XRD), Raman spectroscopy (RS), X-ray absorption near-edge spectroscopy (XANES) and high-energy resolution XANES (HR-XANES). In addition, Phase Field modelling of the current laser heating experiments has helped the interpretation of the empirical thermograms.

5.2. EXPERIMENTAL AND MODELLING APPROACH

5.2.1. SAMPLE PREPARATION

A series of mixed $(U, Pu)O_2$ samples with plutonium dioxide molar fraction $x(PuO_2) =$ 0.037, 0.09, 0.25, 0.40, 0.50, 0.80, 0.90 were prepared, calcinated, sintered and annealed according to the procedure reported in [5]. The different samples were designated with the label MOX and the amount-of-substance fraction $x(PuO_2) \cdot 100$. For example, MOX 9 signifies a MOX sample with $x(PuO_2) = 0.09$. Depleted uranium with an average mass fraction $w(235U) = 0.9962\%$ was used for the sample fabrication, starting from dioxide

powders or from a uranyl nitrate solution. The isotopic composition of the plutonium in the starting plutoniumdioxide powders, determined by thermal ionisation mass spectrometry, was found to be w(239Pu) = 0.9354 and w(240Pu) = 0.0632, the remainder being 238Pu, 241Pu, 242Pu and 241Am isotopes, with mass fractions less than 0.01 each.

5.2.2. LASER HEATING AND FAST PYROMETRY SETUP

Details of the laser-heating setup used in this research have been reported in previous publications [2–5], although the technique has been partially improved in the present work.

Thermograms were measured by sub - millisecond resolution pyrometry on MOX samples laser heated beyond melting by a TRUMPF® Nd:YAG cw laser radiating at 1064.5 nm. Its power vs. time profile is programmable with a resolution of 1 ms. Pulses of different duration (100 - 1000 ms) and maximal power (180 - 675 W) were repeated on a 5 mm diameter spot on a single sample surface as well as on different samples of the same composition in order to obtain statistically significant datasets for each composition.

During the shots, the investigated MOX specimen was held in a sealed autoclave under controlled atmosphere. The atmosphere was chosen on the basis of thermodynamic equilibrium calculations between the condensed phases and the vapour [5], in order to maintain as much as possible the original composition of each sample throughout the heating/cooling cycles. Thus UO_2-rich samples were heated under an inert atmosphere (slightly pressurised argon at 0.3 MPa), whereas PuO_2-rich ones were preferably studied under dry compressed air (also at 0.3 MPa), in order to minimise oxygen losses from the condensed phases.

Excessive thermal shocks were minimised by starting each series of laser pulses from a pre-set temperature of about 1500 K. Each series consisted of three heatingcooling pulses on the same sample spot without cooling the material below an intermediate temperature of approximately 1500 K. The peak intensity and duration of the high-power pulses were increased from one heatingcooling cycle to the other, in order to check the result repeatability under slightly different experimental conditions (Fig. 5.2). This approach constituted a step forward in the laser heating technique. It ensured a better mechanical stability of the samples, on which several successive shots could be repeated to check the result reproducibility and the eventual effects of non-congruent vaporisation or segregation phenomena. The onset of melting was detected by the appearance of vibrations in the signal of a probe laser (Ar^+ cw 750 mW to 1.5 W) reflected by the sample surface (reflected Light Signal technique, or RLS) [2]. The sample cooled naturally when the laser beam was switched off during the thermal cycle. Thermal arrests corresponding to solidification were then observed on the thermograms recorded by the fast pyrometers. These operate in the visible-near infrared range between 488 nm and 900 nm. The reference pyrometer wavelength was here 655 nm. This was calibrated according to the procedure already re- ported elsewhere [2–5]. The normal spectral emissivities of urania and plutonia have both been assumed to be equal to 0.83 as deter- mined from previous work employing the same multi-wavelength pyrometry approach [3, 4].

Uncertainty of the measurements was calculated according to the error propagation law [2], taking into account the uncertainty associated to pyrometer calibration, the emissivity, transmittance of the optical system and the accuracy in detecting the on-

set of vibrations in the RLS signal. The estimated cumulative uncertainty is thus lower than ± 2% of the reported temperatures in the worst cases, with a 2-k coverage factor (corresponding to two standard deviation around the average value).

5.2.3. PRE- AND POST-MELTING MATERIAL CHARACTERISATION

Detailed characterisation of the material composition and structure and its evolution after laser heating/melting has been an essential part of this work. The main techniques employed to this goal are: PXRD, Raman spectroscopy and XANES.

POWDER X-RAY DIFFRACTION

PXRD analyses were performed with a Bruker[®] D8 Advance diffractometer (Cu-$K_{\alpha 1}$ radiation) with a 2Θ range of 10 - 120 ° using 0.009° steps with 2 s of integration time per step at operating conditions of 40 kV and 40 mA. Rietveld analysis of the recorded XRD patterns was performed with the help of the FullProf[®] software.

RAMAN SPECTROSCOPY

Raman spectra were measured with a JobinYvon[®] T64000 spectrometer used in the single spectrograph configuration. Used excitation sources were the 488 nm and 514 nm lines of an Ar+ Coherent[®] laser, as well as the 647 nm and the 752 nm lines of a Kr+ Coherent[®] laser. Eventual polarisation effects on the Raman spectra were neglected in the present investigation. Actual wavelength and power were chosen at each measurement in order to optimise the signal/noise ratio (by minimising the material fluorescence) and reducing undesirable oxidation/burning effects on the sample surface.

Moreover, the comparison of Raman spectra measured at different wavelengths permitted the identification of the vibrational or electronic origin of the peaks observed. Spectra were measured in a confocal microscope with a 50-fold magnification and long focal distance. This feature yielded a good spectral resolution (± 1 cm^{-1}) independently of the surface roughness, with a spatial resolution of 2 μm× 2 μm. The spectrometer detector angle was calibrated daily with the T_{2g} excitation of a silicon single crystal, set at 520.5 cm^{-1} [14].

XANES

XANES and HR-XANES [15] measurements have been performed on approximately 4 mg of powdered sample mixed with 55 mg of boron nitride (BN). The data have been collected at the INE-Beamline, Angströmquelle Karlsruhe (ANKA) synchrotron radiation facility in Karlsruhe (Germany) [16] and at the ROBL-Beamline of the European Synchrotron Radiation Facility (ESRF) situated in Grenoble (France) [17].

MOX9 and MOX25 have been measured at the INE beamline with a Ge (422) double-crystal monochromator coupled to collimating and focusing Rh-coated mirrors. XANES spectra were collected at room temperature in transmission mode at the U L_{III} and at the Pu L_{III} edges.

U L_{III}-edge HR-XANES spectra of MOX9 were measured with a multi-analyser crystals Johann type spectrometer (MAC-spectrometer). Fluorescence emitted from U references and MOX9 and MOX9m samples was diffracted by the 5 Ge(777) analyser crystals and focused on a SDD VORTEX. Sample, crystals and detector were positioned on a

Rowland circle in the vertical plane with diameter of 1 m equal to the bending radius of the spherically bent analyser crystals. The MAC-Spectrometer was set at the maximum of the U Lα_1 emission line (13614 eV, 77.4° Bragg angle), whereas the incident energy was scanned to obtain U L$_{III}$ edge (17166 eV) HR-XANES spectra. It was not possible to measure the experimental energy resolution at this photon energy due to the low elastic scattering cross section.

MOX3, MOX40 and MOX50 spectra were collected at ROBL using a double crystal monochromator mounted with Si (111) crystal coupled to collimating and focusing Rh coated mirrors. A 13-element Ge solid-state detector using a XIA (X-ray Instrumentation Associates) digital amplifier was used to acquire the fluorescence signal of the MOX3 at the Pu L$_{III}$ edge. The experimental XANES data were fitted within -20 eV and +30 eV compared to the E$_0$ position.

The energy calibration was accomplished by measuring simultaneously the K edge XANES spectra of a Y (17038 eV) and a Zr (17998 eV) foil for U L$_{III}$ and Pu L$_{III}$, respectively. ATHENA software was used to remove the background and normalize the spectra [18]. The XANES spectra were compared with spectra of UO$_{2.00}$, U$_4^{IV/V}$O$_9$, U$_3^{V/VI}$O$_8$, PuO$_2$ and PuO$_{2+x}$ reference compounds. The absorption edge (E$_0$) values were defined as the first inflexion point of the XANES spectra and set to the energy position of the first node of the second derivative. The energy position EWL of the most intense absorption resonance (white-line, WL) maximum was found by determining the energy position of the first node of the first derivative. During both experimental runs at ANKA and at ESRF, XANES spectra of UO$_2$, U$_4^{IV/V}$O$_9$, U$_3^{V/VI}$O$_8$, PuO$_2$ and Pu$^{III/IV}$O$_{2+x}$ reference materials were collected. For the uranium references, commercial UO$_2$ was employed, whereas U$_4$O$_9$ and U$_3$O$_8$ were obtained by controlled oxidation in air at varying temperature and cross-checked by XRD. The PuO$_2$ reference sample was heat treated in an oxygen flux at 1400 K for 8 h in order to ensure a composition as close as possible to the O/Pu = 2.00 stoichiometry. The stoichiometry of the PuO$_{2+x}$ reference, annealed in Ar + 6% H$_2$ for 8 h at 1900 K, was checked by Thermo-Gravimetric Analysis [5] and XRD measurements, yielding a O/Pu molar ratio of 1.88 ± 0.07. This large uncertainty affecting the hypo-stoichiometric plutonium dioxide reference composition constituted one of the most limiting error sources in the current XANES analysis. The differences between the white line energy positions of these five compounds are in fair agreement with previous work [19–24]. Despite the use of similar Y and Zr calibration foils, a slight shift was observed between the UO$_2$, and PuO$_2$ white line energy positions collected at ESRF and at ANKA (see Table 5.3). However, as similar relative shifts were observed between the reference materials for both beam lines, a qualitative comparison of the data remains possible.

5.2.4. PHASE-FIELD MODELLING

The sometimes complex features of the observed thermal arrests can be attributed to the dynamics of the melting/solidification process of the small liquid pool formed in the solid matrix. Such dynamics have been studied with the help of numerical simulations of the current experiments, based on a Phase-Field approach to the heat and mass diffusion across the phase boundaries.

This model determines the thermal transport coupled with phase stability through a Phase-Field parameter which tightly links the process kinetics to equilibrium thermody-

namic treatments of the material. Such a parameter is identified by a scalar state variable u representing the fraction of the stable phase at each physical point of the system (e.g. $\varphi = 1$ for the liquid, $\varphi = 0$ for the solid, $\varphi \in (0,1)$ for a coexistence of the two). This approach permits a versatile description of the system including representation of phase boundaries with diffuse interfaces, whereas its main drawback is large computational expense, resulting in long calculation times. The models mathematical and numerical details have already been described elsewhere [25, 26]. They have been implemented in the finite element method software COMSOL Multiphysics®.

Many of the material parameters required as input for the model are unknown, especially at the very high temperatures encountered at the liquid state. Missing parameters were therefore extrapolated from lower temperatures or taken from databases of pure UO_2 [3, 27] when no other information was available. A first approximation of the enthalpy of fusion for Pu-rich compositions was calculated using Richards law [28, 29] as a first approximation.

5.3. RESULTS
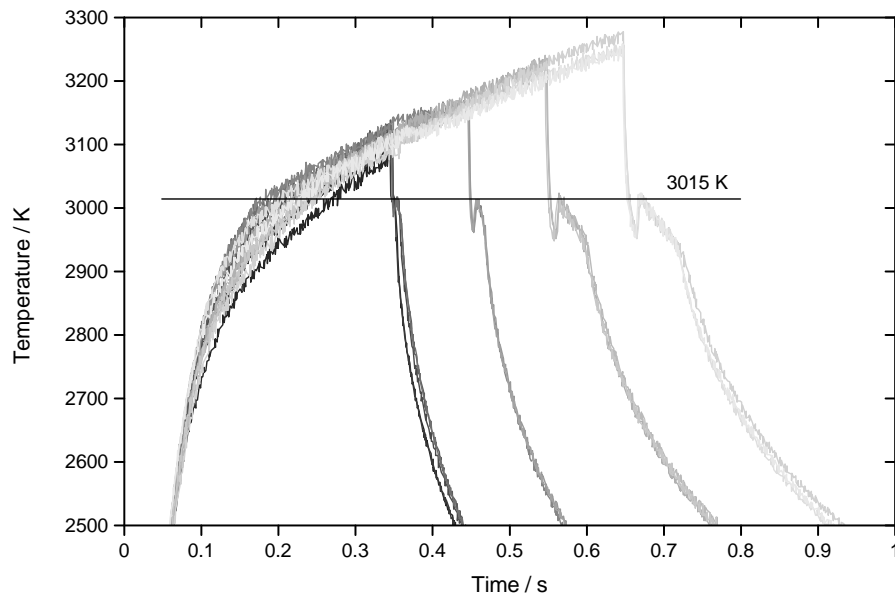
Figure 5.2: Experimental thermograms recorded on a single MOX25 ($U_{0.75}Pu_{0.25}O_2$) sample over successive laser heating cycles. In each cycle, the sample surface was hit by three high-power laser pulses (starting at 0 s) separated by dwelling periods of several seconds during which it was kept at an intermediate temperature around 1500 K in order to minimise thermal shocks. The solidification temperature at 3015 K is suggested by the horizontal line.

FIGURE 5.2 shows, as an example, the heating/cooling cycles performed on a MOX25 specimen. Three high-power pulses were performed in each cycle, separated by longer dwelling periods at an intermediate temperature, around 1500 K. As explained

above, the duration of the high-power pulses was increased from one cycle to the other. The corresponding thermograms changed accordingly. In Fig. 5.2, the three thermograms recorded in each heating/cooling cycle overlap. As already extensively explained in previous work [2–5], a melting inflection is seldom and hardly visible on the thermograms under the current experimental conditions, due to the strongly out - of - equilibrium surface heating produced by the intense laser beam. The melting temperature could only be estimated during heating thanks to the appearance of vibrations in the RLS. Instead, clear thermal arrests / inflections are detectable in the cooling stage of each thermogram overcoming the melting temperature.

One can notice that: (1) Thermograms belonging to the same cycle are generally very well reproducible; the slight change in the heating rate mostly observed in the first cycle can be attributed to the formation and gradual stabilisation and healing of internal cracks in the material, affecting its thermal conduction; (2) Independently of the different thermogram features, the melting/freezing temperatures observed with the help of RLS and thermal arrests remain the same from a cycle to the other, within the experimental uncertainty.

These remarks are paramount because they show that: (1) The current experimental approach preserves the samples mechanical stability over numerous heating-cooling cycles beyond melting; (2) Potential segregation effects, linked to non-congruent melting and vaporisation, have no detectable influence on the reproducibility of the current phase transition temperatures.
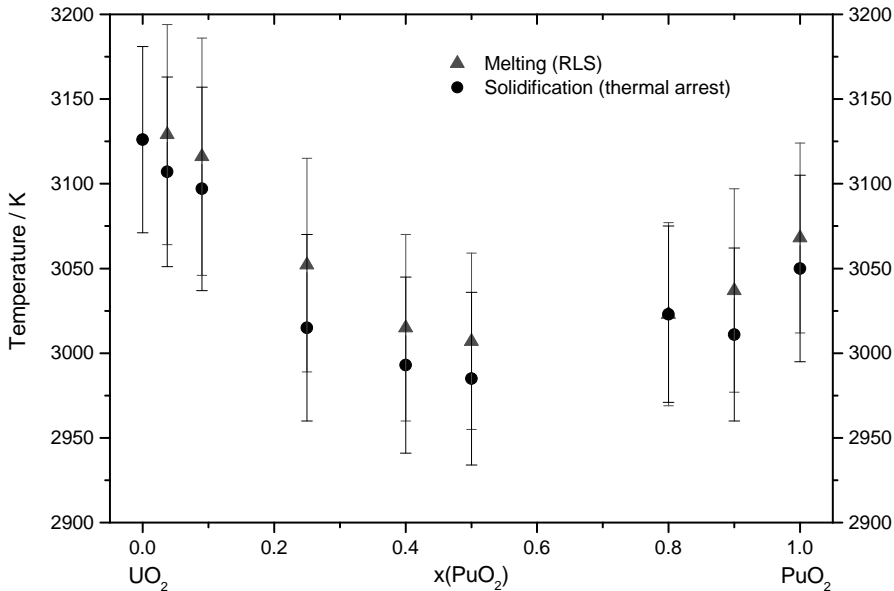

Figure 5.3: The melting/solidification temperatures observed in the present work by RLS and thermal arrest analyses on different MOX samples. Vertical uncertainty bands combine the intrinsic instrumental uncertainty (pyrometer calibration, sample emissivity, transmittance of the optical system) with the experimental data spread.

Fig. 5.3 displays a clear evolution of the melting onset/solidification arrest temperature with composition. Such solidification arrest occurs at lowest temperatures the interval $0.4 < x(PuO2) < 0.7$.

The melting of both pure UO_2 and PuO_2 has been re-investigated with the current approach, too, yielding (3126 ± 55) K and (3050 ± 59) K, respectively. Both values agree, within the reported uncertainties, with those established in the recent literature [3, 4]. The uncertainties reported here are larger than those reported in the quoted literature, because here a 2-k coverage factor has been chosen for the statistics (95% confidence bands) instead than 1-k (67% confidence bands). They are moreover consistent with the trend displayed by the melting/solidification points of intermediate compositions.

Table 5.1 summarises the melting / solidification points observed in the different $(U, Pu)O_2$ samples investigated in this work.

x(PuO$_2$)	Samples / shots	Melting temperature / K	Solidification temperature / K
0	2/15	-	3126 ± 55.1
0.037	3/17	3129 ± 65.4	3107 ± 56.0
0.09	3/9	3116 ± 70.2	3097 ± 60.8
0.25	3/28	3052 ± 63.6	3015 ± 55.5
0.4	6/41	3015 ± 55.8	2993 ± 52.7
0.5	2/11	3007 ± 52.8	2985 ± 51.3
0.8	1/7	3023 ± 54.6	3023 ± 52.1
0.9	1/12	3037 ± 60.2	3012 ± 51.0
1	1/6	3040 ± 59.9	3050 ± 55.1

Table 5.1: Melting points detected by RLS and solidification points observed by thermal arrest analysis in this work on $(U, Pu)O_2$ samples with amount of samples, total shots and 2σ uncertainty band

5.4. DISCUSSION

5.4.1. MELTING / SOLIDIFICATION PROCESSES IN PURE AND MIXED COMPOUNDS

The current melting point of uranium dioxide is slightly lower than the one reported in [3], whereas the melting point of PuO_2 is 33 K higher than the value proposed by DeBruycker et al. [4]. In both cases the differences are largely contained in the experimental error bands, still they can be explained. In fact, here UO_2 was investigated in an external inert gas pressure (0.3 MPa) close to atmospheric, whilst in [3] the value 3147 K was extrapolated from data recorded at high pressure (1 MPa and more), where the melting behaviour was less likely to be affected (lowered) by vaporisation. In the case of PuO_2 the current multiple-pulse laser heating/cooling cycle approach ensured a better mechanical stability compared with the single shots performed by DeBruycker et al. [4].

A noticeable point is that even in these pure compounds, where the melting/freezing transition is supposed to occur without any compositional change, i.e., congruently, the solidification arrest has a more complex shape than just the expected freezing plateau. Compared to earlier thermograms measured on the same compounds [3, 4], this effect is

due here to the fact that the sample cools naturally, without any "'laser conditioning"' of the high cooling speed. On one hand this precaution rules out any uncontrollable effect, on the observed solidification temperature, of the simultaneous presence of the solidi- fication enthalpy release and the heating laser. On the other hand, the high "'natural"' cooling rate (not laser-conditioned), combined with the relatively poor thermal conduc- tivity of uranium and plutonium dioxides, produces rather large thermal gradients at the periphery of the molten pool, especially during solidification. Consequently, the current phase transition dynamics become rather complex.

The aforementioned Phase - Field simulations of the present laser heating experi- ments help to shed some light on the phenomena involved. Solidification occurs in the cooling liquid pool (which generally extends from the sample surface for a few tens μm into the bulk) starting from preferential nucleation sites, namely the pool bottom and its boundaries on the surface (cf. [3]). The solid front then proceeds towards the cen- tre of the molten zone, where thermal equilibrium conditions are produced during the experiment and where temperature is measured in the pyrometers' focal spot (cf. [26]). However, under these conditions the release of the solidification enthalpy and its diffu- sion through the coexisting solid and liquid phases is rather complex and difficult to pre- dict. In addition, actinide diffusion is comparatively slow, especially in the solid [30–34]. This makes it difficult to clearly distinguish between a liquidus point (the temperature at which the first solid germ, with a changed composition, appears in the cooling liquid) and a solidus point (the temperature at which the last drop of cooling liquid becomes solid, with the initial composition). The occurrence of a solidus and a liquidus with different compositions implies in fact that the composition change is supported by a molecular diffusion faster than the cooling rate of the system. Such phenomena, already studied in earlier literature [35], can explain why segregation effects are very limited in the samples investigated here.

As a result, the rather complex features often displayed by the current experimen- tal thermal arrests can be attributed to the solidus/liquidus behaviour typical of non- congruent melting/freezing transitions only for compositions whose solidus and liq- uidus points are sufficiently far apart in temperature (order of a hundred K at least). In the other cases, only a melting/freezing temperature range can be defined based on the current experimental results. Such a temperature range can be defined by combining the RLS analysis on heating and the thermal arrest analysis on cooling. It can be seen in Fig. 5.3 that the two sets of melting/freezing points are in fair agreement, although RLS melting points are systematically slightly higher. This effect is probably due to the pres- ence of parasite reflections of the heating laser into the pyrometers, and can therefore be included in the uncertainty bands as a systematic error of the technique.

Fig. 5.4 reports, as an example, the comparison between a Phase-Field simulation and the corresponding experimental thermogram recorded on a U$_{0.75}$Pu$_{0.25}$O$_2$ sample. Despite some differences visible especially at the highest temperatures, where vapor- isation and liquid instability leading to additional thermal losses are most difficult to model, the simulation permits a direct interpretation of some features of the empirical thermogram.

The dashed curve represents the PuO$_2$ molar fraction on the sample surface. It shows that, following the UO$_2$-PuO$_2$ phase boundaries, rather well established in this compo-

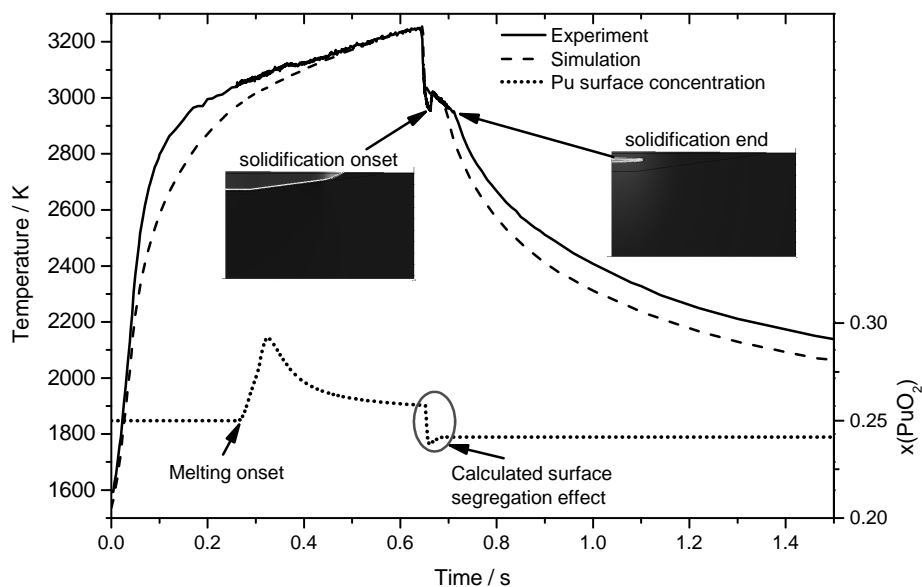Figure 5.4: Experimental thermograms (solid curve) and Phase - Field simulation (dashed curve) of a $U_{0.75}Pu_{0.25}O_2$ sample laser heated beyond melting. Dotted curve: PuO_2 concentration on the surface. In the insets: cross section of a sample from centre to rim. The white line represents the zone of the current phase change, with comparatively smaller liquid.

sitional range (see Section 5.4.3), the newly formed liquid surface is initially enriched in plutonium dioxide. Subsequently, due to fast diffusion in the liquid phase, the initial sample composition ($x(PuO_2) = 0.25$) tends to be rapidly restored. It is however clear, from the simulation, that the fast cooling occurring after the end of the laser pulse leads to onset of solidification before the initial composition is fully recovered in the liquid. A surface solid crust forms then upon freezing before the total liquid mass has crystallised (see insets in Fig. 5.4). The double inflection during cooling in this case corresponds to the solidification onset on the sample surface (first inflection) and to the disappearance of the last liquid inside the material (second inflection). The highest recalescence temperature represents the solidification point of a composition very close to the initial one (approximately ± 0.01 on $x(PuO_2)$ in the current example), except for small segregation effects. These latter have been studied also experimentally in the present research, by post-melting material characterisation.

5.4.2. PRE- AND POST-MELTING MATERIALS CHARACTERISATION

Pre- and post-melting material characterisation was carried out by XRD, XANES, and Raman Spectroscopy. In particular, the latter technique has been shown to be quick and effective for a rapid local analysis of the sample composition. For this purpose, the Raman active T_{2g} mode typical of fcc fluorite-structured dioxides (symmetry group: $Fm\bar{3}m$) [36] has been taken as a vibrational footprint for the different compounds. This Raman peak is well established to occur at (445 ± 1) cm^{-1} in pure UO_2 and (478 ± 1) cm^{-1} in
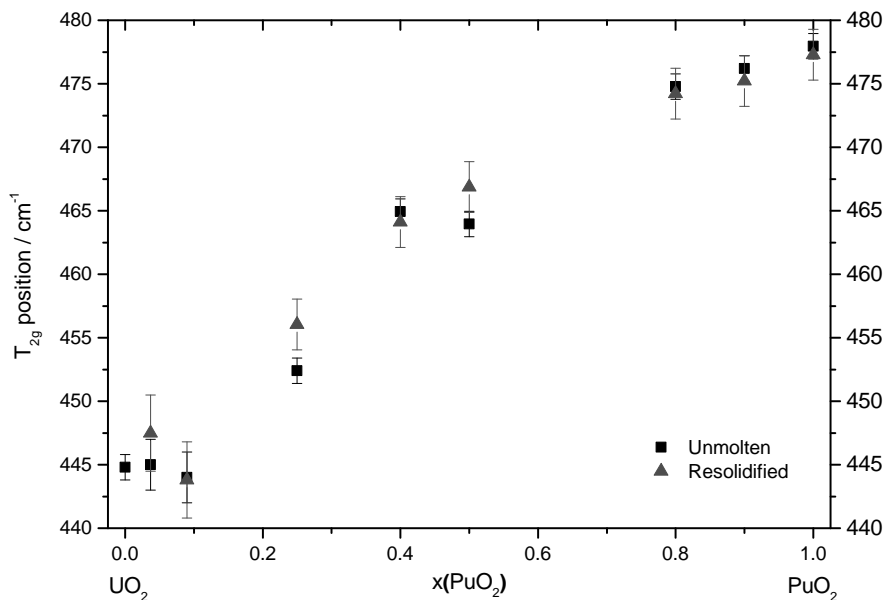
Figure 5.5: T$_{2g}$ Raman peak positions of re-solidified (triangles) and unmolten (squares) mixed UO$_2$-PuO$_2$ samples. (For interpretation of the references to colour in this figure legend, the reader is referred to the web version of this article.)

pure PuO$_2$ [37]. Comparing the T$_{2g}$ peak position in the molten and unmolten material yielded information on the possible occurrence of local segregation following the quick melting/freezing process (Fig. 5.5 and Tab. 5.2). It should be noted that for PuO$_2$ contents lower than 10 mol%, the Raman spectra revealed the formation of higher oxides (mostly U$_4$O$_2$ and U$_3$O$_8$) [38, 39] on the sample surface. Fluorescence induced by such oxides hindered the T$_{2g}$ peak analysis in MOX3.7 and MOX9, explaining the larger error band and the somewhat strange trend observed in Fig. 5.5 for these compositions. Only in the compositions x(PuO$_2$) = 0.25 and x(PuO$_2$) = 0.5, a non-negligible difference between fresh and melted material has been observed, attributable to such segregation effects. One can clearly see an evolution of the T$_{2g}$ position between the pure dioxides. On the other hand, a deeper analysis of the vibrational behaviour and Raman cross-section of the investigated materials would be needed in order to define a physically meaningful analytical dependence of the peak position on composition (cf. [40]).

XRD characterisation showed that no new phases (such as M$_2$O$_3$, M$_4$O$_9$ or M$_3$O$_8$, where M = U, Pu) were formed following the fast melting/freezing process, but the original fcc Fm$\bar{3}$m structure was maintained with the same lattice parameter (within the experimental uncertainty).

The lattice parameters obtained for the different x(PuO$_2$) by Rietveld analysis of the experimental XRD patterns are shown in Fig. 5.6.

Slight but obvious deviations from Vegard's law in different intermediate compositions can be attributed to three main reasons: uncertainty in the initially assumed composition of the starting material, segregation or a shift in the oxygen-to-metal (O/M)

x(PuO$_2$)	Re-solidified	Not melted
0	-	448.8
0.037	447.5	445.0
0.09	443.8	444.0
0.25	456.0	452.4
0.4	464.1	464.9
0.5	466.8	463.9
0.8	474.2	474.7
0.9	475.2	476.2
1	477.3	477.9

Table 5.2: Raman T$_{2g}$ peak positions observed for each composition of re-solidified and not melted material.

molar ratio during the melting process. In principle, it is not possible to distinguish a UO$_2$/PuO$_2$ composition shift from a shift in O/M through lattice parameter analysis only. However, from the chemical characterisation performed on the current samples before laser irradiation, the x(PuO$_2$) composition can be assumed to be affected by an uncertainty of ± 0.02. Since such an uncertainty would justify only very small shifts from Vegard's law, the observed positive variations of the lattice parameter can be safely at-
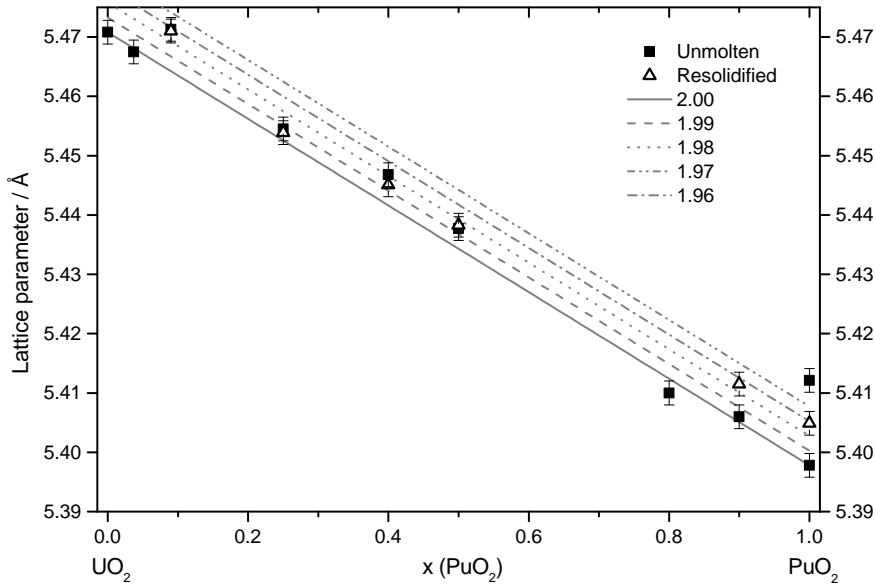
Figure 5.6: The lattice parameters obtained by Rietveld analysis of the experimental X-ray diffractograms for the different x(PuO$_2$) compositions investigated in this work. The black straight solid line represents Vegard's law for an oxygen-to-metal (O/M) ratio = 2.00. Parallel straight lines correspond to different O/M ratios based on data reported in [12]. The two unmolten plutonium dioxide represent a stoichiometric and a hypo-stoichiometric one with O/M = 1.88 ± 0.07.

tributed to deviations of the oxygen-to-metal molar ratio from the 2.00 exact stoichiometry. For this reason, Fig. 5.6 also reports straight lines parallel to Vegard's law curve for different O/M ratios, based on data reported in the literature for non-stoichiometric uraniumplutonium mixed dioxides [12]. It can thus be appreciated, from the XRD analysis, that the current samples are mostly slightly hypo-stoichiometric in oxygen. While the samples with low PuO$_2$ content do not show any clear difference between the melted / refrozen and the original material, a clear difference is visible only in the mixed composition richest in PuO$_2$ (MOX90). Because Raman spectroscopy ensured that no relevant uranium dioxideplutonium dioxide segregation occurred in MOX90 during the laser heating / cooling cycles (cf. Fig. 5.5), it must be concluded that non-negligible oxygen losses increasing the O/M ratio took place for this composition, probably fostered by the high plutonium content. This point should be further investigated in future research, also bearing in mind that in the present research oxidation state analysis based on X-ray absorption spectroscopy has been applied only to samples with lower plutonium dioxide contents, considered to be more essential for the nuclear fuel safety. It is worth pointing out here that no such difference in the lattice parameter was noticed in pure PuO2 before and after laser melting. However, it can be noted in Fig. 5.6 that different samples of pure PuO$_2$ present slightly different lattice parameters, too. The current PuO$_2$ samples differ by age (by a few years), so it is possible that the difference in their lattice parameters corresponds to slight oxygen losses and/or self-radiation damage over storage time. However, no related effect has been observed on the melting behaviour of these pure plutonium dioxide samples.

In conclusion it is clear, from the XRD characterisation, that oxygen behaviour in the mixed oxides, which is directly linked to the oxidation states of U and Pu, constitutes another paramount aspect of the fast heating cycles. If both uranium and plutonium should exist in the (IV) oxidation state in the ideal dioxides and their solid solution, a disproportion can occur, where uranium tends to be oxidised to the (V) or even (VI) states, whereas plutonium tends to be reduced to Pu(III). Moreover, at high temperature non-congruent vaporisation might occur. Such behaviour would have implications on the phase boundaries, which should therefore be considered not in the merely pseudo-binary system UO$_2$-PuO$_2$, but rather in the whole U-Pu-O ternary [6].

A first characterisation of the oxygen behaviour both in fresh and laser irradiated (U, Pu)O$_2$ samples has been performed with the help of XANES experiments.

XANES results at the U and Pu LIII edges in samples with $0 \leq x(PuO_2) \leq 0.5$, presented in Fig. 5.7 and Table 5.3, show that, for a given Pu content, the white lines of the melted and unmelted samples are very similar, indicating that the laser irradiation does not affect significantly the oxygen/metal stoichiometry. In addition, both U and Pu white lines of the MOX samples are well aligned with the UO$_2$ and PuO$_2$ reference compounds, which indicates that both U and Pu mostly remain in their tetravalent oxidation states [19] before and after laser irradiation. The O/M ratios of the melted and unmelted MOX samples remain therefore very close to 2.00.

However, slight shifts of 0.1(5) eV - 0.3(5) eV of the U LIII WL and of 0.1(5) eV - 0.3(5) eV of the Pu LIII WL were observed toward higher and lower energies, respectively (cf. Fig. 5.7a-5.7c and Table 5.3), both in molten and unmolten MOX samples. Considering the resolution uncertainty, a minor oxidation of the U(IV) to U(V) or U(VI) as well as
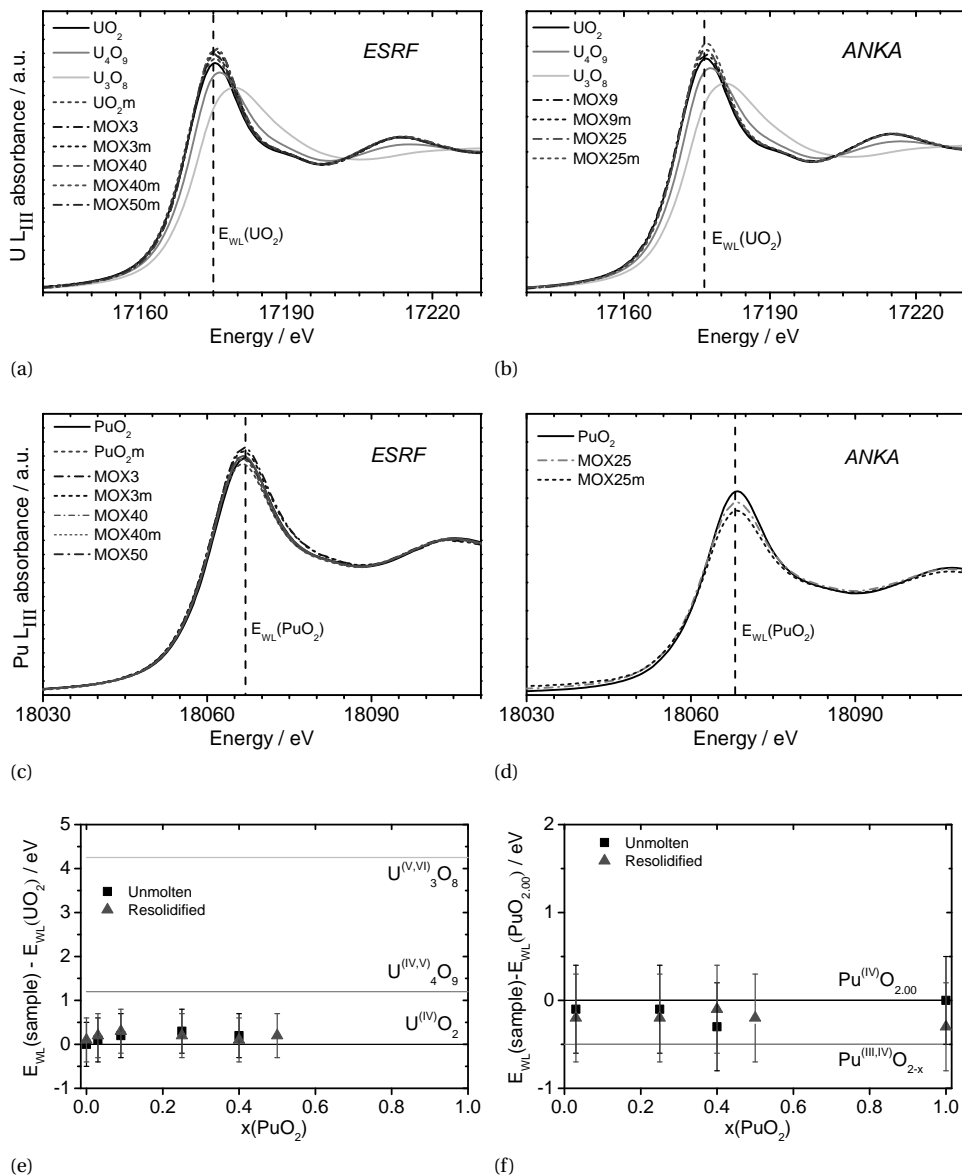
Figure 5.7: XANES spectra of the current MOX samples: (a) U LIII XANES spectra collected at ESRF (left) and ANKA (right), (b) Pu LIII XANES spectra collected at ESRF (left) and ANKA (right), (c) Shift of the U LIII and Pu LIII white line positions of the MOX samples compared to the UO_2 (left) and PuO_2 (right) white line as a function of the PuO_2 content.

5

	U LIII edge				Pu LIII edge			
	ANKA		ESRF		ANKA		ESRF	
	E_{WL} (eV)	ΔE_{WL} (eV)	E_{WL} (eV)	ΔE_{WL} (eV)	E_{WL} (eV)	ΔE_{WL} (eV)	E_{WL} (eV)	ΔE_{WL} (eV)
References								
UO$_2$	17176.5	0	17174.8	0	-	-	-	-
U$_4$O$_9$	17177.7	1.2	17175.8	1	-	-	-	-
U$_3$O$_8$	17180.9	4.4	17178.9	4.1	-	-	-	-
PuO$_2$	-	-	-	-	18068.1	0	18067.4	0
PuO$_{2-x}$	-	-	-	-	18067.6	-0.5	18066.9	-0.5
Samples								
UO$_2$m	n.m.	-	17174.9	0.1	-	-	-	-
MOX 3	n.m.	-	17174.9	0.1	n.m.	-	18067.3	-0.1
MOX 3m	n.m.	-	17175.0	0.2	n.m.	-	18067.2	-0.2
MOX 9	17176.7	0.2	n.m.	-	n.d.	-	n.m.	-
MOX 9m	17176.6	0.1	n.m.	-	n.d.	-	n.m.	-
MOX 25	17176.6	0.1	n.m.	-	18068.0	-0.1	n.m.	-
MOX 25m	17176.7	0.2	n.m.	-	18067.9	-0.2	n.m.	-
MOX 40	n.m.	-	17175.1	0.3	n.m.	-	18067.1	-0.3
MOX 40m	n.m.	-	17175.0	0.2	n.m.	-	18067.3	-0.1
MOX 50m	n.m.	-	17175.0	0.2	n.m.	-	18067.2	-0.2
PuO$_2$m	-	-	-	-	n.m.	-	18067.1	-0.3

Table 5.3: Energy of the white line positions E_{WL} at the U LIII and Pu LIII edges.
Notes: n.m.: not measured; n.d.: not detected, the noise to signal ratio of the XANES fluorescence spectrum was too high; ΔE_{WL} is the difference between the EWL of the sample and the EWL of the UO$_2$, respectively, PuO$_2$, measured at the same beamline. 2.4.

a minor reduction of Pu(IV) to Pu(III) cannot be totally discarded. Regarding an hypo-
thetical U oxidation in the mixed oxide samples, the oxidation of U(IV) to uranyl U(V)
or U(VI) seems quite unlikely as no shoulder located 15 eV after the WL, specific feature
or uranyl U(V)/U(VI), was obviously detected on the XANES and HR-XANES spectra [19]
(see Figs. 5.7 and 5.8). Therefore, we assume that if the shift of the ULIII WL can be
considered as significant with respect to the reported experimental uncertainty, U(IV)
in the MOX samples is slightly oxidized to the U(V) uranate type of bonding. This in-
terpretation is consistent with the fact that the experimental HRXANES spectrum of the
MOX9 resembles more closely the one of UO_2 and $U(IV/V)_4O_9$ than the $U(V/VI)_3O_8$ ref-
erence spectra (Fig. 5.8). The co-existence of small fractions of U(V) and Pu(III) could
be possible as the presence of U(V) compensating for a trivalent cation has already been
evidenced in similar fluorite solid solutions [20, 41]. If this were the case, the exact O/M
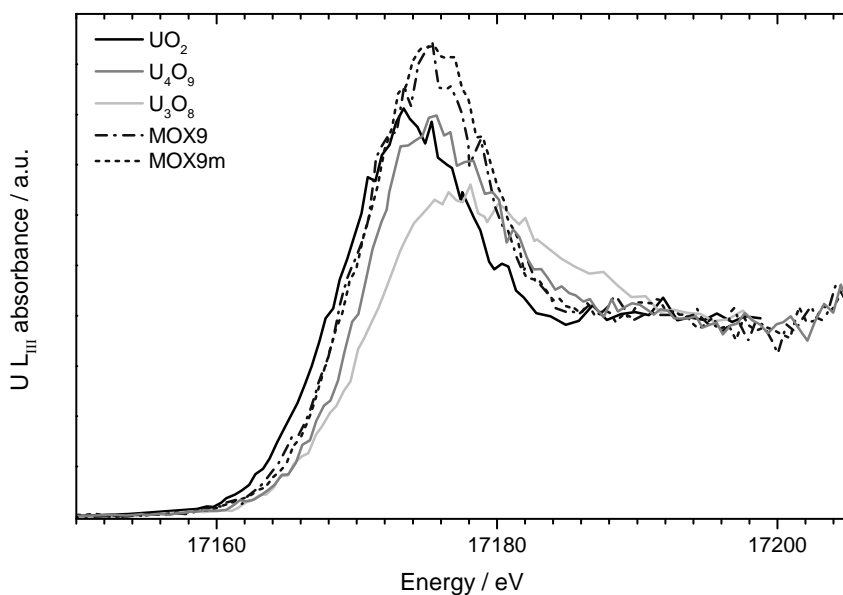= 2.00 stoichiometry would be still at the instrumental uncertainty limit (± 0.03).

Figure 5.8: HR-XANES spectra of MOX9 samples at the U LIII edge.

It is important to observe that U(V) and Pu(III) would already be present in the start-
ing unmolten materials. This is a possible consequence of the high-temperature an-
nealing to which samples were subjected prior to the laser heating in order to stabilise
the O/M molar ratio at a value as close as possible to 2.00 [5]. This observation might
surprise, as the current urania-rich samples have been stored and laser-heated always
under an inert atmosphere (nitrogen and pressurised argon, respectively). However, it
shows how sensitive to the formation of oxygen defects the current materials can be.
This is also one of the crucial points concerning the nuclear fuel's chemical stability [42].
In addition, one cannot exclude the occurrence of reversible deviations from the O/M
= 2.00 stoichiometry at very high temperature, where the dioxide is subject to strongly

non-congruent vaporisation [6]. This last point is important for predicting the real nuclear fuel behaviour. It is in fact well known [42] that the fuel O/M can change considerably from the stoichiometric 2.00 value as a function of the temperature distribution during in-pile operation.

According to the present Raman, XRD and XANES analyses, very little segregation or oxygen losses are observable in the mixed uranium dioxide-plutonium dioxide samples after laser heating beyond melting, particularly for x(PuO$_2$) ≤ 0.5. This is due to the fact that liquid/solid/gas phase boundaries are probably rather close together in this part of the U-Pu-O system, and to the rapidity of the current heating/cooling processes (cf. [35]). Accordingly, the uncertainty relative to the resulting experimental data points reported in Fig. 5.3 are representative of the temperature range across which the liquid/solid transition occurs at each composition, and take into account also difficulties in locating the exact liquidus and solidus points, as mentioned before. Possibly, more significant shifts in the O/M or even in the UO$_2$/PuO$_2$ ratio would have been observed with slower heating/cooling rates.

5.4.3. COMPARISON WITH CALPHAD OPTIMISED PHASE BOUNDARIES

In order to shed some light on the way such deviations might shift the melting / solidification data points reported in Fig. 5.3, these current experimental results are compared in Fig. 5.9a-5.9d with previous data, and the phase diagram optimisation performed by Guéneau et al. with the CALPHAD approach [6].

The agreement between the current and previous furnace-heating data is obviously good in the UO$_2$-rich part of the phase diagram, where the oxygen potential is the lowest.

On the other hand, it is confirmed that the solid/liquid phase boundaries should be placed at temperatures higher than those measured with traditional heating methods in samples with higher PuO$_2$ concentrations. This confirms the CALPHAD prediction plotted in Fig. 5.9, that a minimum melting point should exist in the UO$_2$PuO$_2$ system, at a composition between x(PuO$_2$) = 0.4 and x(PuO$_2$) = 0.7. By considering current and previous data, such minimum melting point is probably located between 2900 K and 3000 K. The large uncertainty still affecting its exact value is certainly linked to the O/M molar ratio stability at very high temperature.

The comparison of experimental data and CALPHAD phase boundary optimisation is shown in Fig. 5.9 in four transversal sections of the ternary U-Pu-O phase diagram: UO$_2$-PuO$_2$ (a), UO$_{2.03}$-PuO$_2$ (b), UO$_2$-PuO$_{1.96}$ (c) and UO$_{1.98}$-PuO$_{1.96}$ (d). These compositions have been selected in order to compare experimental results with different combination of oxygen/metal (O/M) molar ratios across the phase diagram. They are indicative of the four most likely situations: perfect stoichiometry (a), partial hyperstoichiometry (b), partial hypo-stoichiometry (c) and complete hypo-stoichiometry (d). It can be noticed that, consistently with published calculations [5], a stable gas phase is foreseen to be present at the equilibrium in the PuO$_2$-rich part of each section, unless this is sufficiently hypo-stoichiometric as to stabilise the condensed phase (Fig. 5.9c-5.9d). Independently, the qualitative agreement between the current experimental data and the CALPHAD phase boundaries seems to be acceptable in the four cases.

It is therefore clear, from the current investigation and CALPHAD optimisation, that oxygen equilibria do play a role in these phase boundaries and all the experimental data
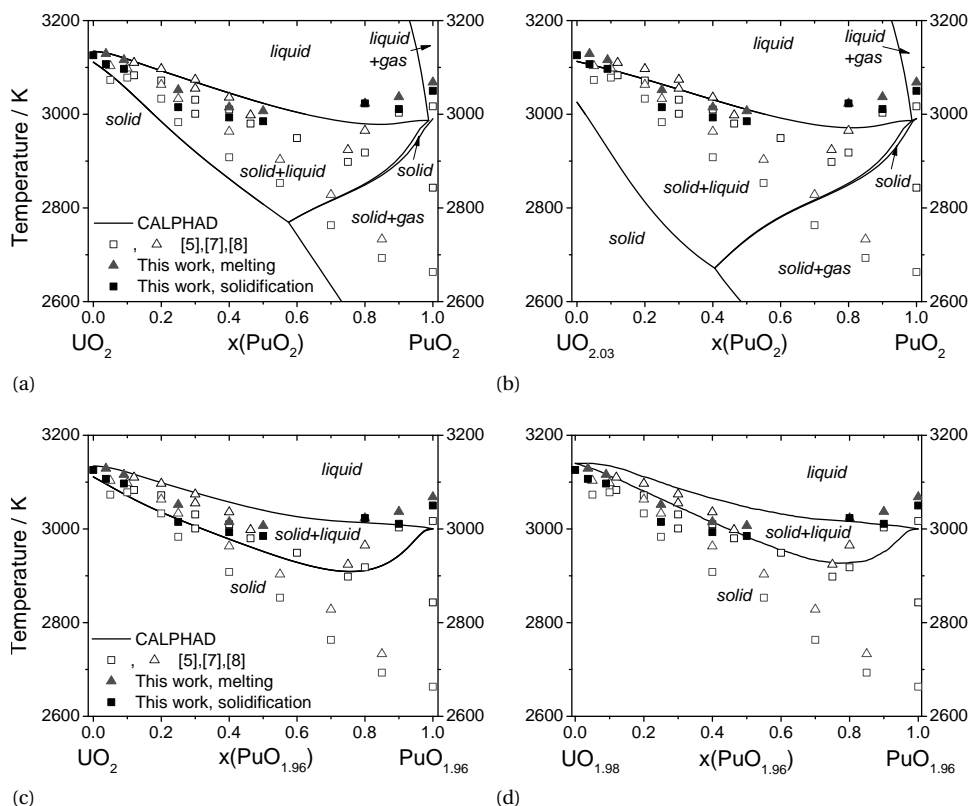
Figure 5.9: The current (squares and triangles) and literature experimental data points (solidus as squares and liquidus as triangles are taken from [5, 7, 8]) compared with CALPHAD optimised phase boundaries (black dashed curves after [6]): (a) In the pseudo-binary UO_2-PuO_2 phase diagram, (b) In the "'skew"' $UO_{2.03}$-PuO_2 section of the U-Pu-O ternary system, (c) In the "'skew"' UO_2-$PuO_{1.96}$ section, (d) In the "'skew"' $UO_{1.98}$-$PuO_{1.96}$ section.

points (both cur- rent and earlier) should be considered with uncertainty bars also in the sense of the O/M molar ratio (perpendicularly to the UO_2-PuO_2 plane in the ternary phase diagram). Further research is being carried out in order to better define such additional uncertainty bands.

On the other hand, the effect of these oxygen equilibria affects only to a limited extent the qualitative trend of the solidusliquidus surfaces in the ternary U-Pu-O system in the vicinity of the UO_2-PuO_2 solid solution. In fact, Fig. 5.9a-5.9d together with the current Raman, XRD and XANES results show that the temperature range within which the melting/solidification transition has been measured in this work is well indicative of the solid/liquid equilibria in the uranium dioxideplutonium dioxide system independently of small variations of the O/M ratio and uncertainties.

5.5. CONCLUSION

IN order to complement recent studies of the melting behaviour of pure plutonium dioxide and $(U, Pu)O_2$ samples with high-PuO_2 contents, new results have been obtained on the same material system at JRC-ITU by fast quasi-containerless laser heating. They confirm earlier furnace heating data in the uranium-dioxide rich part of the phase diagram, and more recent laser-heating data in the plutonium-dioxide side of the system. They suggest that a minimum melting point must exist in the UO_2-PuO_2 system, at a composition between x(PuO_2) = 0.4 and x(PuO_2) = 0.7 and 2900 K ± T ± 3000 K. Taking into account that, especially at high temperature, oxygen defects and O/M molar ratio variations have an effect on the reported phase boundary uncertainties, the current results should be projected in the ternary U-Pu-O system. Further research is on-going, aiming at a better definition of uncertainty bands in the O/M molar ratio both at room and high temperature. However, these uncertainty bands are not expected to significantly affect the qualitative trend of the current solidliquid phase boundaries.

The current results have important implications not only in terms of fundamental materials understanding, but also for the comprehension of the nuclear fuel behaviour in case of an accident during which the temperature would exceed the melting limit. In particular, the new insight provided by the current work will help to clarify and reduce the margin to melting uncertainties.

REFERENCES

[1] R. Böhler, M. Welland, D. Prieur, P. Çakır, T. Vitova, T. Pruessmann, I. Pidchenko, C. Hennig, C. Guéneau, R. Konings, and D. Manara, *Recent advances in the study of the UO_2-PuO_2 phase diagram at high temperatures,* J. Nucl. Mater. **448**, 330 (2014).

[2] D. Manara, M. Sheindlin, W. Heinz, and C. Ronchi, *New techniques for high-temperature melting measurements in volatile refractory materials via laser surface heating,* Rev. Sci. Instrum. **79**, 113901 (2008).

[3] D. Manara, C. Ronchi, M. Sheindlin, M. Lewis, and M. Brykin, *Melting of stoichiometric and hyperstoichiometric uranium dioxide,* J. Nucl. Mater. **342**, 148 (2005).

[4] F. De Bruycker, K. Boboridis, D. Manara, P. Pöml, M. Rini, and R. J. Konings, *Reassessing the melting temperature of PuO_2,* Mater. Today **13**, 52 (2010).

[5] F. De Bruycker, K. Boboridis, R. Konings, M. Rini, R. Eloirdi, C. Guéneau, N. Dupin, and D. Manara, *On the melting behaviour of uranium/plutonium mixed dioxides with high-Pu content: A laser heating study,* J. Nucl. Mater. **419**, 186 (2011).

[6] C. Guéneau, N. Dupin, B. Sundman, C. Martial, J.-C. Dumas, S. Gossé, S. Chatain, F. D. Bruycker, D. Manara, and R. J. Konings, *Thermodynamic modelling of advanced oxide and carbide nuclear fuels: Description of the U-Pu-O-C systems,* J. Nucl. Mater. **419**, 145 (2011).

[7] W. Lyon and W. Baily, *The solid-liquid phase diagram for the UO_2-PuO_2 system,* J. Nucl. Mater. **22**, 332 (1967).

[8] M. Kato, K. Morimoto, H. Sugata, K. Konashi, M. Kashimura, and T. Abe, *Solidus and liquidus temperatures in the $UO_2 - PuO_2$ system,* J. Nucl. Mater. **373**, 237 (2008).

[9] T. Hirosawa and I. Sato, *Burnup dependence of melting temperature of FBR mixed oxide fuels irradiated to high burnup,* J. Nucl. Mater. **418**, 207 (2011).

[10] D. Manara, R. Böhler, K. Boboridis, L. Capriotti, A. Quaini, L. Luzzi, F. De Bruycker, C. Guéneau, N. Dupin, and R. Konings, *The Melting Behaviour of Oxide Nuclear Fuels: Effects of the Oxygen Potential Studied by Laser Heating,* Procedia Chem. **7**, 505 (2012).

[11] H. Kinoshita, D. Setoyama, Y. Saito, M. Hirota, K. Kurosaki, M. Uno, and S. Yamanaka, *Thermodynamic modelling and phase stability assessment of MO_{2-x} oxides with a fluorite structure,* J. Chem. Thermodyn. **35**, 719 (2003).

[12] C. Guéneau, A. Chartier, and L. V. Brutzel, *2.02 - Thermodynamic and Thermophysical Properties of the Actinide Oxides,* in *Compr. Nucl. Mater.*, edited by R. J. Konings (Elsevier, Oxford, 2012) pp. 21–59.

[13] L. Petit, A. Svane, Z. Szotek, W. M. Temmerman, and G. M. Stocks, *Electronic structure and ionicity of actinide oxides from first principles,* Phys. Rev. B **81**, 045108 (2010).

[14] J. Parker, D. Feldman, and M. Ashkin, *Raman Scattering by Silicon and Germanium,* Phys. Rev. **155**, 712 (1967).

[15] T. Vitova, K. O. Kvashnina, G. Nocton, G. Sukharina, M. A. Denecke, S. M. Butorin, M. Mazzanti, R. Caciuffo, A. Soldatov, T. Behrends, and H. Geckeis, *High energy resolution x-ray absorption spectroscopy study of uranium in varying valence states,* Phys. Rev. B **82**, 235118 (2010).

[16] J. Rothe, S. Butorin, K. Dardenne, M. A. Denecke, B. Kienzler, M. Löble, V. Metz, A. Seibert, M. Steppert, T. Vitova, C. Walther, and H. Geckeis, *The INE-Beamline for actinide science at ANKA,* Rev. Sci. Instrum. **83**, 043105 (2012).

[17] W. Matz, N. Schell, G. Bernhard, F. Prokert, T. Reich, J. Clauß ner, W. Oehme, R. Schlenk, S. Dienel, H. Funke, F. Eichhorn, M. Betzl, D. Pröhl, U. Strauch, G. Hüttig, H. Krug, W. Neumann, V. Brendler, P. Reichel, M. A. Denecke, and H. Nitsche, *ROBL a CRG beamline for radiochemistry and materials research at the ESRF,* J. Synchrotron Radiat. **6**, 1076 (1999).

[18] B. Ravel and M. Newville, *ATHENA, ARTEMIS, HEPHAESTUS: data analysis for X-ray absorption spectroscopy using IFEFFIT,* J. Synchrotron Radiat. **12**, 537 (2005).

[19] S. D. Conradson, D. Manara, F. Wastin, D. L. Clark, G. H. Lander, L. A. Morales, J. Rebizant, and V. V. Rondinella, *Local structure and charge distribution in the UO_2 - U_4O_9 system,* Inorg. Chem. **43**, 6922 (2004).

5

[20] D. Prieur, P. M. Martin, A. Jankowiak, E. Gavilan, A. C. Scheinost, N. Herlet, P. De-haudt, and P. Blanchart, *Local structure and charge distribution in mixed uranium-americium oxides: effects of oxygen potential and Am content,* Inorg. Chem. **50**, 12437 (2011).

[21] S. D. Conradson, K. D. Abney, B. D. Begg, E. D. Brady, D. L. Clark, C. den Auwer, M. Ding, P. K. Dorhout, F. J. Espinosa-Faller, P. L. Gordon, R. G. Haire, N. J. Hess, R. F. Hess, D. W. Keogh, G. H. Lander, A. J. Lupinetti, L. A. Morales, M. P. Neu, P. D. Palmer, P. Paviet-Hartmann, S. D. Reilly, W. H. Runde, C. D. Tait, D. K. Veirs, and F. Wastin, *Higher order speciation effects on plutonium L_3 X-ray absorption near edge spectra.* Inorg. Chem. **43**, 116 (2004).

[22] P. Martin, S. Grandjean, C. Valot, G. Carlot, M. Ripert, P. Blanc, and C. Hennig, *XAS study of $(U_{1-y}Pu_y)O_2$ solid solutions,* J. Alloys Compd. **444-445**, 410 (2007).

[23] R. C. Belin, P. M. Martin, J. Lechelle, M. Reynaud, and A. C. Scheinost, *Role of cation interactions in the reduction process in plutonium-americium mixed oxides,* Inorg. Chem. **52**, 2966 (2013).

[24] S. Grandjean, B. Arab-Chapelet, A. Robisson, F. Abraham, P. Martin, J.-P. Dancausse, N. Herlet, and C. Léorier, *Structure of mixed U(IV)An(III) precursors synthesized by co-conversion methods (where An=Pu, Am or Cm),* J. Nucl. Mater. **385**, 204 (2009).

[25] M. Welland, W. Thompson, B. Lewis, and D. Manara, *Computer simulations of non-congruent melting of hyperstoichiometric uranium dioxide,* J. Nucl. Mater. **385**, 358 (2009).

[26] R. Böhler, M. J. Welland, F. D. Bruycker, K. Boboridis, A. Janssen, R. Eloirdi, R. J. M. Konings, and D. Manara, *Revisiting the melting temperature of NpO_2 and the challenges associated with high temperature actinide compound measurements,* J. Appl. Phys. **111**, 113501 (2012).

[27] J. Fink, *Thermophysical properties of uranium dioxide,* J. Nucl. Mater. **279**, 1 (2000).

[28] P. Papon, J. Leblond, and P. H. Meijer, *The Physics of Phase Transitions* (Springer, 2006).

[29] L. Epstein, *Ideal solution behavior and heats of fusion from the UO_2-PuO_2 phase diagram,* J. Nucl. Mater. **22**, 340 (1967).

[30] Q. Yin and S. Savrasov, *Origin of Low Thermal Conductivity in Nuclear Fuels,* Phys. Rev. Lett. **100**, 225504 (2008).

[31] M. Bober and G. Schumacher, *Material transport in the temperature gradient of fast reactor fuels,* in *Adv. Nucl. Sci. Technol. Vol. 7,* edited by E. J. Henley and J. Lewins (Academic, New York, 1973) pp. 495–564.

[32] H. Matzke, *Diffusion processes and surface effects in non-stoichiometric nuclear fuel oxides UO_{2+x}, and $(U, Pu)O_{2+x}$,* J. Nucl. Mater. **114**, 121 (1983).

5

[33] M. J. Welland, *3.21 - Matter Transport in Fast Reactor Fuels,* in *Compr. Nucl. Mater.,* edited by R. J. Konings (Elsevier, Oxford, 2012) pp. 629–676.

[34] V. Di Marcello, A. Schubert, J. van de Laar, and P. Van Uffelen, *Extension of the TRANSURANUS plutonium redistribution model for fast reactor performance analysis,* Nucl. Eng. Des. **248**, 149 (2012).

[35] M. J. Aziz and T. Kaplan, *Continuous growth model for interface motion during alloy solidification,* Acta Metall. **36**, 2335 (1988).

[36] V. G. Keramidas, *Raman spectra of oxides with the fluorite structure,* J. Chem. Phys. **59**, 1561 (1973).

[37] G. Begun, R. Haire, W. Wilmarth, and J. Peterson, *Raman spectra of some actinide dioxides and of EuF_2,* J. Less Common Met. **162**, 129 (1990).

[38] H. Idriss, *Surface reactions of uranium oxide powder, thin films and single crystals,* Surf. Sci. Rep. **65**, 67 (2010).

[39] L. Desgranges, G. Baldinozzi, P. Simon, G. Guimbretière, and A. Canizares, *Raman spectrum of U_4O_9: a new interpretation of damage lines in UO_2,* J. Raman Spectrosc. **43**, 455 (2012).

[40] J.-C. Panitz, J.-C. Mayor, B. Grob, and W. Durisch, *A Raman spectroscopic study of rare earth mixed oxides,* J. Alloys Compd. **303-304**, 340 (2000).

[41] D. Prieur, P. Martin, F. Lebreton, T. Delahaye, D. Banerjee, A. C. Scheinost, and A. Jankowiak, *Accommodation of multivalent cations in fluorite-type solid solutions: Case of Am-bearing UO_2,* J. Nucl. Mater. **434**, 7 (2013).

[42] D. Olander, *Nuclear fuels - Present and future,* J. Nucl. Mater. **389**, 1 (2009).

5

6

THE SOLIDIFICATION BEHAVIOUR OF THE UO$_2$-THO$_2$ SYSTEM

Robert Böhler, Andrea Quaini, Luca Capriotti, Pelin Çakir, Ondrej Beneš, Konstantinos Boboridis, Antony Guiot, Lelio Luzzi, Rudy J.M. Konings, Dario Manara

The high-temperature phase diagram of the UO$_2$ – ThO$_2$ system has been experimentally revisited in the present study for the first time since 1970, using a laser heating approach combined with fast pyrometry in a thermal arrest method. The melting / solidification temperature, which is of fundamental information for a reactor design was studied here. It was found that low addition of ThO$_2$ to UO$_2$ would result in a slight decrease of the solidification temperature. A minimum was found at 3098 K around a composition of 5 mol % ThO$_2$. The solid / liquid transition temperature was then observed to increase again with increasing ThO$_2$ fraction. The literature value of pure ThO$_2$ (around 3630 K) was well reproduced here. Important experimental difficulties, stemming from the high temperatures reached during the measurements, as well as a complete investigation with electron microscopy, Raman spectroscopy and powder X-ray diffraction, are extensively discussed. These results show the importance of the high-temperature oxygen chemistry in this actinide oxide compound.

6.1. INTRODUCTION

T HERE is a renaissance of interest in thorium based fuels as an alternative to uranium based fuels in nuclear reactors. Thorium has advantages in terms of proliferation, waste management, supply and safety [2]. However, there are still technical and safety related issues to bring it to a fully commercial use [3–5]. UO$_2$ – ThO$_2$ mixed fuels (or (U,Th)O$_2$; abbreviated here as TOX) have advantages with respect to proliferation resistance for nuclear weapons and long term waste concerns over pure UO$_2$ fuel [6–8]. One reason why the thorium containing fuels are possibly advantageous compared to pure UO$_2$ are their material properties, more specifically, the properties of ThO$_2$. ThO$_2$ is a highly stable oxide, not subjected to oxidation beyond the stoichiometric composition, and its thermal conductivity is higher than that of uranium dioxide [9]. These properties together with the very high melting temperature of ThO$_2$, constitute obvious advantages in terms of the in-pile fuel performance of TOX fuel [10] and also a rather stable and less radiotoxic form for the waste with less minor actinides [11]. But compared to UO$_2$ the (U,Th)O$_2$ mixed fuels are investigated rather poorly. Especially the high temperature properties are only investigated in earlier research by Lambertson et al. and Latta et al. [12, 13]. Interestingly Latta et al. found a minimum temperature around 5 mol % ThO$_2$, but did not provide an explanation of this surprising deviation of ideal behaviour. The end-members of this system were studied more recently by Manara et al. (UO$_2$ [14]) and Ronchi and Hiernaut (ThO$_2$ [15]).

One of the main goals of the present work is to remeasure the full UO$_2$ - ThO$_2$ pseudo-binary section, whereby the melting / solidification behaviour of these mixed oxides are studied by laser heating and fast pyrometry under controlled atmosphere. This setup has been used for measuring some high temperature phase changes of refractory materials (e.g. [14, 16, 17]) revealing new results on the melting behaviour. First studies in mixed actinide oxide compounds, namely on mixed uranium-plutonium dioxides revealed also large differences to earlier believed ideal behaviour of this system at high temperatures [18]. New studies on the mixed (U,Pu)O$_2$ system confirmed these observations of a minimum temperature in the melting / solidification transition [19]. A conclusion obtained of the latter work is that the high temperature phase transitions are sensitive to the oxygen potential and can be fully understood only in the light of ternary systems of the mixed oxide components [20, 21]. ThO$_2$ in contrast is chemically more stable and has a lower oxygen potential than the other actinide oxides [22]. This makes it therefore chemically more stable also at high temperatures. Under those conditions it was interesting to check on one hand the high temperature behaviour of a nuclear fuel material, as well as, on the other hand, fundamental aspects of a system for which an essentially ideal solution behaviour can be foreseen at high temperatures.

The results of the laser melting experiments are completed with different methods as scanning electron microscopy (SEM), Energy-dispersive X-ray spectroscopy (EDX), X-ray diffraction (XRD) and Raman spectroscopy. Among these, Raman analysis of actinide compounds is a rather original method to investigate the material surfaces [23, 24]. The UO$_2$ – ThO$_2$ pseudo-binary phase diagram was finally refined with new experimental high temperature phase change data.

6.2. DESCRIPTION OF THE EXPERIMENTS

6.2.1. SAMPLE PREPARATION

The UO_2 - ThO_2 mixed samples were prepared using a sol-gel external gelation method with different molar fractions of ThO_2 ($x(ThO_2)$ = 0.05, 0.20, 0.40, 0.60, 0.80, 0.95, 1.00). The different samples were identified with the label TOX and the amount-of-substance fraction $x(ThO_2)\cdot 100$. Chemically, the samples contained besides uranium and thorium negligible amounts of different metals (< 0.1 wt. %). The powder / sol-gel beads were produced by precipitation of the U / Th solution in small droplets. These beads were heated in air to remove the organics at 400°C. Then the sol-gel beads were calcined in quartz crucibles at 800°C in air to remove the organics from the sol-gel process and convert the U-Th-hydroxide precipitation to form the $(U,Th)O_{2+x}$. After 2 h the gas is changed to Ar / H_2 to reduce the uranium back to U^{IV}. Finally, the powder is pressed to pellets of about 5 mm in diameter and 2 - 3 mm thickness. These pellets are sintered at 1650°C for 8 hours in Ar/H_2 to obtain a O/M ratio of 2.00.

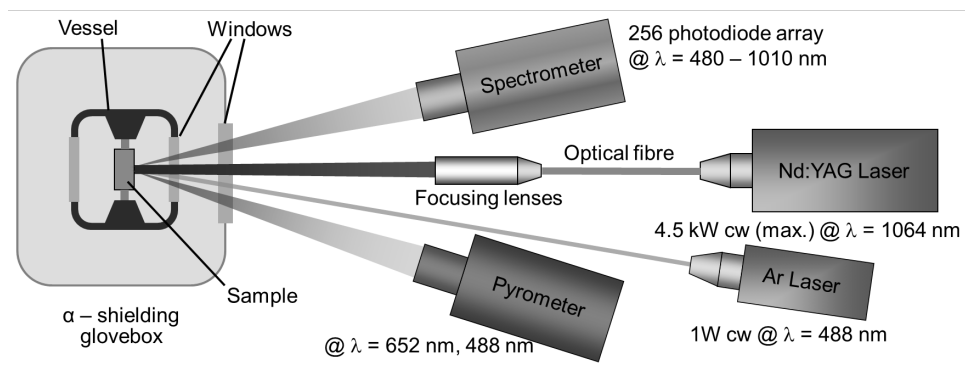### 6.2.2. LASER MELTING EXPERIMENTAL SETUP

Figure 6.1: A schematic description of the used apparatus for the melting experiments.

The experimental apparatus used in this work is summarised in Fig. 6.1 and was already described in detail elsewhere [14]. The sample was mounted in a pressurized cell with a controlled atmosphere, which was inside an α shielding glovebox. The contact between the sample and its mount was minimized by radially arranged screws to hold the sample in place. With this approach the molten volume is contained by the outer periphery of colder solid material, thus, preventing contamination by foreign material, hence can be described as quasi - containerless. The power source for heating was a Nd:YAG continuous-wave laser radiating at 1064.5 nm. The laser is programmable with a power/time profile of variable duration as short as a few milliseconds and a maximum power of 4.5 kW. However the heating profile was kept simple in order to separate better power changes from a thermal signal response.

The samples were preheated with low laser powers (45 W or 90 W) for 30 s to reduce thermal shocks. After this time a sufficient steady state heat distribution through the sample with a measured front surface temperature of 1500 K to 2000 K has established

and the sample was brought to melting with pulses of different length (100 ms to 1 s) at a constant power plateau (up to 600 W). The chosen power depends also on the composition of the sample since ThO$_2$ is in the near infra-red (laser wavelength) nearly transparent. This transparency is temperature dependant and disappears at high temperature where absorption / emissivity values similar to other actinide dioxides are reached [15].

After each pulse the power was set back to the preheating value to let the sample re-solidify and reach again a homogeneous state before the next pulse was started. A maximum of 3 pulses were applied in a set of shots before letting the sample cool naturally. Such heating cycles were performed under air for compositions rich in ThO$_2$ and Ar for intermediate and UO$_2$-rich compositions. The buffer gas was slightly pressurized up to 0.3 MPa to reduce the vaporisation. The onset of melting was detected by the appearance of vibrations in the signal of a probe laser (Ar$^+$ cw 750 mW to 1.5 W) reflected by the sample surface (reflected-light-signal technique, or RLS)[25]. These vibrations disappear during the solidification process at the thermal arrest and therefore establish the temperature at the thermal arrest as the solidification temperature.

The surface radiance temperature in the centre of the heated zone was measured by a pyrometer operating at 652 nm and with a fast logarithmic amplifier. The nominal spot size was approximately 0.5 mm in diameter. The pyrometer was calibrated against a standard tungsten-ribbon lamp in the range 1800 K to 2500 K, ensuring traceability to the International Temperature Scale of 1990 [26]. The validity of the calibration, the quality of the optical windows, the alignment, and the thermodynamic equilibrium conditions on the measurement spot were tested by measuring in-situ the well established melting radiance temperatures of UO$_2$ (3040 K [14]) and tungsten (3207 K [27]) close to 650 nm.

The true temperature was obtained by correcting the radiance temperature with the measured of the normal spectral emittance NSE ($\varepsilon(\lambda, T)$). A further spectrometer, based on a linear array of 256 photodiodes, was used to record the sample thermal radiance in the range of 488 to 1011 nm, whereby the time resolution is one spectrum per millisecond at best. The photodiode at 649 nm was calibrated up to 2500 K using the tungsten-ribbon lamp and this calibration was transferred to a tubular - cavity variable - temperature graphite blackbody furnace up to 3500 K. The remaining photodiodes were then calibrated with this blackbody, allowing a conversion of output signal to spectral radiance over the entire useful wavelength range.

The measured radiance spectra can be fitted with two physically equivalent methods: by a least-squares regression to Plancks distribution law or by the radiance temperature, T_λ, plotted as a function of wavelength, λ, assuming a grey body with constant wavelength independent emissivity $\varepsilon(T)$. Both methods were successfully applied on other actinide dioxides and are shown in detail elsewhere [17, 28]. For UO$_2$ the already published data is used [29], while the high temperature value (0.870 $\pm$ 0.044) obtained during the present work with both fits was adopted for pure ThO$_2$. This is in agreement with earlier results of ThO$_2$ [15, 30] and is also supported by analogy to emittance data of other similar dioxides [17, 28]. The emittance study could not be performed on all compositions. A linear interpolation between the two NSE of UO$_2$ and ThO$_2$ was calculated, giving to the generic intermediate composition a weighted value related to the amount of the two pure components, which are shown in Tab. 6.1. This assumption seems reasonable especially considering the close emittance values of the two end members and

agreed well with the calculated values for some intermediate compositions.

The sample surface was considered to be smooth, as supported by the good repeatability of the measured radiance temperatures upon freezing. The freezing temperature of TOX was determined from the cooling stage of the recorded thermograms, locating the corresponding thermal arrest. As often observed in rapid laser-heating experiments of such materials, and confirmed by numerical simulation [17], the heating stage often occurs too quickly to reveal an observable melting arrest during this phase of the thermal cycle but could be estimated with the help of the RLS.

Uncertainties of the measurements were calculated according to the error - propagation law, taking into account the uncertainty associated to pyrometer calibration, the emissivity, transmittance of the optical system and the accuracy in detecting the onset of vibrations in the reflected light signal. The estimated cumulative uncertainty is thus lower than ± 2.5 % of the reported temperatures in the worst cases for solidification temperatures and ± 3.5 % for melting transitions (calculated with a coverage factor k = 2).

6.2.3. MATERIAL CHARACTERISATION

To check the composition, the material was investigated with different methods before and after the experiments. First, secondary electron (SE) and backscattered electron (BSE) images were recorded on a scanning electron micro-scope (SEM with a Philips XL40®) operated at 25 kV.

Additionally, the samples were characterized with a Bruker D8 advance® diffractometer (Cu K_α radiation), using a range of 10° - 120° with 0.009 steps. The procedure was later also conducted on re-solidified material to see a possible effect from melting.

The third method used to see effects on the surface was Raman spectroscopy. Raman spectra were measured with a Jobin - Yvon® T64000 spectrometer used in the single spectrograph configuration. The excitation source was a Coherent® cw laser (Ar^+ or Kr^+) radiating at wavelengths of 488 nm, 514.5 nm, 647 nm, and 752 nm with a nominal power up to several 100 mW at the exit of the cavity. The power impinging on the sample surface is lower by a factor 10 approximately and is chosen at each measurement in order to optimise the signal / noise ratio (by minimising the material fluorescence) and reducing undesirable oxidation / burning effects on the sample surface. Spectra are measured in a confocal microscope with a 50x magnification and long focal distance (about 1 cm). This feature gives a good signal / noise ratio independently of the surface shape, with a spatial resolution of 2 x 2 μm on the sample surface. The spectrograph angle is calibrated with the T_{2g} excitation of a silicon single crystal, set at 520.5 cm^{-1}.

6.3. RESULTS OF THE MELTING EXPERIMENTS

6.3.1. MIXED URANIUM-THORIUM DIOXIDE

Fig. 6.2 is an example of the recorded thermograms during the heating and cooling cycles. A TOX 40 specimen is, as described before, heated up to a temperature of about 1500 K in an Ar atmosphere and then brought to melting with pulses of different duration. After the laser pulse the sample cools by radiation conduction to the environment. This cooling process is interrupted by the release of latent heat during solidification of the molten pool and results in a short stabilisation of temperature. After 3
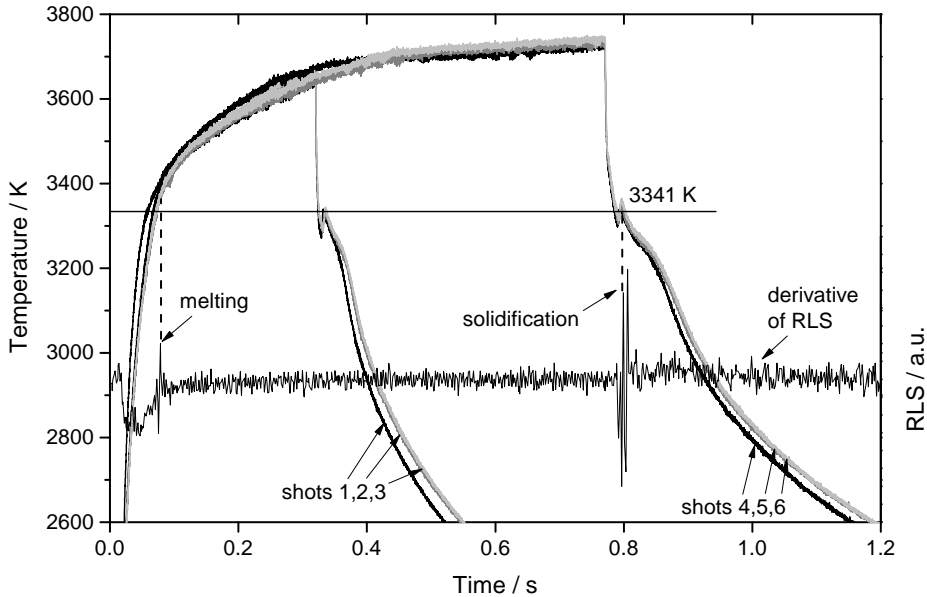
Figure 6.2: Thermograms recorded on a single TOX 40 (U$_{0.60}$Th$_{0.40}$)O$_2$ sample over 2 successive laser heating cycles. In each cycle the sample surface was hit by three high-power laser pulses (starting at 0 s) separated by dwelling periods of several seconds during which it was kept at an intermediate temperature around 1500 K in order to minimise thermal shocks. The solidification temperature of TOX 40 at 3341 K is suggested by the horizontal line. The reflected-light-signal (RLS) of shot 4 is shown below the corresponding thermogram indicating melting at about 0.08 s and 3370 K and solidification at 3341 K and 0.8 s.

high power pulses the sample is let cool to room temperature and another set of 3 shots with longer duration are used to melt the sample front side. In Fig. 6.2 thermograms of the pulses with the same length are overlapped. Differences in the heating rate are mostly attributed to crack formation in the sample disk and therefore changes in the thermal conduction in the sample. The melting process heals some cracks so that the cooling curves are repeatable over successive shots with different lengths. This implies that the samples are stable for numerous heating cycles and segregation effects, due to non-congruent vaporisation and melting, do not influence the solidification temperature in successive shots.

From these thermograms the solidification temperature is deduced at the cooling stage at the peak of the thermal arrest. An ideal flat arrest was not observed at constant temperature, since the molten surface solidifies very quickly and builds a crust upon the molten material in only a few milliseconds [19]. Therefore the thermograms can be interpreted as follows: After turning off the high power pulse, the molten surface reaches a slight undercooling until a crust of re-solidified material starts to cover the melt. During this solidification the latent heat, released during the crust formation, serves as a power source and raises the temperature on the surface. The temperature reaches a local maximum, while the surface solidifies entirely and a trapped molten pool is left inside the solid material. The re-solidification of the enclosed melt is continuous and releases heat

to the surrounding material, up to the sample surface. Therefore the cooling process at the surface is slowed down until the melt in the inside has solidified at the last inflection.

The reflected blue-light-laser (RLS) helps to identify this solidification, as well as the melting process. In Fig. 6.2 the 1st derivative of the RLS of the first shot (black) is shown in blue. One sees clear changes in the signal at the end of the laser pulse (end of heating) and right afterwards at the same time as the local temperature maximum at the thermal arrest. Also on the heating side one can identify a weaker change, also described in earlier work [14, 17, 25, 28], at the same time as the sample surface reaches the melting temperature.
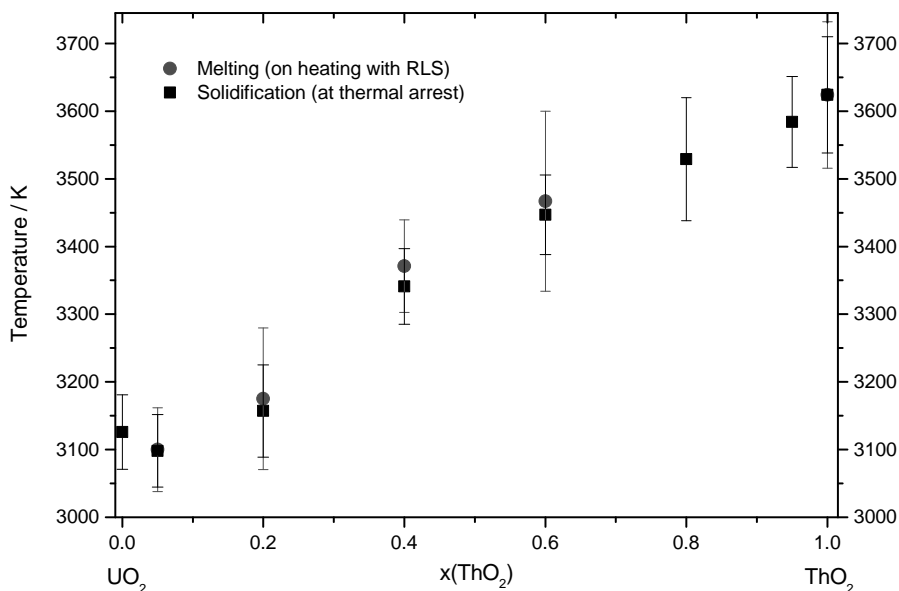

Figure 6.3: The melting / solidification temperatures observed in the present work with help of RLS and thermal arrest analyses on different TOX samples. Vertical uncertainty bands combine the intrinsic instrumental uncertainty (pyrometer calibration, sample emissivity, transmittance of the optical system) with the experimental data spread.

Fig. 6.3 and Tab. 6.1 summarise the melting / solidification points observed with the different (U, Th)O_2 compositions investigated in this work. Within the experimental uncertainty the temperature remain the same for the melting and solidification, which confirms that segregation effects during the experiments, as described before, seem to have a minor influence. One can also observe that the (U, Th)O_2 pseudo binary system seems to have a minimum melting/solidification point around 5 mol % ThO_2.

6.3.2. THORIUM DIOXIDE

Melting experiments with pure ThO_2 were performed with the current approach in air, showing a melting temperature of 3624 K ± 86 K. This is in agreement, within the reported uncertainties, with the established value in literature (3651 K ± 17 K) [15]. Tests in different atmospheres (air and argon) showed colour changes as described by Ronchi

Composition	NSE	No. of shots	Melting temperature / K	Solidification temperature / K
UO$_2$	0.830	-	-	3126 K ± 55 K [19]
TOX 5	0.832	9	3100 K ± 62 K	3098 K ± 54 K
TOX 20	0.838	11	3175 K ± 105 K	3157 K ± 69 K
TOX 40	0.846	21	3371 K ± 68 K	3341 K ± 53 K
TOX 60	0.854	9	3467 K ± 125 K	3447 K ± 59 K
TOX 80	0.862	4	n.d.	3529 K ± 91 K
TOX 95	0.868	4	n.d.	3584 K ± 67 K
ThO$_2$	0.870	11	3624 K ± 108 K	3624 K ± 86 K

Table 6.1: Normal spectral emittance (NSE), melting temperature detected by RLS and solidification points observed by thermal arrest analysis in this work on mixed (U, Th)O$_2$. (*Note:* n.d. - not detected)

and Hiernaut [15]. While the melted material surface stayed white in experiments in air, in argon the sample tended to become black after several shots. Preliminary thermo-gravimetry tests showed a hypostoichiometric change of the black material, confirming the existence of a link between oxygen losses and change in colour of the specimen of a more metallic sample as seen also before on calcium oxide [31]. However, the temperature measured in the tests with Ar-atmosphere did not show a statistically significant difference, as one can expect from calculated thermograms [22].

6.4. Discussion

6.4.1. Microscopy
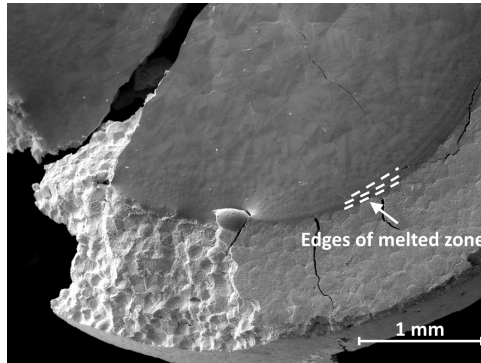
Figure 6.4: Secondary electron image of a broken TOX 60 sample, with defined re-solidified zones from different successive shots.

The samples were analysed by secondary-electron-microscopy at different magnifications. A typical microscope image (Fig. 6.4) shows the surface of a TOX 60 sample after the laser shots. One can see the edges of the melted and re-solidified zone of different successive shots. The EDX analysis showed no change of composition along the surface from the centre to the outside within the uncertainties of EDX. There is also no

difference compared to the not melted material surrounding the re-solidified zone. In all analysed compositions there are no evident traces of segregation. The ratios U/Th in the re-solidified areas remain very close to the not melted one.

Since the EDX analysis has relatively large uncertainties ($\pm$ 10 % in composition), further investigations were performed with Raman spectroscopy and powder X-ray diffraction analysis to confirm the absence of segregation effects.

6.4.2. RAMAN SPECTROSCOPY

Main purpose of the current Raman spectroscopy analysis was the detection of possible segregation/oxidation effects in the mixed oxide samples following the laser heating cycles beyond melting. Some Raman spectra recorded in this work with a 514 nm laser excitation source on mixed uranium-thorium dioxides are presented in Fig. 6.5 and 6.7.
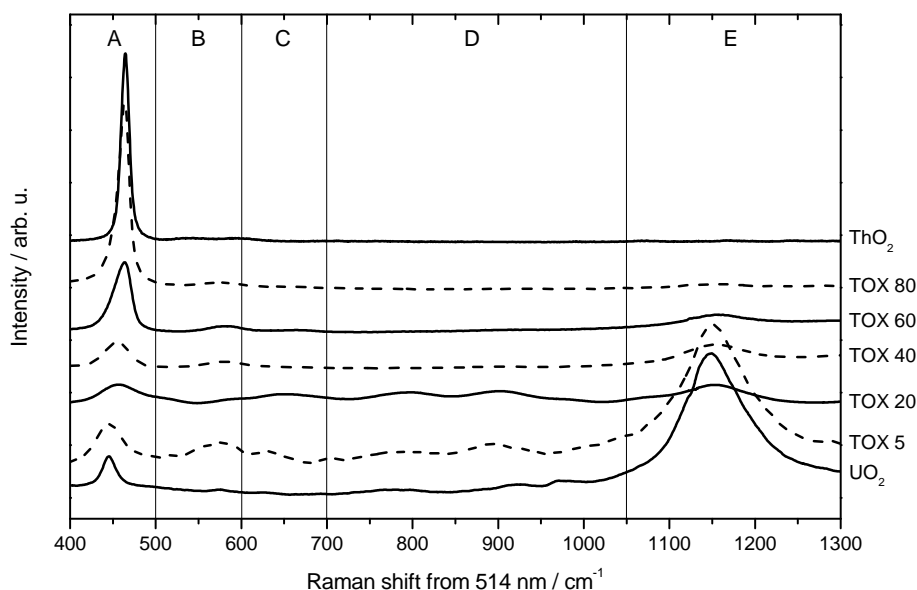

Figure 6.5: Raman spectra comparison of not melted samples with different ThO_2 content recorded with a 514 nm excitation laser.

The fluorite-like structures studied in this research (fcc, $Fm\overline{3}m$) have only one (triply degenerate) Raman active vibration (T_{2g}), which is taken as a reference peak for our investigation. In stoichiometric urania the peak is found at 445 cm^{-1} [32], in thoria at 465 cm^{-1} relative to the excitation wavelength [32]. This vibration is identified as zone "A" in the spectra reported in Fig. 6.5. Zone "B" contains a rather weak peak around 575 cm^{-1}, which has been attributed to a longitudinal optical (LO) phonon [33]. Its Raman activity is linked to the presence of oxygen vacancies in the fcc fluorite lattice [34]. This peak is visible rather poorly in all compositions. Zone "C" contains, essentially in TOX 5 and TOX 20, a weak peak around 630 cm^{-1}. This feature has been assigned to the formation of oxygen interstitial clusters, resulting in the separation of a M_4O_9 super-

symmetry within the fcc lattice [35]. The rather irregular features observable in zone "D" of the Raman spectra of Pure UO$_2$, TOX 5 and TOX 20, correspond to vibrations of species containing uranyl groups. These species (U$_3$O$_7$, U$_3$O$_8$, UO$_3$ [36]) can be easily formed on the sample surface in contact with air, especially under the irradiation of the laser used as excitation source for the Raman measurements. Obviously, the addition of ThO$_2$ (a chemically very stable compound) to UO$_2$ has a stabilising effect, with respect to the formation of these structures on the sample surface in contact with the air, only for compositions x(ThO$_2$) > 0.2 approximately. Finally, the presence of a broad and intense peak around 1150 cm^{-1} is clearly observable in zone "E" of the spectra measured in samples with x(ThO$_2$) < 0.80. This peak has been demonstrated to be an overtone of the 575 cm^{-1} LO phonon [33, 37]. Its intensity obviously changes with composition. This peak was shown to be Raman resonant in uranium dioxide [33, 37], but not in thorium dioxide. This explains its composition dependent behaviour in the current mixed oxides.
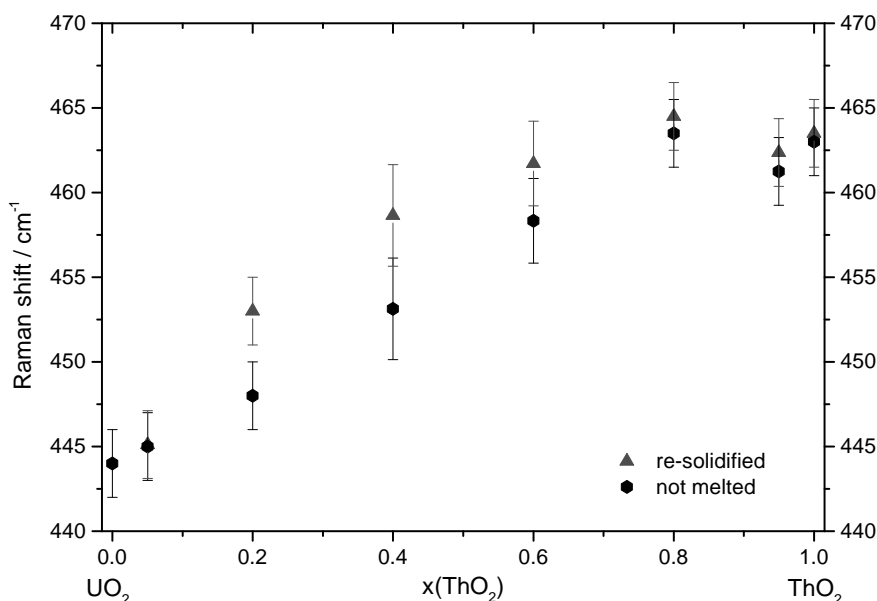

Figure 6.6: Dependence of the Raman T$_{2g}$ position on molar fraction of ThO$_2$.

A plot of the dependence of the T$_{2g}$ peak position with the ThO$_2$ content is shown in Fig. 6.6 and in Tab. 6.2. The average of several measurements on not melted and re-solidified material at the surface is shown with a combined uncertainty with a 2-k coverage factor resulting in a total uncertainty of 2 cm^{-1} to 3 cm^{-1} (with a spectral uncertainty of ± 1 cm^{-1}). The T$_{2g}$ Raman shift clearly tends from urania to the thoria value following the amount of thoria in the material. This peak tends also to sharpen at increasing ThO$_2$ content, probably due to a decrease in oxygen defect concentration. The measurements were conducted on different spots at the surface showing no consistent (in-/decrease) and systematic (centre to outside) difference to each other on the same surface. This homogeneity of the surface could originate from the very fast formation of

the crust combined with slow diffusion in the solid.

No full analytical relation between the composition and the T_{2g} peak Raman shift has been determined for this system. The T_{2g} peak wavenumber increases with an approximately linear trend only from pure UO_2 to 80 mol % ThO_2 for the not melted material. For higher thoria contents, this Raman mode keeps very similar to the one of pure ThO_2, both in peak position and intensity. This behaviour is probably attributable to the resonant nature of the T_{2g} Raman active mode in thorium dioxide, and its much higher scattering efficiency compared to UO_2 [38, 39]. One can see that the re-solidified material has a consistently higher T_{2g} peak position than the not melted material, though very little around the end-members (UO_2 and ThO_2). An increase in the Raman shift would indicate a composition shift towards ThO_2 on the surface of the re-solidified material, compared to the not melted material for the intermediate compositions (with 20, 40 and 60 mol % ThO_2).

There are different effects which might play a role in the current observations with Raman spectroscopy: (i) high temperature lattice disorder, as Frenkel pairs in the oxygen sublattice [40], quenched to room temperature, could have an increasing effect on the peak shifts of the re-solidified material, (ii) changes of the material fractions as a result of different surface tensions in the melt or (iii) segregation can occur during the rapid heating/cooling cycles across the non-congruent melting transition, resulting in compositional shifts in the quenched solid, also (iv), the T_{2g} Raman scattering efficiency of ThO_2 is higher compared to UO_2 [38, 39].
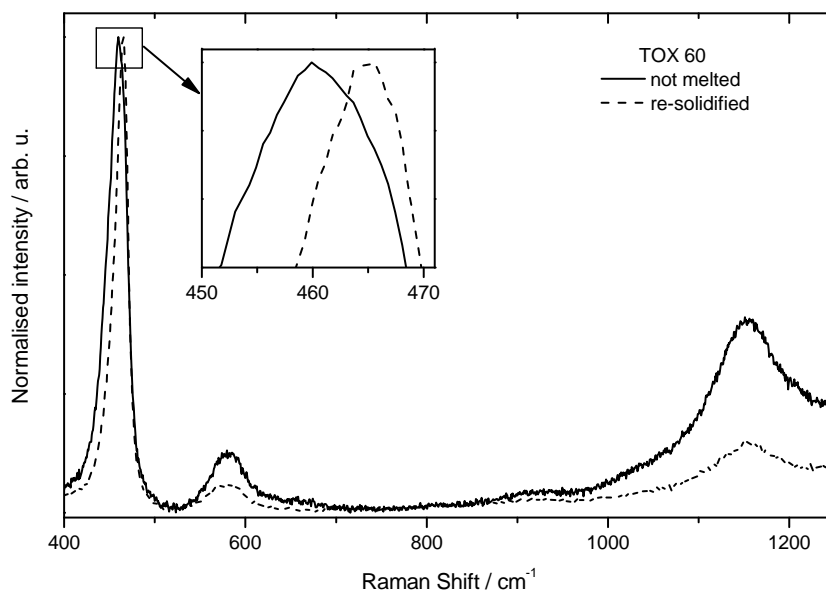

Figure 6.7: Raman spectra comparison of a re-solidied and not melted TOX 60 sample recorded with a 514 nm excitation laser.

In order to detect possible effects of high-temperature surface oxidation or oxygen defect formation Fig. 6.7 shows the comparison between a broader Raman spectrum

Composition	Raman shift / cm^{-1}		Lattice parameter / Å	
	not melted	re-solidified	not melted	re-solidified
UO$_2$	444	-	5.4708	-
TOX 5	445.1	445.1	5.4775	5.4780
TOX 20	448.1	453.0	5.4985	5.5031
TOX 40	452.9	458.6	5.5243	5.5245
TOX 60	458.3	461.7	5.5501	5.5513
TOX 80	463.5	464.5	5.5735	5.5747
TOX 95	461.3	462.4	5.5898	5.5900
ThO$_2$	463.0	463.5	5.5971	5.5972

Table 6.2: The evolution of T$_{2g}$ positions and lattice parameter with ThO$_2$ content

recorded with a 514 nm excitation laser on a re-solidified and a not melted TOX 60 sample. The most appreciable difference between the two spectra is the slight shift in the T$_{2g}$ peak (see inset), corresponding to the difference in its position reported in Fig. 6.6. As mentioned above, such difference can be related to both a local enrichment in ThO$_2$, probably due to segregation during the melting/freezing process, and the formation / annihilation of oxygen defects. However, the slight differences in the spectral zones C and D of Fig. 6.5, between 600 and 950 cm^{-1}, seem more reasonably attributable to variations in the background noise than to any clear formation or annihilation of oxygen defects during the thermal cycles beyond melting. It can be concluded that no obvious oxidation effects on the re-solidified surface could be detected by the current Raman analysis.

Instead, this analysis revealed the occurrence of some segregation leading to non-negligible ThO$_2$ enrichment, with respect to the initial sample composition, in resolidified samples with intermediate values of x(ThO$_2$). The lower relative intensities of the Raman peaks at 575 cm^{-1} and 1150 cm^{-1} in the re-solidified sample (Fig. 6.6) confirm the same trend, when compared with the spectra displayed in Fig. 6.5 for the various UO$_2$-ThO$_2$ compositions. Such segregation, occurring during the fast heating/cooling cycles, can be limited to the very external part of the sample surface. This part has been shown to be the first to solidify from the liquid forming a thin crust in contact with the external atmosphere [19]. It is the most likely to display segregation phenomena, due to slow diffusion in the solid [14, 19]. However, its exact thickness has not been determined.

The penetration depth for the Raman analysis in this work can be conservatively assumed with the Lamber-Beer law to be 0.5 μm to a few μm (depending on the ThO$_2$ content)[41, 42], compared to melted depth of at least 20 μm [17]. Therefore the analysis is certainly limited to a superficial layer considerably thinner than the whole melted pool and to a thinner layer than an EDX analysis, which has an emission depth of about 5 μm. It is not obvious to conclude whether the Raman-analysed part is smaller or bigger than the superficial crust initially formed upon solidification. Independently, it is plausible to assume that segregation effects observed by Raman spectroscopy in melted samples with intermediate x(ThO$_2$) values can be limited to an external layer of the refrozen pool. There, a composition enriched in ThO$_2$ can be formed and quenched at the

beginning of the fast solidification process, according to the UO_2-ThO_2 solidus-liquidus phase boundaries.

6.4.3. POWDER X-RAY DIFFRACTION

In order to investigate the occurrence of similar segregation and additional oxidation phenomena in the whole mass of not melted and re-solidified material, powder X-ray analysis was performed.
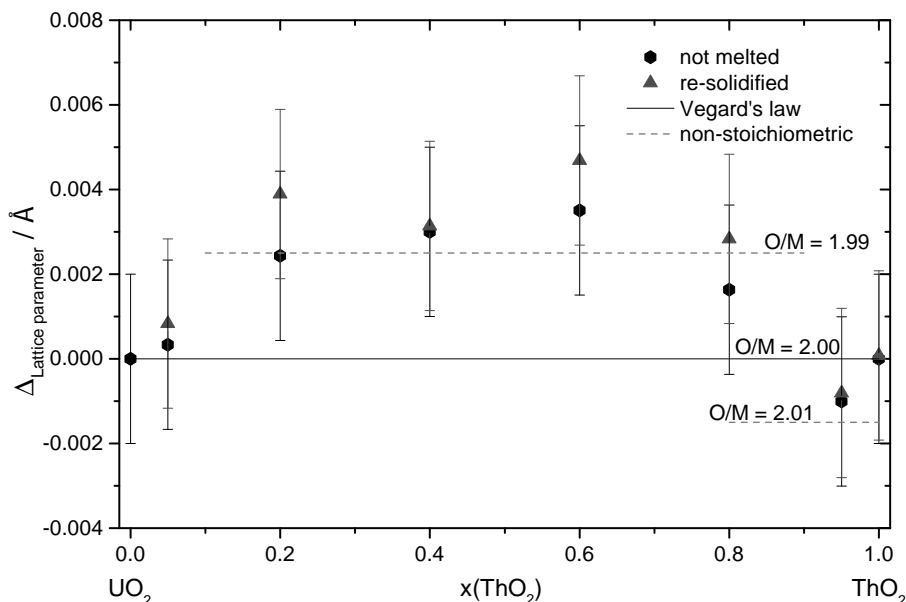

Figure 6.8: Difference between lattice parameters of the samples (± 0.002 Å) and Vegard's law interpolation between the endmembers in dependence of the ThO_2 content. The black line represents Vegard's law between the stoichiometric UO_2 and ThO_2. The dotted lines suggest non-stoichiometric changes from hyperstoichiometric studies on $(U, Th)O_2$ [43] and hypostoichiometric studies on $(U, Pu)O_2$ [44].

Tab. 6.2 shows the measured lattice parameters obtained by powder X-ray diffraction (PXRD), while Fig. 6.8 shows the difference of the lattice parameter to the interpolation (Vegard's law) between the pure components ThO_2 and UO_2. One can easily see that the re-solidified and not melted material shows nearly identical lattice parameters. As well, no other (higher oxide) phases as the fcc $Fm\bar{3}m$ phase of the solid solution of $(U, Th)O_2$ - even on different samples in the uranium rich part - were seen in the diffraction patterns. The lattice parameter agree well with the parameters of Cohen and Berman [43] or Hubert et al. [45], except a slight deviation in Cohen and Berman's work from Vegard's law, showing a minimum at 2 mol.% ThO_2. A small phase separation was seen for the re-solidified TOX 40, with a higher lattice parameter (5.5489 Å; +0.0288 Å away form Vegard's law), which is probably formed while cooling. Such segregation is explained in the next section in more detail with the help of the phase diagram.

The slight deviation to Vegard's law here can be attributed to uncertainty (of approximately 2%) in the initial composition or a slight change of the O/M ratio, although it

is not possible to distinguish between these two effects only by the lattice parameter. Compared to the results from mixed (U, Pu)O$_2$ [44] or from hyperstoichiometric studies on (U, Th)O$_2$ [43], the change in O/M can be assumed to be small in this work. There is no study so far to the knowledge of the authors, which addresses the reduction of (U, Th)O$_2$. It is not surprising that due to the low oxygen potential of ThO$_2$ shifts in the lattice parameter caused by stoichiometric changes would be small. In some compositions an increase of the lattice parameters in the re-solidified material suggests a shift towards ThO$_2$, but is still within the uncertainty range and relatively small compared to the shifts indicated by Raman spectroscopy in this work. One has also to bear in mind that these measurements were done at room temperature and even though the samples are cooled down from high temperature very quickly and structures might be quenched, changes cannot be ruled out during cooling. Also, any local differences within the re-solidified zone are not seen by PXRD and are maybe averaged, especially since in the analysis no distinction of material close to the surface and "deeper" material can be made.

Finally, PXRD analysis confirms, with the before mentioned constraints, that the shift observed in the T$_{2g}$ Raman peak of samples with intermediate x(ThO$_2$) values are probably attributable to UO$_2$-ThO$_2$ segregation limited to a very shallow region starting from the most external crust of the melted and re-solidified surface. The remaining re-solidified bulk maintains, within the experimental uncertainties, the initial composition even after the laser heating cycles beyond melting.

6.4.4. MELTING TEMPERATURE RESULTS

The melting point for ThO$_2$ is here measured to be 27 K lower than formerly measured and published by Ronchi and Hiernaut [15]. With the considered uncertainties, the difference is largely covered. In fact, by reinterpreting the solidification temperatures of Ronchi and Hiernaut on the basis of their published thermogram in the same way as thermograms in this work have been interpreted, one reaches a temperature of 3639 K $\pm$ 42 K (only the data spread with a 2-k coverage factor is considered), which is even closer to our result of 3624 K. Other effects as the reported pre-melting transition were not seen in the current study. Generally, small enthalpy changes are not expected to be seen with the experimental approach in this work, due to the different sample geometry and heat loss balance with respect to Ronchi and Hiernaut's work.

The interpretation of the thermograms has been already discussed in a previous work with the help of Phase-Field simulations [19], which show that the complex shape of the thermal arrest comes from rapid solidification of the surface rather than a solidus / liquidus transition in thermodynamic equilibrium. Compared to the diffusion rates of actinide oxides [44] the solidification process in these experiments is very fast, so that an exact identification of the liquidus (first appearance of solid in the molten zone) and solidus (solidification of the last molten material) temperatures becomes very difficult [46]. With the help of the reflected light signal, the melting transition could be identified in some measurements and was found to be close to the the solidification temperature as one can see in Fig. 6.3 and Fig. 6.9. The differences are still within the uncertainty bands. The most likely explanation for this melting/solidification difference is parasite reflections of the heating laser into the pyrometer.

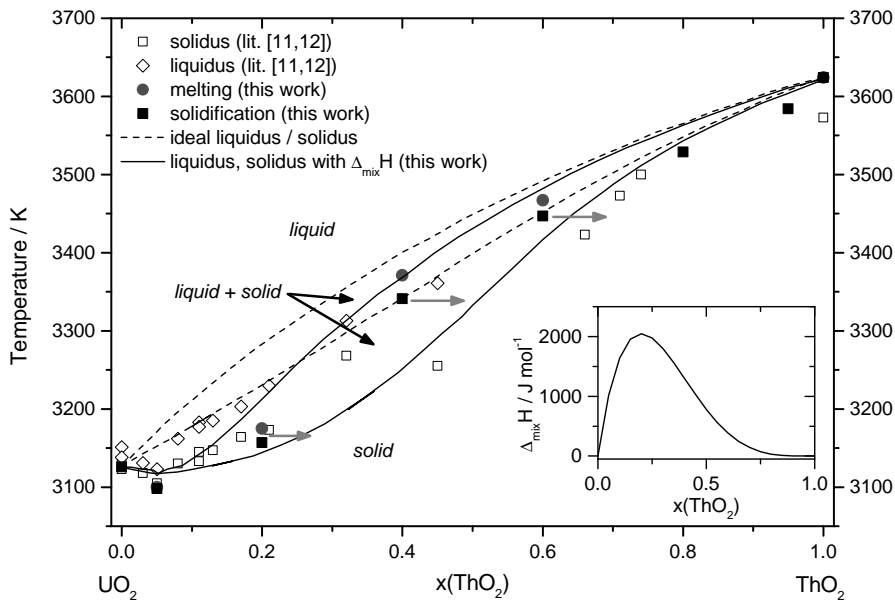The UO$_2$ - ThO$_2$ system is an isomorphous binary phase diagram. In this kind of sys-

Figure 6.9: High temperature phase diagram of the pseudo-binary UO$_2$ - ThO$_2$ system. Results of this work are shown together with the ideal solution binary solidus and liquidus (solid lines) and data from earlier measurements [12, 13]. With grey arrows a suggested shift of the obtained melting/solidification temperatures is shown qualitatively. The solid solidus and liquidus lines take into account deviations from the ideal solution behaviour. They have been calculated by considering a mixing enthalpy in the solid solution, whose values reported in the inset have been optimised in order to best fit the current experimental data with a polynomial formalism.

tem only one solid phase exists at the equilibrium and the two endmembers exhibit a complete solid solubility. If one assumes ideal solid and liquid solutions for every composition, solidus and liquidus can be calculated solely based on the thermodynamic data of the two end members recently reviewed by Konings et al. [47] and considering only ideal configurational entropy contributions. The resulting solidus and liquidus plots are shown in Fig. 6.9 together with the current and literature experimental data.

The minimum melting temperature found in this work for 5 mol. % ThO$_2$ contradicts a fully ideal solution in the domain of melting (as already graphically assumed by Belle and Berman [6]). The work of Lambertson et al. [12] showed a total miscibility of the components in all proportions. Latta et al. [13] focused their attention on the region below 20 mol. % ThO$_2$, for which a minimum at 5 mol. % ThO$_2$ was also observed. The melting temperatures in that study are similar to this work in the uranium rich part, but differ in the intermediate compositions. In the thorium rich part of the phase diagram data are more rare, so that a direct comparison of each composition is not possible. This deviation from ideal behaviour close to UO$_2$, the chemically less stable oxide, emphasises a stabilizing effect of ThO$_2$ in mixed actinide oxides [43]. The reproducibility by laser containerless heating of older data with a high content of thoria confirms that the oxygen potential is indeed a crucial parameter determining the reactivity of these oxides

with the containment.

With the used characterisation methods, small variations between the re-solidified and the not melted material can be linked to segregation on the most external part of the freezing surface. According to the phase diagram the composition formed at the liquidus temperature upon solidification of the sample surface corresponds to the solidus point of another composition enriched in ThO$_2$. This latter surface composition is likely to be quenched to room temperature almost unchanged, due to slower mass diffusion in the solid. Therefore it is suggested to move the observed solidification points of the intermediate compositions (20, 40 and 60 mol % ThO$_2$) towards the ThO$_2$ side of the phase diagram (see Fig. 6.9), although the shift could not be exactly quantified. Thus, ideal solution behaviour can be approximated for most of the compositions.

Calphad optimisation of phase diagrams of actinide oxides suggest a non-congruent (slightly hypostoichiometric) melting for dioxides [20, 22], and oxygen potential studies of hyperstoichiometric (U, Th)O$_2$ suggested a non-ideal hyperstoichiometric system [48].

Almost ideal solid solution behaviour has been observed in most compositions in this study, especially for thorium rich compositions. The slight deviation from the ideal solution leading to a minimum melting point in the UO2-rich part can be fairly reproduced by using a polynomial formalism of the type proposed by Pelton and Thompson [49], with one adjustable parameter for describing the excess Gibbs energy ΔG^{exc} in the solid:

$$\Delta G^{exc} = x(UO_2)^4 \cdot x(ThO) \cdot A \tag{6.1}$$

A is a parameter, assumed to be temperature-independent, representing the interaction between the components in the solid solution. The exponents with which the molar fractions of urania and thoria (x(UO$_2$) and x(ThO$_2$) respectively) appear in Eq. 6.1 account for asymmetry in the model, consistently with the most relevant deviations from ideality observed in uranium-richer compositions. In this first-approach excess parameter optimization, the liquid phase is still treated as a fully ideal solution. Best fit of the experimental solidification data (considered as solidus points at compositions corrected for eventual segregation effects) was obtained for A = 25 kJ mol^{-1}. The resulting solidus and liquidus lines are also reported in Fig. 6.9 (solid curves). They do match a minimum melting point for low thoria contents. They also seem to be more consistent with the mentioned shifts induced in intermediate compositions by segregation effects during the melting/freezing process and with earlier solidus data [12, 13]. A plot of the relative solid mixing (excess) enthalpy $\Delta_{mix}H$ vs. composition is reported in the inset of Fig. 6.9. These results are obtained in a first-approximation approach, and should therefore be considered as purely indicative of general trends. Nonetheless, they do give a rough quantification of deviations from ideal solution behaviour concentrated in urania-rich compositions. Such deviations can be certainly related to the formation of lattice defects for high UO$_2$ contents. In these compositions, the formation of both oxygen interstitials and vacancies is very likely due to the possibility for uranium to assume, in the oxide, the valence states +3, +4, +5 and +6, whereas thorium is stable only in the form Th^{4+} [44]. This is also in line with the current Raman analysis, which showed that further oxidised structures of UO$_2$ are more easily formed on the surface of samples with nominally

5 and 20 mol % ThO$_2$, i.e. for the lowest ThO$_2$ contents investigated here.

Interestingly, a small addition of ThO$_2$ to UO$_2$ seems to still permit the formation of these structures rather than hindering it. The uranium rich part of the system can therefore be fully assessed only as a ternary U-Th-O. This behaviour can also be described, in a first approximation, as a binary non-stoichiometric phase diagram as shown in [19]. In the light of such behaviour, it is easier to understand the anomalous melting point deviation from the ideal solidus and liquidus lines in mixed uranium-thorium dioxides with low thorium content.

6.5. Conclusions

F OLLOWING novel results in disagreement to earlier data found for pure and mixed actinide oxides with containerless laser heating, this study re-analysed ThO$_2$ and the mixed system (U, Th)O$_2$. Several conclusions can be drawn from these experiments:

- With respect to the high temperature interaction between sample and containment, the reproducibility of earlier results seems to be better in compounds like ThO$_2$, with a low oxygen potential. Earlier results were reproduced within the uncertainty bands, confirming a minimum melting point in the UO$_2$ - ThO$_2$ system around 5 mol % ThO$_2$ and 3098 K.

- The (U, Th)O$_2$ system should be described, in the uranium rich part, rather as a ternary U-Th-O system than a purely pseudo-binary UO$_2$ - ThO$_2$. The performed material analyses (SEM, Raman spectroscopy, XRD) support this interpretation, by showing the formation, on the very surface of the re-solidified sample, of species with a higher oxidation state only for thorium dioxide concentrations lower than approximately 20 mol % ThO$_2$. More effects at high temperature, as e.g. defect formation and O/M variations, may play a further role, but could not be identified with the current analysis methods at room temperature.

- Ideal solution behaviour can be reasonably hypothesised around melting for intermediate and ThO$_2$-rich compositions. Based on material characterisation results, segregation effects cannot be excluded on the observed melting / solidification temperatures of intermediate compositions (20, 40 and 60 mol % ThO$_2$). These compositions show by bulk and thermal analysis only minor differences between re-solidified and not melted material. Surface analysis (Raman spectroscopy) reveals possible composition shifts, difficult to quantify. These shifts are probably limited to the very surface of the re-solidified sample and are in line with a quenching solidification process in the phase diagram.

The current results help to understand the high temperature behaviour of a refractory material in terms of basic research and also in terms of safety and security of a possible nuclear fuel in accidental or operating conditions.

REFERENCES

[1] R. Böhler, A. Quaini, L. Capriotti, P. Çakır, O. Beneš, K. Boboridis, A. Guiot, L. Luzzi, R. Konings, and D. Manara, *The solidification behaviour of the UO_2-ThO_2 system in a laser heating study,* J. Alloys Compd. **616**, 5 (2014).

[2] P. R. Hania and F. C. Klaassen, *3.04 - Thorium Oxide Fuel,* in *Compr. Nucl. Mater.,* edited by R. J. M. Konings (Elsevier, Oxford, 2012) pp. 87–108.

[3] S. F. Ashley, G. T. Parks, W. J. Nuttall, C. Boxall, and R. W. Grimes, *Nuclear energy: Thorium fuel has risks,* Nature **492**, 31 (2012).

[4] W. E. Lee, M. Gilbert, S. T. Murphy, and R. W. Grimes, *Opportunities for Advanced Ceramics and Composites in the Nuclear Sector,* J. Am. Ceram. Soc. **96**, 2005 (2013).

[5] C. Lombardi, L. Luzzi, E. Padovani, and F. Vettraino, *Thoria and inert matrix fuels for a sustainable nuclear power,* Prog. Nucl. Energy **50**, 944 (2008).

[6] J. Belle and R. Berman, *Thorium dioxide: properties and nuclear applications,* Tech. Rep. (USDOE Office of Nuclear Energy, Science and Technology (NE), 1984).

[7] J. Herring, P. E. MacDonald, K. D. Weaver, and C. Kullberg, *Low cost, proliferation resistant, uranium-thorium dioxide fuels for light water reactors,* Nucl. Eng. Des. **203**, 65 (2001).

[8] M. Basu (Ali), R. Mishra, S. Bharadwaj, and D. Das, *Thermodynamic and transport properties of thoria - urania fuel of Advanced Heavy Water Reactor,* J. Nucl. Mater. **403**, 204 (2010).

[9] Y. Lu, Y. Yang, and P. Zhang, *Thermodynamic properties and structural stability of thorium dioxide.* J. Phys. Condens. Matter **24**, 225801 (2012).

[10] O. İpek, *Analysis of temperature distribution, burn-up and breeding parameters in nuclear fuel rod in fusion-fission reactor system fueled with mixed ThO_2-UO_2 fuel,* Int. J. Energy Res. **35**, 112 (2011).

[11] C. Lombardi, L. Luzzi, E. Padovani, and F. Vettraino, *Inert matrix and thoria fuels for plutonium elimination,* Prog. Nucl. Energy **38**, 395 (2001).

[12] W. A. Lambertson, M. H. Mueller, and F. H. Gunzel, *Uranium Oxide Phase Equilibrium Systems: IV, UO_2-ThO_2,* J. Am. Ceram. Soc. **36**, 397 (1953).

[13] R. Latta, E. Duderstadt, and R. Fryxell, *Solidus and liquidus temperatures in the UO_2-ThO_2 system,* J. Nucl. Mater. **35**, 347 (1970).

[14] D. Manara, C. Ronchi, M. Sheindlin, M. Lewis, and M. Brykin, *Melting of stoichiometric and hyperstoichiometric uranium dioxide,* J. Nucl. Mater. **342**, 148 (2005).

[15] C. Ronchi and J.-P. Hiernaut, *Experimental measurement of pre-melting and melting of thorium dioxide,* J. Alloys Compd. **240**, 179 (1996).

6

[16] F. De Bruycker, K. Boboridis, D. Manara, P. Pöml, M. Rini, and R. J. Konings, *Reassessing the melting temperature of PuO$_2$*, Mater. Today **13**, 52 (2010).

[17] R. Böhler, M. J. Welland, F. D. Bruycker, K. Boboridis, A. Janssen, R. Eloirdi, R. J. M. Konings, and D. Manara, *Revisiting the melting temperature of NpO$_2$ and the challenges associated with high temperature actinide compound measurements*, J. Appl. Phys. **111**, 113501 (2012).

[18] F. De Bruycker, K. Boboridis, R. Konings, M. Rini, R. Eloirdi, C. Guéneau, N. Dupin, and D. Manara, *On the melting behaviour of uranium/plutonium mixed dioxides with high-Pu content: A laser heating study*, J. Nucl. Mater. **419**, 186 (2011).

[19] R. Böhler, M. Welland, D. Prieur, P. Çakır, T. Vitova, T. Pruessmann, I. Pidchenko, C. Hennig, C. Guéneau, R. Konings, and D. Manara, *Recent advances in the study of the UO$_2$-PuO$_2$ phase diagram at high temperatures*, J. Nucl. Mater. **448**, 330 (2014).

[20] C. Guéneau, N. Dupin, B. Sundman, C. Martial, J.-C. Dumas, S. Gossé, S. Chatain, F. D. Bruycker, D. Manara, and R. J. Konings, *Thermodynamic modelling of advanced oxide and carbide nuclear fuels: Description of the U-Pu-O-C systems*, J. Nucl. Mater. **419**, 145 (2011).

[21] D. Manara, R. Böhler, K. Boboridis, L. Capriotti, A. Quaini, L. Luzzi, F. De Bruycker, C. Guéneau, N. Dupin, and R. Konings, *The Melting Behaviour of Oxide Nuclear Fuels: Effects of the Oxygen Potential Studied by Laser Heating*, Procedia Chem. **7**, 505 (2012).

[22] H. Kinoshita, D. Setoyama, Y. Saito, M. Hirota, K. Kurosaki, M. Uno, and S. Yamanaka, *Thermodynamic modelling and phase stability assessment of MO$_{2-x}$ oxides with a fluorite structure*, J. Chem. Thermodyn. **35**, 719 (2003).

[23] C. Jégou, R. Caraballo, S. Peuget, D. Roudil, L. Desgranges, and M. Magnin, *Raman spectroscopy characterization of actinide oxides (U$_{1-y}$Pu$_y$)O$_2$: Resistance to oxidation by the laser beam and examination of defects*, J. Nucl. Mater. **405**, 235 (2010).

[24] M. J. Sarsfield, R. J. Taylor, C. Puxley, and H. M. Steele, *Raman spectroscopy of plutonium dioxide and related materials*, J. Nucl. Mater. **427**, 333 (2012).

[25] D. Manara, M. Sheindlin, W. Heinz, and C. Ronchi, *New techniques for high-temperature melting measurements in volatile refractory materials via laser surface heating*, Rev. Sci. Instrum. **79**, 113901 (2008).

[26] H. Preston-Thomas, *The International Temperature Scale of 1990 (ITS-90)*, Metrologia **27**, 3 (1990).

[27] R. E. Bedford, G. Bonnier, H. Maas, and F. Pavese, *Recommended values of temperature on the International Temperature Scale of 1990 for a selected set of secondary reference points*, Metrologia **33**, 133 (1996).

6

[28] F. De Bruycker, K. Boboridis, P. Pöml, R. Eloirdi, R. Konings, and D. Manara, *The melting behaviour of plutonium dioxide: A laser-heating study,* J. Nucl. Mater. **416**, 166 (2011).

[29] M. Bober, J. Singer, and K. Wagner, *Spectral Reflectivity and Emissivity Measurements of Solid and Liquid UO_2 at 458, 514.5 and 647 nm as a Function of Polarization and Angle of Incidence*, Tech. Rep. September (Kernforschungszentrum Karlsruhe - Institut für Neutronenphysik und Reaktortechnik, 1980).

[30] H. Karow and M. Bober, *Experimental investigations into the spectral relectivities and emissivities of liquid UO_2 , UC, ThO_2 , and Nd_2O_3,* in *Thermodyn. Nucl. Mater. 1979, Vol. 1* (IAEA, 1980) pp. 155–169.

[31] D. Manara, R. Böhler, L. Capriotti, A. Quaini, Z. Bao, K. Boboridis, L. Luzzi, A. Janssen, P. Pöml, R. Eloirdi, and R. Konings, *On the melting behaviour of calcium monoxide under different atmospheres: A laser heating study,* J. Eur. Ceram. Soc. **34**, 1623 (2014).

[32] G. Begun, R. Haire, W. Wilmarth, and J. Peterson, *Raman spectra of some actinide dioxides and of EuF_2,* J. Less Common Met. **162**, 129 (1990).

[33] T. Livneh and E. Sterer, *Effect of pressure on the resonant multiphonon Raman scattering in UO_2,* Phys. Rev. B **73**, 085118 (2006).

[34] L. Desgranges, G. Guimbretière, P. Simon, C. Jegou, and R. Caraballo, *A possible new mechanism for defect formation in irradiated UO_2,* Nucl. Instruments Methods Phys. Res. Sect. B Beam Interact. with Mater. Atoms **315**, 169 (2013).

[35] L. Desgranges, G. Baldinozzi, P. Simon, G. Guimbretière, and A. Canizares, *Raman spectrum of U_4O_9: a new interpretation of damage lines in UO_2,* J. Raman Spectrosc. **43**, 455 (2012).

[36] F. Pointurier and O. Marie, *Identification of the chemical forms of uranium compounds in micrometer-size particles by means of micro-Raman spectrometry and scanning electron microscope,* Spectrochim. Acta Part B At. Spectrosc. **65**, 797 (2010).

[37] R. Rao, R. K. Bhagat, N. P. Salke, and A. Kumar, *Raman spectroscopic investigation of thorium dioxide-uranium dioxide (ThO_2 -UO_2) fuel materials.* Appl. Spectrosc. **68**, 44 (2014).

[38] V. G. Keramidas, *Raman spectra of oxides with the fluorite structure,* J. Chem. Phys. **59**, 1561 (1973).

[39] M. Ishigame and M. Kojima, *Second-Order Raman Spectra of Thorium Dioxide,* J. Phys. Soc. Japan **41**, 202 (1976).

[40] M. T. Hutchings, *High-temperature studies of UO_2 and ThO_2 using neutron scattering techniques,* J. Chem. Soc., Faraday Trans. 2 **83**, 1083 (1987).

6

[41] R. J. Ackermann, R. J. Thorn, and G. H. Winslow, *Visible and Ultraviolet Absorption Properties of Uranium Dioxide Films,* J. Opt. Soc. Am. **49**, 1107 (1959).

[42] O. Weinreich and W. Danforth, *Optical Properties of Crystalline Thoria,* Phys. Rev. **88**, 953 (1952).

[43] I. Cohen and R. Berman, *A metallographic and X-ray study of the limits of oxygen solubility in the UO_2 - ThO_2 system,* J. Nucl. Mater. **18**, 77 (1966).

[44] C. Guéneau, A. Chartier, and L. V. Brutzel, *2.02 - Thermodynamic and Thermophysical Properties of the Actinide Oxides,* in *Compr. Nucl. Mater.,* edited by R. J. Konings (Elsevier, Oxford, 2012) pp. 21–59.

[45] S. Hubert, J. Purans, G. Heisbourg, P. Moisy, and N. Dacheux, *Local structure of actinide dioxide solid solutions $Th_{1-x}U_xO_2$ and $Th_{1-x}Pu_xO_2$,* Inorg. Chem. **45**, 3887 (2006).

[46] M. J. Aziz and T. Kaplan, *Continuous growth model for interface motion during alloy solidification,* Acta Metall. **36**, 2335 (1988).

[47] R. J. M. Konings, O. Beneš, A. Kovács, D. Manara, D. Sedmidubský, L. Gorokhov, V. S. Iorish, V. Yungman, E. Shenyavskaya, and E. Osina, *The Thermodynamic Properties of the f-Elements and their Compounds. Part 2. The Lanthanide and Actinide Oxides,* J. Phys. Chem. Ref. Data **43**, 013101 (2014).

[48] M. Ugajin, *Oxygen potentials of (Th, U)O_{2+x} solid solutions,* J. Nucl. Mater. **110**, 140 (1982).

[49] A. Pelton and W. Thompson, *Phase diagrams,* Prog. Solid State Chem. **10**, 119 (1975).

6

7

HIGH TEMPERATURE PHASE TRANSITION OF MIXED PuO$_2$-ThO$_2$

Robert BÖHLER, Pelin ÇAKIR, Ondrej BENEŠ, Herwin HEIN, Rudy J.M. KONINGS, Dario MANARA

A laser heating approach combined with fast pyrometry in a thermal arrest method was used to provide new data for the melting/solidification phase transition in mixed PuO$_2$ – ThO$_2$ at high temperature. At low concentration of ThO$_2$ in PuO$_2$ a minimum in the solidification temperature in the pseudo binary PuO$_2$ – ThO$_2$ was observed. The minimum was found around a composition with 5 mol % ThO$_2$. Phase transition temperatures of other compositions are closer to an ideal solution behaviour. To detect changes in the material a complete investigation with electron microscopy, Raman spectroscopy and powder X-ray diffraction was done. Raman vibration modes were found, that are characteristic for materials containing PuO$_2$, and high temperature segregation effects during solidification were described. The results obtained in the present work are compared to other mixed actinide dioxides and compared to the ideal solution case for this system. The presented results show the importance of the high-temperature oxygen chemistry in this actinide oxide phase.

7.1. Introduction

$\mathbf{M}$ IXED actinide dioxides are a solid solution of the two dioxide end-members with a fluorite-like structure (fcc, $Fm\overline{3}m$) [2]. Thermal material properties of such systems seem to behave ideally at temperatures well below melting [2], which is shown, for example, for the $(Pu,Th)O_2$ solid solution with new heat capacity studies by Valu et al. [3]. Recent studies on the melting of mixed actinide dioxides $((U,Pu)O_2$ [4], $(U,Th)O_2$ [5]) showed on the other hand a non-ideal behaviour for the high temperature melting/solidification phase transition. Both mixed systems revealed a minimum temperature in the pseudo-binary section and question the validity of an ideal solution assumption for these systems at high temperatures. These oxides, being very sensitive to the oxygen potential, then should be better regarded as ternary systems, especially at high temperatures.

The mixture of PuO_2 with ThO_2 is interesting in this context for several reasons: (i) The melting points of the pure components are the furthest apart among the actinide dioxides, that are known to be stable under standard conditions and can be used in such a melting study. (ii) The difference in ionic radius of the actinides is the largest compared to already measured binary actinide dioxide systems. (iii) The valence state is neither for Pu nor for Th in a dry environment expected to reach 5+ in contrast to uranium-containing systems. But for a given O/M ratio, the oxygen potential of PuO_2 is higher than other MO_2 phases (M = Th, U, Np). PuO_2 is therefore possibly easier to be reduced to a 3+ state [6]. (iv) Finally, only two basic assessments exist for the high temperature region [7, 8] which also have to be updated with the newer results for PuO_2 [9].

In general, $(Pu,Th)O_2$ represents a potential nuclear fuel material, for which the high temperature behaviour is a fundamental parameter for the safety evaluation. Thorium dioxide based fuels could be used to reduce the long term radiotoxicity of the spent fuel by fissioning the transuranium elements [10] and is still being tested for these purposes [11]. In addition, ThO_2 has favourable material properties in terms of a nuclear fuel: proliferation, waste concerns and operating conditions can be improved compared to uranium based fuels [12].

It is therefore interesting to assess fundamental properties of this system and compare them to other mixed actinide dioxides. In the present work laser melting was used to study the melting/solidification behaviour. Possible effects in the material during these high temperature experiments such as segregation or stoichiometric changes have been investigated after cooling by scanning electron microscopy (SEM), Energy-dispersive X-ray spectroscopy (EDX), X-ray diffraction (XRD) and Raman spectroscopy. In that context, Raman spectroscopy has been used for the first time to characterise this compound. Finally, the PuO_2 – ThO_2 pseudo-binary phase diagram was refined with new experimental high temperature phase transformation data.

7.2. Experiments

7.2.1. Sample preparation

The samples were produced using a sol-gel external gelation method with different molar fractions of ThO_2 (x(ThO_2) = 0.05, 0.15, 0.46, 0.70, 0.92, 0.97). Samples from the same batch with 70, 92 and 97 mol % ThO_2 were used already for thermal diffusivity and con-

ductivity studies [13], whereas samples with 15, 46, 70, 92 and 97 mol % ThO$_2$ were used for heat capacity studies [3]. Material with 70, 92 and 97 mol % ThO$_2$ was produced in the period of the 5th framework program of the European Commission [14, 15], while samples with 5, 15 and 46 mol % ThO$_2$ were fabricated in a similar way before the melting experiments. Details about the sample preparation can be found in the aforementioned material property studies [3, 13].

7.2.2. LASER MELTING EXPERIMENTAL SETUP

The experimental apparatus used in this work was described in detail elsewhere (e.g. [5, 16, 17]). Only the main aspects of the setup and differences to recent work [5] are presented.

In laser melting experiments the molten volume is held by the outer periphery of the colder solid material, thus, preventing contamination by foreign material. Hence the method can be described as quasi - containerless.

The samples were preheated with low laser power (45 W) for 30 s to reduce the effect of thermal shocks. After this time a steady state heat distribution through the sample with a measured front surface temperature of 1500 K to 2000 K was established and the sample was brought to melting with pulses of different length (100 ms to 1 s) at a constant power plateau (up to 1200 W). The chosen power depends also on the composition of the sample since ThO$_2$ is in the near infra-red (laser wavelength = 1064 nm) nearly transparent. This transparency is temperature-dependent and disappears at high temperature where absorption/emissivity values become similar to other actinide dioxides [18]. After each pulse the power was set back 45 W to let the sample re-solidify and reach again a surface temperature below 2000 K before the next pulse was started one second later. A maximum of 4 pulses were applied in a set of shots before letting the sample cool naturally. Such heating cycles were performed under air slightly pressurized up to 0.3 MPa to reduce vaporisation.

The surface radiance temperature in the centre of the heated zone was measured by a pyrometer operating at 652 nm with a nominal spot size of approximately 0.5 mm in diameter. The onset of melting was detected by the appearance of vibrations in the signal of a probe laser (Ar$^+$, cw, 1.5 W) reflected by the sample surface (reflected-light-signal technique, or RLS)[17]. These vibrations disappear during cooling at the thermal arrest and therefore also establish the temperature at the thermal arrest as the solidification temperature.

The true temperature was obtained by correcting the radiance temperature with the measured normal spectral emittance NSE ($\varepsilon(\lambda, T)$) with a further spectrometer, based on a linear array of 256 photodiodes (488 to 1011 nm). The measured radiance spectra can be fitted by the radiance temperature, T_λ, calculated with Wien's approximation of Planck's law and plotted as a function of wavelength, λ, assuming a grey body with constant wavelength independent emissivity $\varepsilon(T)$. For PuO$_2$ and ThO$_2$ the already published data were used (0.83 for PuO$_2$ [19]; 0.87 for ThO$_2$ [5]). Since the emittance study could not be performed on all compositions, a linear interpolation between the two NSEs of PuO$_2$ and ThO$_2$ was made, giving to the intermediate composition a weighted value related to the amount of the two end members, which are shown in Tab. 7.1. This assumption seems reasonable especially considering the close emittance values of the

two end members and agreed with the measured values for intermediate compositions.

The sample surface was considered to be smooth, as supported by the good repeatability of the measured radiance temperatures upon solidification. The solidification temperature of (Pu,Th)O_2 was determined from the cooling stage of the recorded thermograms, locating the corresponding thermal arrest. As often observed in rapid laser heating experiments of such materials, and confirmed by numerical simulation [20], the heating stage often occurs too quickly to reveal an observable melting arrest during this phase of the thermal cycle but could be estimated with the help of the RLS. In general, temperatures obtained by assistance of the RLS upon heating are similar to the ones during cooling [4, 5].

Uncertainties of the measurements were calculated according to the error propagation law, taking into account the uncertainty associated to pyrometer calibration, emissivity, transmittance of the optical system and the accuracy in detecting the onset of vibrations in the reflected light signal. The estimated cumulative uncertainty is thus lower than ± 2 % of the reported temperatures in the worst cases for the solidification temperatures (calculated a combined uncertainty with a confidence level of 0.95 (k ≈ 2)).

7.2.3. Material characterisation

To check the composition, the material was investigated with different methods before and after the experiments. First, secondary electron (SE) and backscattered electron (BSE) images were recorded on a scanning electron micro-scope (SEM with a Philips XL40®) operated at 25 kV.

Additionally, the samples were characterized with a Bruker D8 advance ® X - ray diffractometer (Cu K$_\alpha$ radiation, range: 10° – 120° with 0.009 steps). The measurement was later also conducted on re-solidified material to see a possible effect from melting.

The third method used was Raman spectroscopy. Raman spectra were measured with a Jobin –Yvon® T64000 spectrometer used in the single spectrograph configuration. The excitation source was a Coherent®cw laser (Ar$^+$or Kr$^+$) radiating at wavelengths of 488 nm, 514.5 nm, 647 nm, and 752 nm. Spectra are measured in a confocal microscope with a 50x magnification and long focal distance (about 1 cm) with a spatial resolution of 2 x 2 μm on the sample surface.

7.3. Results

7.3.1. Melting experiments

A typical temperature versus time curve obtained with the laser melting setup is shown in Fig. 7.1. Details of the suggested interpretation can be found in earlier publications [4, 5, 20]. The local maximum temperature at the thermal arrest was taken as the solidification temperature of the surface. A flat thermal arrest was not observed for any of the actinide oxides, since the molten surface solidifies very quickly and builds a crust upon the molten material in only a few milliseconds. The solidification happens very quickly compared to the duration of a heating cycle. The solidification arrest can only be seen in the inset of Fig. 7.1 in which time resolution has been increased.

Fig. 7.2 and Tab. 7.1 summarise the solidification points observed with the different (Pu,Th)O_2 compositions investigated in this work. Single measured NSE values are also

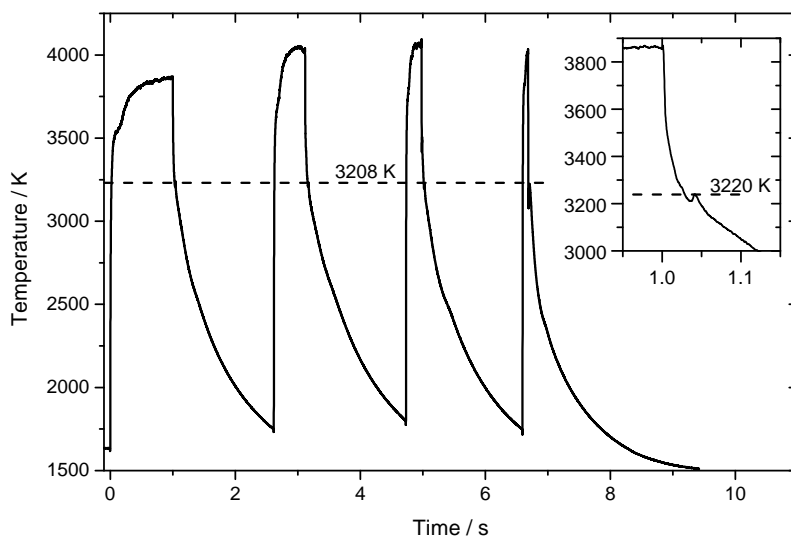Figure 7.1: A sequence of four laser heating pulses performed on $(Pu_{0.54}Th_{0.46})O_2$ in air. The heating laser power was maintained at 45 W in between the high-power pulses. The inset shows the solidification of the first heating/cooling cycle in more detail. The average solidification temperature of $(Pu_{0.54}Th_{0.46})O_2$ at 3208 K (calculated with a constant $\varepsilon = 0.846$) is suggested by the horizontal line, as well as the solidification temperature of the first cycle in the inset at 3220 K.
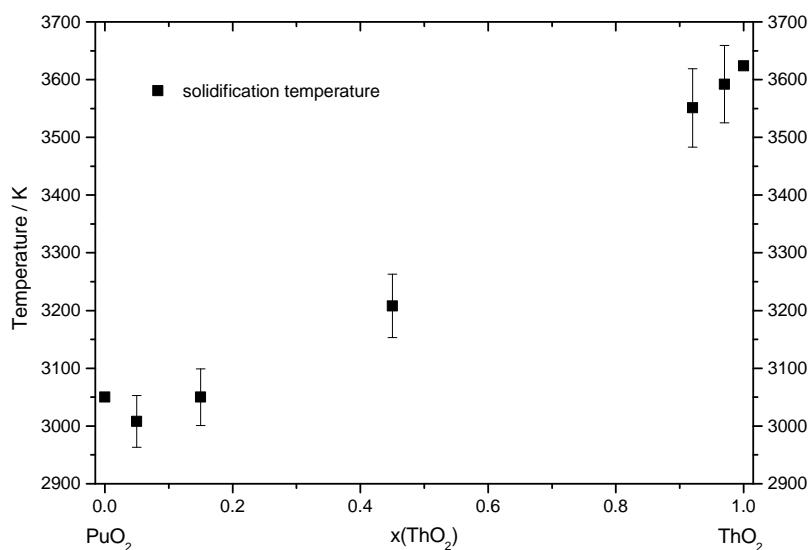
Figure 7.2: The average solidification temperatures determined at the thermal arrest for mixed $(Pu, Th)O_2$. The uncertainties in temperature are determined in the thermal analysis. Composition uncertainties are deduced from and XRD measurements. Solidus and liquidus lines for an ideal solid solution are plotted for comparison. Possible segregation to 3 phases is shown by theoretical solidification paths from high temperature.

shown in Tab. 7.1, which confirm within the uncertainty the assumption of interpolated values for the emissivity. For the calculation of the true solidification temperature the interpolated values were chosen.

Composition	interpolated NSE	measured NSE	No. of shots	Solidification temperature / K
PuO$_2$	0.830	-	-	3050 K $\pm$ 55 K [4]
(Pu$_{0.95}$Th$_{0.05}$)O$_2$	0.832	0.83	25	3008 K $\pm$ 45 K
(Pu$_{0.85}$Th$_{0.15}$)O$_2$	0.838	0.82	23	3050 K $\pm$ 49 K
(Pu$_{0.54}$Th$_{0.46}$)O$_2$	0.846	0.86	17	3208 K $\pm$ 55 K
(Pu$_{0.30}$Th$_{0.70}$)O$_2$	0.854	-	2	-
(Pu$_{0.08}$Th$_{0.92}$)O$_2$	0.862	0.90	6	3551 K $\pm$ 68 K
(Pu$_{0.03}$Th$_{0.97}$)O$_2$	0.868	-	3	3592 K $\pm$ 67 K
ThO$_2$	0.870	-	-	3624 K $\pm$ 86 K [5]

Standard uncertainties u are $u(p)$ = 0.005 MPa, u_r *(NSE)* = 0.05, and the combined expanded uncertainty for the temperature, *U(T)*, is given for each case with a confidence level of 0.95 (k $\approx$ 2).

Table 7.1: Interpolated and measured normal spectral emittance (NSE), and solidification temperatures observed by thermal arrest analysis in this work on mixed (Pu, Th)O$_2$ at pressure p = 0.3 MPa.

Within the experimental uncertainty the temperature remains the same for the solidification of several successive shots, which indicates that segregation effects during the experiments seem to have only a minor influence. Due to the restricted number of samples, the resulting uncertainty is higher for Th-rich compositions. A composition with 70 mol % ThO$_2$ with only one available sample was also studied, but the thermal analysis was not successful due to malfunctioning pyrometers.

Interestingly (Pu, Th)O$_2$ solid solutions shows a minimum in the melting / solidification transition around 5 mol % ThO$_2$ content, similar to (U, Th)O$_2$ [5].
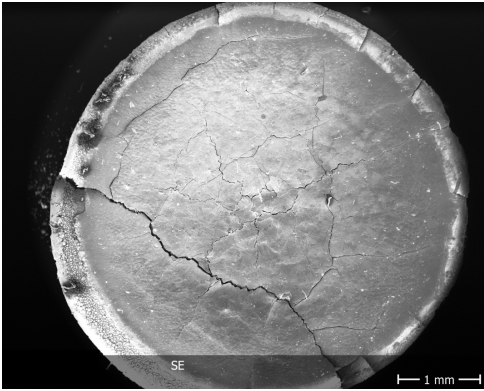
7.3.2. Material characterisation

Scanning electron microscopy

Figure 7.3: A secondary electron image of a (Pu$_{0.85}$Th$_{0.15}$)O$_2$ sample after several heating/cooling cycles.

The laser irradiated sample surface was analysed with scanning electron microscopy at different magnifications. An example of such an analysis can be seen in Fig. 7.3. The re-solidified surface of a $(Pu_{0.85}Th_{0.15})O_2$ sample is shown. Cracks usually form during final cooling to room temperature. In back-scattered electrons (BSE) analysis only homogeneous material distribution on the surfaces is found. Energy-dispersive X-ray (EDX) analysis has relatively large uncertainties (± 10 % in absolute composition) considering the not-polished surfaces investigated here, and showed no changes in composition along the surface between re-solidified and not melted material.

RAMAN SPECTROSCOPY

Raman measurements were conducted on the surface of the sample from the centre to the outside section, on re-solidified, not melted, and fresh (not laser heated) material. The emission volume of the EDX is deeper than the expected penetration depth of the laser beam used in Raman spectroscopy as estimated with the Lamber-Beer law [5], so that possible surface effects are revealed better with the latter method.

The fluorite-like structures studied here (fcc, $Fm\bar{3}m$) have only one (triply degenerate) Raman active vibration (T_{2g}), which is taken as a reference peak for our investigation. In stoichiometric PuO_2 the peak is found at 478 cm^{-1} and in thoria at 465 cm^{-1} relative to the excitation wavelength [21]. The spectra of mixed, not melted $(Pu,Th)O_2$ show additional peaks as seen in Fig. 7.4. Spectra of $(Pu_{0.08}Th_{0.92})O_2$ of acceptable quality were be obtained and were not used in this comparison. In re-solidified material the peaks stayed at the same position, as shown for the 46 mol % ThO_2 in Fig. 7.4.
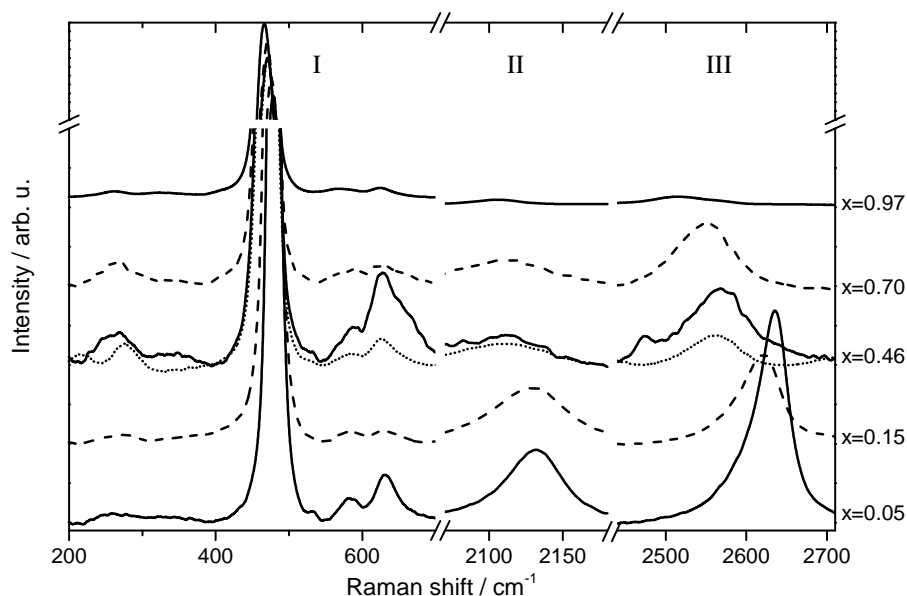

Figure 7.4: Single Raman spectra measured with 514 nm excitation wavelength on not melted material of different $(Pu_{1-x}Th_x)O_2$ compositions. The spectra are normalised to the T_{2g} peak intensity and shown at 3 different wavenumber ranges. At x(ThO_2)=0.46 the dotted line represents a re-solidified surface measurement.

The spectra in Fig. 7.4 are divided in three parts. Part I from 200 - 700 cm^{-1}, part II from about 2000 - 2200 cm^{-1}, part III from about 2500 - 2700 cm^{-1}. In part I the characteristic features for the investigated compounds are located which will be discussed here. One can identify a peak at approx. 260 cm^{-1}, which can be allocated to the LO mode, a weak mode at 335 cm^{-1}, and the T_{2g} peak between 465 and 478 cm^{-1}, depending on the composition. The position of the latter is shown in more detail in Fig. 7.5.

This is followed by modes at about 535 cm^{-1} (characteristic for hypostoichiometry [22]), around 575 cm^{-1} (TO mode) and at about 630 cm^{-1}. The last was attributed in the case of uranium oxides to a U_4O_9 phase [22]. Part II and III show peaks which were also observed by Sarsfield et al. for pure PuO_2 [23]. Both peaks ("II" and "III") change position and become weaker with increasing ThO_2 content. Interestingly, the ratio between these and T_{2g} is nearly constant as seen in Tab. 7.2.

Composition	Raman shift / cm^{-1}			Raman shift ratios	
	T_{2g}	"II"	"III"	"II"/T_{2g}	"III"/T_{2g}
PuO_2	478	2125	2629	4.45	5.50
$(Pu_{0.95}Th_{0.05})O_2$	478.9	2130	2631	4.45	5.49
$(Pu_{0.85}Th_{0.15})O_2$	476.9	2130	2620	4.47	5.49
$(Pu_{0.54}Th_{0.46})O_2$	471.1	2112	2598	4.48	5.51
$(Pu_{0.30}Th_{0.70})O_2$	469.7	2109	2547	4.49	5.42
$(Pu_{0.08}Th_{0.92})O_2$	461	-	2496	-	5.41
$(Pu_{0.03}Th_{0.97})O_2$	466.5	2104	2517	4.51	5.40
ThO_2	464	-	-	-	-

Standard uncertainties u are $u(p)$ = 0.005 MPa and $u(Raman\ shift)$ = 2 cm^{-1}.

Table 7.2: The evolution of the Raman T_{2g} and other peak positions with ThO_2 content in not melted $(Pu,Th)O_2$ measured at pressure p = 0.1 MPa.

Especially interesting is the T_{2g} peak position (Fig. 7.5), which is characteristic for each composition. Fig. 7.5 presents the peak position for all compositions in dependence of the ThO_2 content from several measurements on the surfaces with different laser wavelength. Measurements taken on different spots were averaged since no differences were seen radially on the surface or from different samples with the same composition. The shift in position seems to depend linearly on the ThO_2 content of the samples. Since measurements with $(Pu_{0.08}Th_{0.92})O_2$ were not clearly interpretable, these results should be only considered with caution. A difference between the melted and not melted material could not be found, which suggests no change of composition during melting and re-solidification on the surface.

POWDER X-RAY DIFFRACTION

In addition bulk analyses was performed with XRD analysis to show influences on a larger scale. Fig. 7.6 and Tab. 7.3 show the lattice parameter obtained by Rietveld refinement of the diffraction pattern of the samples previously analysed by microscopy technique and Raman spectroscopy.

PuO_2 and ThO_2 are expected to form a solid solution and to follow Vegard's law. Not melted material in this work shows a positive deviation in nearly all compositions (see
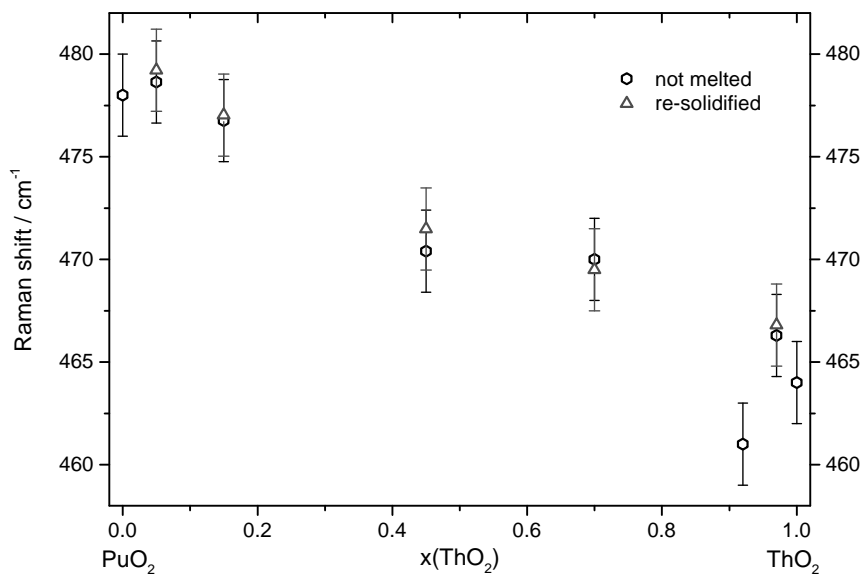
Figure 7.5: Averaged T_{2g} peak positions ($\pm$ 2 cm^{-1}) in not melted (polygon) and re-solidified (triangle) (Pu,Th)O$_2$.
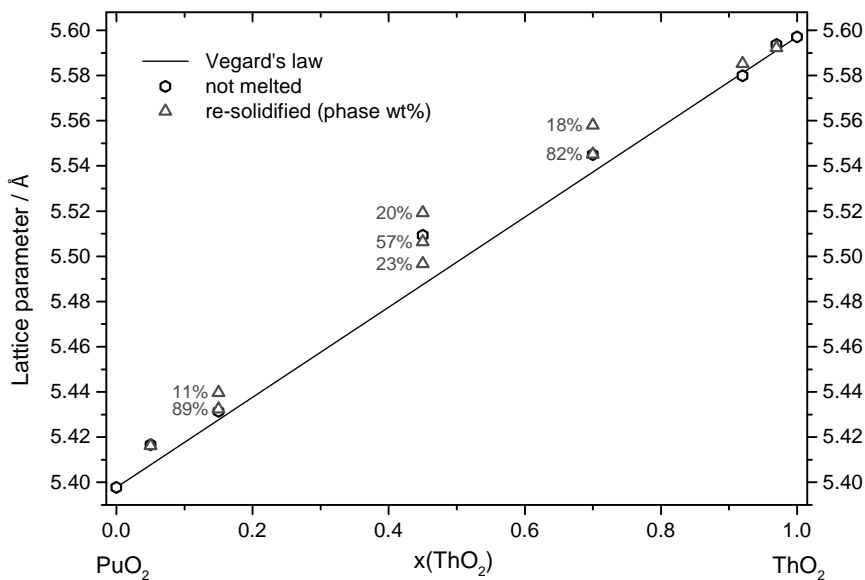
Figure 7.6: Lattice parameters for investigated (Pu,Th)O$_2$ compositions ($\pm$ 0.002 Å). Vegard's law is indicated by the straight line between the end-members. Re-solidified (triangles) and not melted material (polygon) are shown for measured samples. For cases with more than 1 phase, the numbers give the relative amount of each phase in weight percentage.

Composition	Lattice parameter / Å			
	not melted	re-solidified		
		main	2nd	3rd
PuO_2	5.3978	-	-	-
$(Pu_{0.95}Th_{0.05})O_2$	5.4167	5.4161	5.4165	-
$(Pu_{0.85}Th_{0.15})O_2$	5.4314	5.4324	5.4397	-
$(Pu_{0.54}Th_{0.46})O_2$	5.5093	5.5064	5.5192	5.4967
$(Pu_{0.30}Th_{0.70})O_2$	5.5451	5.5452	5.5582	-
$(Pu_{0.08}Th_{0.92})O_2$	5.5799	5.5852	-	-
$(Pu_{0.03}Th_{0.97})O_2$	5.5937	5.5922	-	-
ThO_2	5.5971	-	-	-

Standard uncertainties u are $u(p) = 0.005$ MPa and $u(lattice\ parameter) = 0.002$ Å.

Table 7.3: Lattice parameters of different $(Pu,Th)O_2$ compositions of not melted (and not-heated) and re-solidified material measured at pressure p = 0.1 MPa.

Fig. 7.6), but still follows the trend of Vegard's law. Such deviation is also visible in other work with mixed actinide dioxides presenting the lattice parameter. In the work of Hubert et al. [24] the lattice parameter deviates up to 0.015 Å from Vegard's law for $(Pu,Th)O_2$, which is about the same deviation found in this work.

For the sample containing 46 mol % ThO_2, a phase separation into three fcc phases is observable after melting, but the most abundant phase remains similar to the fresh material. The re-solidified material in other intermediate compositions shows a also phase separation, but only into two phases. The most abundant phase still remains for all compositions similar to the fresh and not melted material.

7.4. Discussion

The accuracy with which a phase diagram is experimentally determined depends on two main issues: the accuracy in the measurement of temperature and the accuracy in the characterisation of the sample composition at the exact moment when the phase transitions occur. In the following section, first the impact of the melting experiments and the material analysis is discussed. Afterwards the phase diagram of $(Pu, Th)O_2$ is critically revisited.

7.4.1. Melting temperature results

Only one assessment of the PuO_2-ThO_2 phase diagram as a pseudo-binary system exists so far [7]. With newer data for PuO_2, this assessment was updated. The results in the present study for intermediate compositions are in reasonable agreement with former work on the pure end members [18, 19].

Considering results from Phase-Field simulation of such laser heating experiments [4, 5, 20], the temperature at the thermal arrest or peak (see Fig. 7.1) was determined to be the point when the surface has completely resolidified. Therefore it is reasonable to equalise the solidification temperature of this work with a solidus.

The melting temperatures of the ThO_2-rich compositions follow closely the solidus calculated with an ideal solution assumption (see Fig. 7.2). Also in the earlier assessment [7] this trend was visible . But only compositions with a ThO_2 content up to 70 mol % were investigated before.

The PuO_2-rich compositions show a deviation from the ideal binary solution with the minimum around a 5 mol % ThO_2 content, as it was already reported for other mixed actinide oxides [4, 5]. Due to its comparatively high oxygen potential among the actinide oxides, plutonium dioxide may be more easily reduced, and therefore an assumption of a stoichiometric pseudo-binary section may not be fully suitable in this region. The material analysis has not shown any deviation which could account completely for this behaviour. The Raman surface analysis has shown possible lattice defects, maybe resulting from a small hypostoichiometry of the sample. But the material analysis was conducted at room temperature after the experiments. Changes in the material which are found later in the analysis are probably quenched from high temperature. In-situ effects at high temperature, such as possible reversible or temporarily oxygen losses, cannot be seen by any material analysis.

Moreover, one observes segregation effects by the XRD analysis, which probably took place at high temperature, and were partially quenched to room temperature. The phase analysis showed up to three distinct phases, which should have hence a distinct measurable phase transition temperature, if they crystallise from the liquid on the surface. In the thermograms these effects are not observable as different solidification arrest or clear inflections. The proportion of new appearing phases is small and therefore the latent heat released by this new phase will be also small. The reflected light signal technique only showed one phase change during cooling. As well, the location of this segregation cannot be determined exactly in the molten pool or later in the re-solidified material. At the surface, where the temperature is measured, the material analysis by Raman spectroscopy has not shown signs of segregation, so that also the uncertainties in composition for the phase transition are taken from the uncertainties from the XRD analysis for the most abundant phase at each composition in re-solidified material.

7.4.2. MATERIAL CHARACTERISATION

MICROSCOPY

Within the uncertainty of the EDX and BSE analyses, no differences in composition of not melted and re-solidified material or a phase separation was found on any sample at different magnifications. Any segregation effects as seen by the XRD results seem to not occur close to the surface. However, with this analysis method small differences are difficult to determine and might not be detected.

RAMAN SPECTROSCOPY

An analysis of the composition can be done with the Raman T_{2g} vibration, whose shift is proportional to the ThO_2 content (Fig. 7.5). For mixed crystals, it has been estimated already with the random-element-isodisplacement model (REI) [25], that the optic mode frequency varies continuously and approximately linearly with concentration from the frequency characteristic of one end member to that of the other end member in an one-mode behaviour. Re-solidified and not melted material showed in all samples and com-

positions nearly no difference for the T_{2g} position. Thus, no segregation effects can be deduced from this analysis on the surface of the samples.

The Raman spectra show further modes (Fig. 7.4). The LO (at 260 cm^{-1}) and TO (575 cm^{-1}) modes are normally only visible by IR spectroscopy and become Raman active only if the lattice is disordered. These observed peaks therefore indicate defects in the lattice, which can be linked to energetically favourable oxygen Frenkel defects or oxygen losses, possibly quenched to room temperature. Also the peaks at 535 and 630 cm^{-1} can be related to a disorder in the lattice, while a formation of M_4O_9 with these compounds, as in uranium compounds [22], seems unlikely. The origin of the band around 335 cm^{-1} remains unclear.

The modes at higher energy (around 2100 and 2600 cm^{-1}) seem to be related to the composition and obviously to PuO_2. Sarsfield et al. [23] extensively discussed the origin of these peaks, ruling out interactions with the surrounding atmosphere and material, and suggesting an electronic origin with energies of about 262 and 324 meV respectively. The nearly constant ratio observed at different compositions between the T_{2g} and the higher energy peaks (see Tab. 7.2) tempt one to see a relationship between these modes. If these peaks were a combination of T_{2g} with another transition or vibration, these should be visible in the measured spectra. But no other modes were found in the spectra which had the required wavenumbers. Hence, no combinations can be so far clearly attributed to the high energy peaks in these spectra, and the origin(s) of these signals remain unclear.

POWDER X-RAY DIFFRACTION

The powder X-ray diffraction analysis was used to determine lattice constants of different samples. Deviations from Vegard's law in the lattice parameters could have several reasons: (i) composition shifts, (ii) defects, or (iii) stoichiometry changes. It is not possible to distinguish them only with the lattice parameter data, so that the influences have to be discussed separately but all may be present together as presented for (iv) the phase separation found in this work. In general, the re-solidified material could also be contaminated with not-melted material, which might also result in multiple phases due to a difficult separation during the preparation for the powder X-ray diffraction analysis.

(i) A deviation of the lattice parameter in not heated or not melted samples could be caused by inaccuracy in composition during the sample preparation, as seen in other work with (Pu,Th)O_2 [24]. The deviation of the most abundant phase after melting is assumed as a worst-case uncertainty source for the solidification temperature in Fig. 7.2, resulting in error bars towards the ThO_2 side of the phase diagram.

(ii) Defect formation due to age would increase the lattice parameter [23]. Additionally, more defects due to other origin than a self-irradiation may be introduced at higher temperature and quenched to room temperature. Small deviations from Vegard's law could be related to this issue.

(iii) A change in stoichiometry inducing a lattice expansion is difficult to quantify. Different studies on hypostoichiometric actinide dioxides suggest a lattice swelling [2, 26], but there is no data so far for mixed (Pu,Th)O_2. The expansion rate of the lattice of (Pu,Th)O_{2-y} can be approximated from literature data of other dioxides [2, 5] to 0.04 Å per y=0.1, leading to only limited hypostoichiometry for all compositions (maximum

at the 2nd phase of $(Pu_{0.54}Th_{0.46})O_{1.93}$ compared to fresh material $(Pu_{0.54}Th_{0.46})O_{1.96}$. Melting of the material seems not to have an strong influence on stoichiometry, since all re-solidified samples have a very similar lattice parameter compared to not melted material. Nevertheless, a slight hypostoichiometry of the samples cannot be excluded, especially since the rather complicated Raman spectra of these compositions also show signs of a disturbed lattice, which can be linked to oxygen losses.

(iv) Considering only stoichiometric changes and disregarding changes in composition, the phase separation seen in intermediate compositions, could be interpreted as a phase close to stoichiometry and two phases more reduced. This would also imply that the initial, fresh material is either not stoichiometric and/or has a different composition. A change to a hyperstoichiometric phase in PuO_2-rich compositions, as one might expect from the higher oxygen potential of PuO_2 compared to ThO_2, was not found. A reduction as seen by Truphémus et al. [27] to three distinct phases for non-stoichiometric $(U,Pu)O_2$ could not be seen in that extent for $(Pu,Th)O_2$. To explain the effects seen in this study only with oxygen related phenomena, one has to assume a slightly non stoichiometric section in the Pu-Th-O phase diagram as already suggested for mixed $(U,Pu)O_2$ [2, 28], with a miscibility gap for non-stoichiometric material only for intermediate compositions. Therefore only oxygen defects, quenched from high temperature to room temperature could be partly accountable for the lattice parameter changes, whereas these are unlikely to cause a phase separation.

But the appearance of more phases can be also linked to a segregation upon melting or freezing process. Phases, enriched and reduced with material with the higher melting point, can be explained in terms of segregation effects during cooling and solidification of the material with the help of the binary phase diagram (Fig. 7.7). If the cooling process is fast enough compared to the diffusion processes, quenching of the high temperature phases is possible. When material solidifies with an enriched composition (1st solidified phase), the remaining melt is equally depleted in composition. If there is not enough time to regain the initial composition by diffusion, a new phase would appear with a depleted composition. But if the solidification happens quickly enough, there is even not enough time to reach a homogeneous melt depleted in composition compared to the initial material and three phases might form, with a phase equal to the initial material (2nd solidified phase) and depleted in composition (3rd solidified phase). The phase separation happens presumably only at the solidification front, which are supposedly located at the edges of the molten pool [4]. Because it was not possible to select the samples for the XRD material analysis by these criteria, the amount of phases and weight of the enriched and reduced phases is not always found to be the same.

Other investigated mixed actinide dioxides showed no segregation $((U,Pu)O_2$ [4]) or in much less extent $((U,Th)O_2$ [5]). This can be explained with the binary phase diagrams. Since the melting temperatures of the end members are closer to each other in the latter cases, segregation is less probable, because the liquidus and solidus points are also closer together. The composition which solidifies the first is nearby the initial composition and may be not seen in any material analysis method.

Segregation to different phases was not seen by a shift of the T_{2g} position in the Raman analysis nor in the microstructure analysis. All observed phases have a fcc structure, which makes it more difficult to see small deviations introduced by a small composition

change. In the case of (U,Th)O$_2$, segregation effects were also seen in the Raman analysis [5]. If these changes only affect the material close to the surface, they are very likely to be overseen or averaged out with powder diffraction analysis method and are very difficult to locate.

7.4.3. PHASE DIAGRAM CONSIDERATIONS

In the hypothetical case of no interaction between the solution end-members, assuming that the heat capacity is approximately the same for solid and liquid phases in the vicinity of melting, and taking into account that the only entropy contributions to Gibbs energy are related to configurational terms, the ideal-solution solidus and liquidus lines of the binary phase diagram are solely defined by the melting temperatures and the enthalpies of fusion of the two end members [29] as shown by the dotted lines in Fig. 7.7. Actinide dioxide melting enthalpy values assessed by Konings et al. [30] are used to calculate the optimized solidus and liquidus plotted in Fig. 7.7 together with the current experimental data. It is evident that the current experimental data relative to plutonia-rich compositions deviate from such phase diagram. Therefore, the system cannot be represented by considering only an ideal behaviour of both solid and liquid solutions.

Deviations from ideality, can be related to various factors, as for example lattice strain caused by a difference in the ionic radii of Pu^{4+} and Th^{4+}, or a different oxygen potential of the pure end members [4]. Recent research [2, 4] has shown that the latter point plays an important role in the very high temperature behaviour of these oxides, especially around the melting transition. It has been reported [31], that pure plutonium dioxide melts congruently at a slightly hypostoichiometric composition (PuO$_{1.98\pm0.02}$). Therefore, mixed oxides including plutonium dioxide cannot be rigorously treated as purely pseudo-binary ((M$_1^{4+}$,M$_2^{4+}$)O$_2$), but are thermodynamically more accurately described as ternary systems ((M$_1^{4+}$,M$_2^{4+}$,M$_2^{3+}$)O$_2$). This behaviour, thoroughly assessed for the system U-Pu-O [31], should certainly apply also to the current system Pu-Th-O. However, a full thermodynamic assessment of the ternary Pu-Th-O system goes beyond the scopes of the present work, and will be left for further investigation. Therefore, as a first approximation, the solidus and liquidus lines are optimized here, according to the current experimental data, in the pseudo-binary PuO$_2$-ThO$_2$ plane in the rough assumption that PuO$_2$ does melt congruently. By considering excess Gibbs energy terms instead of an ideal solution, one can find the best data fit in a pseudo-binary plane, including the minimum melting point around x(ThO$_2$) = 0.05, following an approach similar to that proposed by Pelton and Thompson [32]. The following expression has thus been used for the excess Gibbs energy of the solid phase:

$$\Delta G^{exc}(x(ThO_2)) = x(PuO_2)^3 \cdot x(ThO_2) \cdot \Omega \tag{7.1}$$

$x(ThO_2)$ and $x(PuO_2)$ are the mole fractions of ThO$_2$ and PuO$_2$, respectively. Ω is the non-ideal interaction energy term between PuO$_2$ and ThO$_2$, assumed to be a temperature - independent parameter. In Eq. 7.1, ΔG^{exc} coincides with the excess enthalpy in the non-ideal solution model, as excess entropic contributions have been neglected. $x(PuO_2)$ appears at the third power to account for asymmetry of the model, according to the fact that deviations from the ideal solution behaviour, and in particular a minimum melting point, have been mostly observed in PuO$_2$-rich compositions. In the current

model, the interaction parameter Ω is considered to be zero in the liquid phase (non-ideality is neglected in the liquid).
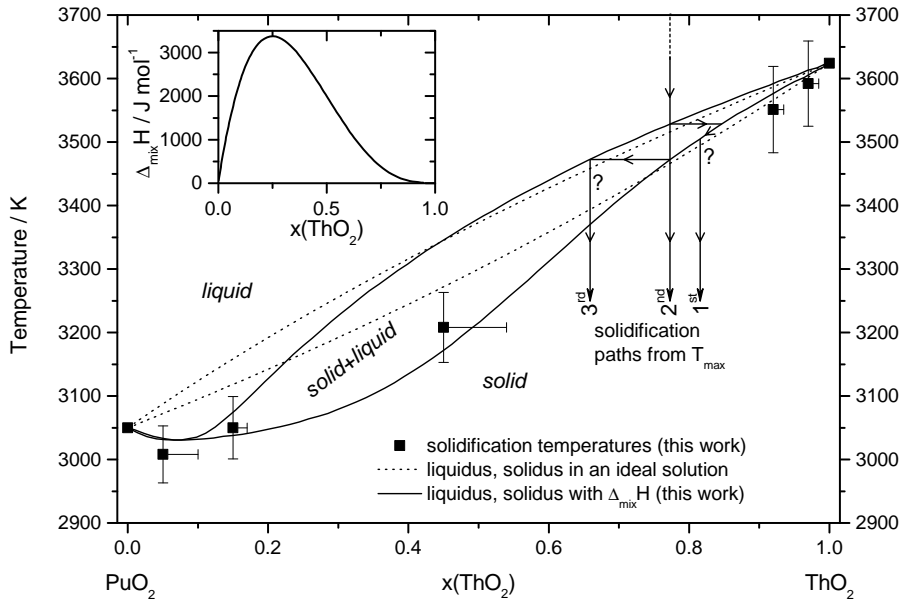

Figure 7.7: High temperature phase diagram of the pseudo-binary PuO$_2$-ThO$_2$ system. Composition uncertainties are deduced from and XRD measurements. Results of this work are shown together with the ideal solution binary solidus and liquidus (dotted lines). The solid solidus and liquidus lines take into account deviations from the ideal solution behaviour. They have been calculated by considering a mixing enthalpy in the solid solution, whose values reported in the inset have been optimized in order to best fit the current experimental data with a polynomial formalism as shown in Eq. 7.1. Possible segregation to 3 phases is shown by theoretical solidification paths from high temperature.

The resulting optimized solidus and liquidus lines are plotted in Fig. 7.7 together with the current experimental data points. The corresponding best value for the interaction parameter is $\Omega = 36$ kJ mol^{-1}, yielding the excess mixing enthalpy, $\Delta_{mix}H$, plotted in the inset of Fig. 7.7. The minimum melting point can be reasonably fitted with the current approach, as well as the other experimental data points, within the reported uncertainty bars. The approximations adopted in the current phase boundary optimization are somewhat coarse, because they imply that plutonium dioxide melts congruently and, moreover, neglect non-ideality parameters in the liquid phase. Nonetheless, the fair quality of the present data fit permits to quantify, roughly, the non-ideality of the alleged pseudo-binary system, whereby even changes in oxygen stoichiometry (outside the PuO$_2$-ThO$_2$ pseudo-binary plane) can be accounted for as deviations from ideality. Thus, the modest values of the current excess solution enthalpy show that the minimum melting point observed for just a few mol % of ThO$_2$ dissolved in PuO$_2$ can be justified even with small deviations from an ideal behaviour of the pseudo-binary system. Such deviations can be most probably related, in a more detailed approach, to the formation of oxygen defects, and in particular oxygen losses, due to the high oxygen potential of

plutonium dioxide and PuO_2-rich compositions at temperatures close to melting. This is in line with the material characterization in this work which shows signs of hypostoichiometry in the samples. As mentioned above, a non-stoichiometric phase diagram as already suggested for $(U,Pu)O_{2\pm y}$ by a full CALPHAD optimization [31], seems a reasonable assumption for the description of melting in the $(Pu,Th)O_2$ system, too. In addition, a similar melting behaviour has recently been assessed also for the $(U,Th)O_2$ system [5]. There, however, uranium has a more complex chemistry than plutonium, permitting the accommodation of both oxygen vacancies (valence state U^{3+}) and interstitials (U^{5+}, U^{6+}). This makes the high temperature behaviour more difficult to estimate in uranium - thorium mixed dioxides [5]. Finally, in the light of these observations, it is suggested that also the plutonium dioxide – thorium dioxide system can only be fully understood with an assessment of the ternary Pu-Th-O system rather than a simplified pseudo-binary section.

7.5. CONCLUSIONS

WITH new laser - heating results on the melting transition, the high temperature phase diagram of mixed plutonium-thorium dioxides has been assessed in the present work. Large deviations from the few earlier results are reported. With the material characterization performed before and after melting by SEM, Raman spectroscopy and XRD, phase separation processes in relation with the phase diagram were identified and explained. Additionally, new observations of high energy Raman modes are presented and related to PuO_2.

As with other mixed actinides dioxides, mixed plutonium-thorium dioxides show a minimum melting point. Such a minimum occurs in plutonium dioxide-rich compositions (around 95 mol %) at a temperature close to 3000 K. Moreover, the current observations lead to the conclusion that such effects can only be fully understood within a comprehensive study of the ternary Pu-Th-O system. The material analyses performed here support this interpretation by yielding signs of oxygen losses for several compositions. These results emphasize that knowledge and control of the oxygen potential in the investigation of the actinide dioxides is crucial, especially at high temperatures.

REFERENCES

[1] R. Böhler, P. Çakır, O. Beneš, H. Hein, R. J. M. Konings, and D. Manara, *High temperature phase transition of mixed (PuO$_2$ + ThO$_2$) investigated by laser melting,* J. Chem. Thermodyn. **81**, 245 (2015).

[2] C. Guéneau, A. Chartier, and L. V. Brutzel, *2.02 - Thermodynamic and Thermophysical Properties of the Actinide Oxides,* in *Compr. Nucl. Mater.*, edited by R. J. Konings (Elsevier, Oxford, 2012) pp. 21–59.

[3] O. Vălu, O. Beneš, R. Konings, and H. Hein, *The high temperature heat capacity of the (Th,Pu)O$_2$ system,* J. Chem. Thermodyn. **68**, 122 (2014).

[4] R. Böhler, M. Welland, D. Prieur, P. Çakır, T. Vitova, T. Pruessmann, I. Pidchenko,

C. Hennig, C. Guéneau, R. Konings, and D. Manara, *Recent advances in the study of the UO$_2$-PuO$_2$ phase diagram at high temperatures,* J. Nucl. Mater. **448**, 330 (2014).

[5] R. Böhler, A. Quaini, L. Capriotti, P. Çakır, O. Beneš, K. Boboridis, A. Guiot, L. Luzzi, R. Konings, and D. Manara, *The solidification behaviour of the UO$_2$-ThO$_2$ system in a laser heating study,* J. Alloys Compd. **616**, 5 (2014).

[6] H. Kinoshita, D. Setoyama, Y. Saito, M. Hirota, K. Kurosaki, M. Uno, and S. Yamanaka, *Thermodynamic modelling and phase stability assessment of MO$_{2-x}$ oxides with a fluorite structure,* J. Chem. Thermodyn. **35**, 719 (2003).

[7] K. Bakker, E. Cordfunke, R. Konings, and R. Schram, *Critical evaluation of the thermal properties of ThO$_2$ and Th$_{1-y}$U$_y$O$_2$ and a survey of the literature data on Th$_{1-y}$Pu$_y$O$_2$,* J. Nucl. Mater. **250**, 1 (1997).

[8] R. Agarwal and S. C. Parida, *Phase Diagrams and Thermodynamic Properties of Thoria, Thoria-Urania, and Thoria-Plutonia,* in *Thoria-based Nucl. Fuels,* Green Energy and Technology, edited by D. Das and S. R. Bharadwaj (Springer London, London, 2013) pp. 71–105.

[9] F. De Bruycker, K. Boboridis, D. Manara, P. Pöml, M. Rini, and R. J. Konings, *Reassessing the melting temperature of PuO$_2$,* Mater. Today **13**, 52 (2010).

[10] C. Lombardi, L. Luzzi, E. Padovani, and F. Vettraino, *Inert matrix and thoria fuels for plutonium elimination,* Prog. Nucl. Energy **38**, 395 (2001).

[11] J. Somers, D. Papaioannou, J. McGinley, and D. Sommer, *Safety assessment of plutonium mixed oxide fuel irradiated up to 37.7 GW day tonne^{-1},* J. Nucl. Mater. **437**, 303 (2013).

[12] P. R. Hania and F. C. Klaassen, *3.04 - Thorium Oxide Fuel,* in *Compr. Nucl. Mater.,* edited by R. J. M. Konings (Elsevier, Oxford, 2012) pp. 87–108.

[13] C. Cozzo, D. Staicu, J. Somers, A. Fernandez, and R. Konings, *Thermal diffusivity and conductivity of thorium-plutonium mixed oxides,* J. Nucl. Mater. **416**, 135 (2011).

[14] *Thematic Network on Advanced Options for Partitioning and Transmutation (ADOPT),* Tech. Rep. (European Commission, 2005).

[15] *Oxide Fuels: Microstructure and Composition Variations (OMICO),* Tech. Rep. (European Commission, 2007).

[16] D. Manara, C. Ronchi, M. Sheindlin, M. Lewis, and M. Brykin, *Melting of stoichiometric and hyperstoichiometric uranium dioxide,* J. Nucl. Mater. **342**, 148 (2005).

[17] D. Manara, M. Sheindlin, W. Heinz, and C. Ronchi, *New techniques for high-temperature melting measurements in volatile refractory materials via laser surface heating,* Rev. Sci. Instrum. **79**, 113901 (2008).

7

[18] C. Ronchi and J.-P. Hiernaut, *Experimental measurement of pre-melting and melting of thorium dioxide,* J. Alloys Compd. **240**, 179 (1996).

[19] F. De Bruycker, K. Boboridis, P. Pöml, R. Eloirdi, R. Konings, and D. Manara, *The melting behaviour of plutonium dioxide: A laser-heating study,* J. Nucl. Mater. **416**, 166 (2011).

[20] R. Böhler, M. J. Welland, F. D. Bruycker, K. Boboridis, A. Janssen, R. Eloirdi, R. J. M. Konings, and D. Manara, *Revisiting the melting temperature of NpO_2 and the challenges associated with high temperature actinide compound measurements,* J. Appl. Phys. **111**, 113501 (2012).

[21] G. Begun, R. Haire, W. Wilmarth, and J. Peterson, *Raman spectra of some actinide dioxides and of EuF_2,* J. Less Common Met. **162**, 129 (1990).

[22] L. Desgranges, G. Baldinozzi, P. Simon, G. Guimbretière, and A. Canizares, *Raman spectrum of U_4O_9: a new interpretation of damage lines in UO_2,* J. Raman Spectrosc. **43**, 455 (2012).

[23] M. J. Sarsfield, R. J. Taylor, C. Puxley, and H. M. Steele, *Raman spectroscopy of plutonium dioxide and related materials,* J. Nucl. Mater. **427**, 333 (2012).

[24] S. Hubert, J. Purans, G. Heisbourg, P. Moisy, and N. Dacheux, *Local structure of actinide dioxide solid solutions $Th_{1-x}U_xO_2$ and $Th_{1-x}Pu_xO_2$,* Inorg. Chem. **45**, 3887 (2006).

[25] I. Chang and S. Mitra, *Application of a Modified Random-Element-Isodisplacement Model to Long-Wavelength Optic Phonons of Mixed Crystals,* Phys. Rev. **172**, 924 (1968).

[26] J. M. Haschke, T. H. Allen, and L. A. Morales, *Reaction of Plutonium Dioxide with Water: Formation and Properties of PuO_{2+x},* Science (80-.). **287**, 285 (2000).

[27] T. Truphémus, R. C. Belin, J.-C. Richaud, M. Reynaud, M.-A. Martinez, I. Félines, A. Arredondo, A. Miard, T. Dubois, F. Adenot, and J. Rogez, *Structural studies of the phase separation in the UO_2-PuO_2-Pu_2O_3 ternary system,* J. Nucl. Mater. **432**, 378 (2013).

[28] C. Sari, U. Benedict, and H. Blank, *A study of the ternary system UO_2-PuO_2-Pu_2O_3,* J. Nucl. Mater. **35**, 267 (1970).

[29] M. Kato, K. Morimoto, H. Sugata, K. Konashi, M. Kashimura, and T. Abe, *Solidus and liquidus temperatures in the UO_2-PuO_2 system,* J. Nucl. Mater. **373**, 237 (2008).

[30] R. J. M. Konings, O. Beneš, A. Kovács, D. Manara, D. Sedmidubský, L. Gorokhov, V. S. Iorish, V. Yungman, E. Shenyavskaya, and E. Osina, *The Thermodynamic Properties of the f-Elements and their Compounds. Part 2. The Lanthanide and Actinide Oxides,* J. Phys. Chem. Ref. Data **43**, 013101 (2014).

7

[31] C. Guéneau, N. Dupin, B. Sundman, C. Martial, J.-C. Dumas, S. Gossé, S. Chatain, F. D. Bruycker, D. Manara, and R. J. Konings, *Thermodynamic modelling of advanced oxide and carbide nuclear fuels: Description of the U-Pu-O-C systems*, J. Nucl. Mater. **419**, 145 (2011).

[32] A. Pelton and W. Thompson, *Phase diagrams*, Prog. Solid State Chem. **10**, 119 (1975).

7

Summary & Conclusions

We have found it of paramount importance that in order to progress we must recognize the ignorance and leave room for doubt. Scientific knowledge is a body of statements of varying degrees of certainty - some most unsure, some nearly sure, none certain.

Richard P. Feynman [1]

A thorough knowledge of the actinide oxides' material properties is essential for their safe application and handling. Actinide dioxides have been used and are going to be used mainly as fuel material in nuclear reactors, and therefore require extensive characterisation for understanding and controlling their behaviour during reactor operation.

This work provides new data on the material properties of the unirradiated state in a laboratory environment. The main goal was to improve and extend available high temperature phase diagram data of actinide dioxides and their mixed systems. This was achieved by performing fast laser melting experiments together with complementary material analysis to investigate composition and stoichiometry.

Actinide dioxides show in their pure, stoichiometric form, no phase changes until reaching the melting transition temperature according to their temperature - composition phase diagrams. This transition was already the subject of research in the past. In contrast to furnace techniques, the applied laser heating allowed experiments in, so called, quasi - containerless conditions, which revealed melting temperatures for several pure actinide dioxides up to several hundreds kelvin higher than previously reported.

The material was usually pressed to small thin pellets which were mounted with screws in a sample holder positioned in an autoclave. The latter was mounted inside a glove box, while the heating and temperature measurement apparatus were mounted outside of the glove box. A laser (up to 4.5 kW at 1064 nm wavelength) was used to heat up the samples and melt them on the surface with short high power pulses. The radiance temperature on the same surface spot was measured in-situ by a pyrometer calibrated for this high temperature range. A spectral analysis and surface emissivity measurements were conducted by means of an multichannel spectrometer. The phase change temperatures were determined by the thermal arrests in the temperature vs. time curves and by assistance of a low power reflected light signal.

The material was further analysed to investigate possible changes related to the melting process. Surface analysis was performed using Scanning Electron Microscopy, Energy Dispersive X-ray spectroscopy and Raman spectroscopy. X-ray Diffraction and X-ray Absorption Near Edge Structure on powder material were used as bulk analysis methods. Phase-field simulations of the melting experiments helped to get an better insight into the very fast processes taking place in the material during the heating and cooling stages, and distinguish them.

---

[1] "What do you care what other people think?": further adventures of a curious character (1988)

SUMMARY OF RESULTS

Applying new heating schemes allowed multiple experiments to be performed on same sample surfaces, allowing the check of the repeatability, and hence, improving the statistical analysis of the results of materials with limited availability. The influence of parameters of the laser heating setup, such as heating time and buffer gas, were extensively tested for the case of CaO and showed an effect of an oxidising (melting point at 3222 K ± 25 K) and reducing (3192 K ± 40 K) atmospheres. Moreover, the quasi-containerless laser heating technique was used in the case of CaO to confirm its high temperature melting point and simultaneously pointing out advantages compared to other heating methods.

By measuring the melting point of NpO_2 with the laser melting technique, the trend in melting temperature of all stable pure actinide dioxide compounds at standard conditions was verified. The melting temperature for NpO_2 was measured at 3070 K ± 62 K, which is more than 200 K higher than the previously published values. Within the context of this thesis, the pure dioxides ThO_2, UO_2 and PuO_2 were also re-measured, confirming earlier literature values obtained with this method. Further measurements on other actinide dioxides (AmO_2, CmO_2, PaO_2) would require major changes of the current setup because of their very limited availability, higher radioactivity, and poor chemical stability, i.e., decomposition would probably occur before melting.

However, using Lindemann's melting rule, an extrapolation from the already measured melting temperatures to unknown ones was performed using known structural properties in the materials. By relating the melting point to the force constant of the metal-oxygen bond in the actinide dioxides, one can derive the melting points of AmO_2 to approximately 3000 K, PaO_2 at about 3043 K, and show a general trend of a lowering of the melting temperature towards CmO_2.

As actinide dioxides are also often applied in mixed forms, different mixed actinide dioxides were subsequently investigated in this study. They form a solid solution and, hence, should be ideally represented by a pseudo binary phase diagram with continuous liquidus and solidus temperatures, a minimum melting temperature was found for $(U, Pu)O_2$, $(U, Th)O_2$ and $(Pu, Th)O_2$ mixed systems. This minimum temperature was already predicted in a laser heating study for the high plutonia part of the $(U, Pu)O_2$ system, and in traditional thermal analysis study for $(U, Th)O_2$. The minimum found for $(Pu, Th)O_2$ confirmed a similarity between these systems.

Phase diagram calculations showed for $(Pu, Th)O_2$, $(U, Th)O_2$ and in more details for $(U, Pu)O_2$ that the assumption of a stoichiometric pseudo binary system may not fully cover the results obtained by laser heating experiments. It is more appropriate to consider a non-stoichiometric section in the ternary metal-metal-oxygen system at high temperatures. For the other two mixed systems the non-ideality was shown with simpler thermodynamic simulation approach. This is also in line with other phase diagram assessments for the binary actinide oxide systems, which all tend to have a congruent melting point at a slightly hypo - stoichiometric composition.

The post-test material analysis, which was performed on the actinide oxides, has not revealed any significant sign of oxidation or reduction caused by melting experiments, although Raman spectroscopy showed peaks of a disordered lattice on the surface of some mixed systems. Even precise measurements of the lattice with XANES did not evidence a change in stoichiometry. Since none of the characterisation methods can be

performed in-situ at high temperature, it is probable that disorder changes occur during quenching to room temperature. The quenching was fast enough to show segregation in the mixed dioxides. This phenomenon was found to be more pronounced when the difference of melting points was larger (none in $(U, Pu)O_2$, very little in $(U, Th)O_2$ and little in $(Pu, Th)O_2$).

EVALUATION OF THE CURRENT RESULTS

Knowing the problematic chemical stability of the investigated refractory materials at high temperature, the application of containerless laser heating, compared to more traditional thermal analysis methods, made a more accurate melting point determination possible. The high repeatability of the measurements and the results of the material characterisation prove that this experimental approach is a suitable method to determine high temperature data for refractory oxides.

The differences to previous work is directly related to the different oxygen potentials of the investigated materials. The fast and quasi containerless characteristic of the laser heating experiments brings large advantages, since the oxygen potential defines the stability and the reactivity of the material with its environment. The pure dioxides show a bigger gap between new and old melting point results with an increase in the oxygen potential of the respective material. In this context it is not surprising that the melting point found for NpO_2 is higher compared to more traditional heating methods.

This dependence on the oxygen potential was also observed for the mixed actinide dioxides. The measured phase change temperature followed the ideal behaviour closely in materials with a high content of ThO_2, the most stable dioxide with the lowest oxygen potential. When introducing another dioxide in the solution (tested here with U and Pu), the temperature sinks to a minimum around 5 mol% ThO_2 content. For $(U, Pu)O_2$, for which the oxygen potentials of the end-members are closer to each other, the minimum is found to be very shallow between 40 and 70 mol% PuO_2 content. The minimum in the melting temperatures is therefore probably related to the relatively high oxygen potential of one of the end members. Neither an influence of the differences in ionic radii, nor a systematic influence on the melting temperature due to a difference in valence states was found. An increase of the difference of the melting temperature of the end members, however, fosters the appearance of segregation effects.

Therefore, it is crucial for high temperatures studies reaching melting and above, to control the oxygen potential. For further analysis of the actinide dioxides with a low stability and high oxygen potential, the current setup may not be sufficient to control all theses parameters. Application of high pressure in the measurement autoclave may help stabilise compounds at high temperatures, and may provide new experimental results.

Even with a much more sophisticated melting experiment, doubts and uncertainties will probably remain as a consequence of the complicated nature of the actinides and the extreme environmental conditions. An improvement in the quality of the results can only be achieved with the assistance of numerical simulation methods as it was already performed in parts of this study. The experimental data obtained in this work are essential as input parameters for assessing the phase diagrams with numerical tools such as CALPHAD. At the same time, these methods can contribute to a huge extent to the interpretation of experimental results at high temperature, as it was shown in this work for the mixed oxides. Further improvements on the melting setup and procedure can be

realised with other complementary simulations based on the the phase-field model. By simulating the complete melting experiment, the method was shown to be an adequate tool to describe phase changes. Simple models already give an insight into the processes and allow to adapt the experimental procedure. Complicated model adaptations are however necessary in order to cover the melting process of actinide compounds better. Additionally, the uncertainty of the measurements can be lowered with improvements on the detection techniques, namely with a direct measurement of the emissivity. It was also not possible to identify in the thermal analysis of the melting experiments consistent signs for liquidus phase transitions. The resolution of the pyrometers, as well as the speed in the current approach, may not be suitable to identify such effects with the present ceramic materials. A combination of tests on fully characterised materials with simulation techniques may be necessary to optimise the current approach.

Furthermore, the material analysis needs to be improved for proper stoichiometry determinations. Newer methods as high resolution X-ray absorption spectroscopy may give a better insight into the material behaviour by allowing a better distinction between the different valence states of the cations. Nevertheless, a first characterisation by Raman spectroscopy of some mixed actinide dioxides was successfully performed within this work. It was shown that Raman spectroscopy is sensitive enough to detect different compositions and possible changes in stoichiometry. But the spectra of the actinide dioxides are still not completely understood. Several peaks could not yet be assigned. Spectroscopic analysis of pure and mixed actinides has to be continued to reveal the origin of these peaks.

SIGNIFICANCE OF THE CURRENT RESULTS

The impact on nuclear reactor fuels is evident for accidental high temperature conditions, as can occur during power transients, during which the melting temperature can be reached:

- Possible future applications of fuels, such as mixed uranium-plutonium dioxides with a higher plutonia content, need to take the non-ideal behaviour into consideration. However, in this study no evidence was found for phase separation from the liquid phase in this system.

- Thorium-based fuels can be used in existing and future reactors. The current findings show that only in cases with low amounts of thoria the melting temperature deviates from ideal behaviour. But mixed thoria fuels seem to have a greater likelihood of separation from the liquid. This is important for the analysis of accident situations in which fuel melting takes place.

- The presence of transuranium elements in an fuel will have a smaller impact on the melting temperature of the fuel than it was assumed before due to higher melting temperatures measured for several actinide oxides in this work.

- This study presented extensively the potential of the laser melting approach combined with different material characterisation methods as a way to investigate high temperature phase changes for challenging materials.

Finally, the physicochemical properties presented in this work constitute an important step in the understanding of actinide dioxides' behaviour at high temperatures.

SAMENVATTING & CONCLUSIE

EEN grondige kennis van de materiaaleigenschappen van de actinidenoxiden is essentieël voor het hanteren en veilig toepassen van deze verbindingen. Actinidenoxiden worden voornamelijk gebruikt of zullen worden gebruikt als splijtstof in nucleaire reactoren, en moeten uitvoerig worden gekarakteriseerd om hun gedrag tijdens het bedrijf van reactoren te begrijpen en te controleren.

Het werk dat in dit proefschrift wordt beschreven levert nieuwe gegevens over de eigenschappen van de onbestraalde materialen in een laboratoriumomgeving. Het hoofddoel was het verbeteren van de beschikbare gegevens over de hoge-temperatuur fasediagrammen van de actinidendioxiden en hun mengsels. Dit is gerealiseerd door middel van snelle laser smelt experimenten en aanvullende analyses met het doel de samenstelling en stoichiometrie te bepalen.

In hun zuivere stoichiometrische vorm vertonen de actinidedioxiden geen faseveranderingen tot hun smeltpunt, zoals uit de temperatuur-samenstelling fasediagrammen kan worden afgeleid. De smeltovergang is al in het verleden onderzocht. In tegenstelling tot analyses met behulp van ovens, staat de toegepaste laser techniek toe dat de experimenten worden uitgevoerd onder zogenaamde "quasi-houderlozeömstandigheden, die hebben aangetoond dat de smeltpunten van enkele zuivere actinidendioxiden enkele honderden Kelvin hoger zijn dan de resultaten van vroegere werken.

Het bestudeerde materiaal voor de experimenten was in de vorm van tabletten die met behulp van schroeven in de monsterhouder in een autoclaaf werden gemonteerd. Die laatste was in een handschoenenkast opgesteld, terwijl de apparatuur voor het verhitten en de temperatuurmeting buiten de handschoenenkast was opgesteld. Een laser (met een vermogen to 4.5 kW en een golflengte van 1064.5 nm) werd gebruikt voor het verhitten van het oppervlak van de monsters door middel van korte hoogvermogen pulsen. De stralingtemperatuur (radiance temperature) van dezelfde plek op het oppervlak werd gemeten met behulp van een pyrometer die gekalibreerd was voor het betreffende temperatuurgebied. Een spectrale analyse en de oppervlakte-emissiviteit werd met behulp van een multikanaal spectrometer. De faseveranderingen werden gemeten als een thermisch plateau in het temperatuur-tijd signaal, en met behulp van het gereflecteerde signaal van een laagvermogen laser.

Het materiaal werd daarna geanalyseerd om bepalen of er veranderingen plaats hadden gevonden als gevolg van het het smelten. Het oppervlakte van de tabletten werd geanalyseerd met Rasterelectronenmicroscopie (SEM), Energy Dispersieve Röntgenspectroscopie (EDX) en Raman spectroscopie. Voor bulkanalyse werden Röntgendiffractie en Röntgenabsorptie near edge structuur spectroscopie uitgevoerd aan poeder. Phase-field simulaties van de smeltexperimenten werden toegepast om een beter begrip te krijgen van de zeer snelle processen die tijdens het opwarmen en afkoelen plaatsvonden, en om deze te onderscheiden.

Door het toepassen van nieuwe opwarmschemas en procedures werd het mogelijk om meerdere experimenten op hetzelfde monsteroppervlak uit te voeren, waarmee de reproduceerbaarheid kon worden onderzocht en dus de statische analyse kon worden verbeterd wat van belang is voor materialen die slecht beperkt beschikbaar zijn. De invloed van parameters van de experimentele opstelling, zoals de opwarmtijd en het buffergas, werden uitvoerig onderzocht voor CaO en toonden het verschil tussen een oxyderend (smeltpunt 3225 ± 25 K) en een reducerend buffergas (3192 ± 40 K). De „quasihouderloze" laser techniek kon dus worden toegepast om het hoge smeltpunt van CaO te bevestigen en de voordelen ten opzichte van andere technieken duidelijk te maken.

Door het meten van het smeltpunt van NpO_2 met de lasertechniek kon de trend in de smeltpunten van de alle stabiele zuivere actinidedioxiden onder standaard omstandigheden worden geverifieerd. Het smeltpunt van NpO_2 werd bepaald als 3070 ± 62 K meer dan 200 K hoger dan de resultaten uit het verleden. In samenhang met dit werk werden ook de smeltpunten van ThO_2, UO_2 en PuO_2 opnieuw gemeten, en konden de eerdere resultaten worden bevestigd die met dezelfde techniek waren verkregen. Meting aan andere actinidedioxiden (PaO_2, AmO_2, CmO_2) zouden ingrijpende verandering van de opstelling vereisen met het oog op de geringe hoeveelheden die beschikbaar zijn, de sterke radioactieve straling, en de beperkte chemische stabiliteit i.e. dissociatie zal waarschijnlijk optreden voor het smelten.

Met behulp van Lindemann's smeltregel konden echter de onbekende smeltpunten worden geëxtrapoleerd op basis van bekende structuureigenschappen van de materialen. Door het smeltpunt te correleren met de krachtkonstante van de metaal-zuurstof binding in de actinidedioxiden kon het smeltpunt van AmO_2 worden afgeleid als ongeveer 3000 K, en dat van PaO_2 als ongeveer 3043 K, waarbij de trend in de verlaging van het smeltpunt in de rij ThO_2-CmO_2 duidelijk werd.

Omdat actinideoxiden ook veel worden ingezet als mengsels, werden diverse mengoxiden onderzocht in het kader van deze studie. Alhoewel deze mengoxiden vaste oplossingen vormen en in het ideale geval als pseudo-binaire fasediagrammen kunnen worden gezien met geleidelijke toename van de solidus en liquidus temperaturen, werd een minimum gevonden in de $(U,Pu)O_2$, $(U,Th)O_2$, en $(Pu,Th)O_2$ mengsystemen. Dit minimum was al voorspeld in een eerdere studie met de lasertechniek aan samenstelling met een hoge PuO_2 concentratie, en in een traditionele thermische analyse studie voor $(U,Th)O_2$. Het minimum dat voor het $(Pu,Th)O_2$ werd gevonden bevestigde de overeenkomsten tussen deze systemen.

Fasediagramberekeningen voor $(Pu,Th)O_2$, $(U,Th)O_2$ en in detail voor $(U,Pu)O_2$ toonden aan dat de aanname van een pseudo-binair stoichiometrisch system niet volledig met de experimentele gegevens met de lasertechniek in overeenstemming is. Het lijkt beter om bij hoge temperaturen een niet-stoichiometrische doorsnede in het ternaire metaal - metaal - zuurstof systeem te beschouwen. Dit stemt overeen met de fasediagram evaluaties voor de binaire actinide - zuurstof systemen, die allemaal een congruent smeltpunt tonen voor licht onderstoichiometrische samenstelling.

De analyse van de actinidedioxiden na de experimenten toonde geen bewijs voor oxidatie of reductie als gevolg van de smeltexperimenten, hoewel enkele pieken in de Raman spectroscopie aanwijzing gaf voor wanorde in de kristalstructuur aan het oppervlak

van sommige mengoxiden. Zelfs nauwkeurige XANES metingen lieten geen veranderingen in de stoichiometrie zien. Aangezien geen enkele van de karakteriseringsmethoden in-situ bij hoge temperatuur kon worden uitgevoerd, ligt het voor de hand te veronderstellen dat de wanorde ontstaat tijdens afkoelen naar kamer temperatuur, waarbij die (deels) wordt afgeschrikt. Het afschrikken was snel genoeg om ontmenging in de mengoxiden te tonen. De resultaten toonden dat dit fenomeen duidelijker waarneembaar is wanneer het verschil in smeltpunt groter is (geen ontmenging in $(U,Pu)O_2$, zeer weinig in $(U,Th)O_2$ en weinig in $(Th,Pu)O_2$).

Evaluatie van de resultaten

Met het oog op de problematische chemische stabiliteit van de onderzochte refractaire materialen, kan worden gesteld dat de toepassing van de houderloze lasertechniek het mogelijk maakt om nauwkeurigere metingen van het smeltpunt uit te voeren, in vergelijk met tradionele thermische analyse methoden. De goede reproduceerbaarheid van de resultaten, en de resultaten van de karakterisering tonen aan dat deze methode uitermate geschikt is voor de bepaling van smeltpunten van refractaire oxiden.

Het wwargenomen verschil met eerdere studies kan worden gerelateerd aan de zuurstofpotentiaal van de onderzochte materialen. De zuurstofpotentiaal bepaalt de stabilitiet en reactiviteit van het materiaal met zijn omgeving en de snelle quasi-houderloze laser techniek heeft in dat opzicht grote voordelen aangezien de interactie sterk wordt beperkt. De zuivere dioxiden laten een groter verschil zien tussen nieuwe en oude smeltpunten als de zuurstofpotentiaal toeneemt. In dat opzicht is het niet verwonderlijk dat het smeltpunt van NpO_2 hoger is dan de meting met traditionele thermische analysetechniek.

De afhankelijkheid van de zuurstofpotentiaal werd ook bij de mengoxiden waargenomen. De gemeten faseovergang was in goede overeenstemming met het ideal gedrag in materialen met een hoge ThO_2 concentratie, het meest stabiele dioxide met de laagste zuurstofpotentiaal. Wanneer een ander dioxide in de vaste lossing werd geïntroduceerd (in dit geval voor U and Pu) daalt de temperatuur tot een minimum by ongeveer 5% ThO_2. Voor $(U,Pu)O_2$, waarbij de zuurstofpotentiaal van de eindleden veel dichter bij elkaar liggen, werd een zeer vlak miminum tussen 40 en 70% PuO_2 gevonden. Het minimum in het smeltpunt is daarom gerelateerd aan de relief hogere zuurstofpotentiaal van een van de eindleden. Geen invloed van het verschil in ionstraal of een invloed van de valentietoestand is waargenomen. Een toename van het verschil in de smeltpunten van de eindleden van de vaste oplossing leidt echter tot een toename van de ontmengingseffecten.

Daarom is het van essentieel belang bij hoge-temperatuur experimenten waarbij het smeltpunt bereikt of overschreden wordt dat de zuurstofpotentiaal wordt gecontroleerd. De huidige opstelling lijkt dan ook beperkt geschikt voor verdere analyse van actinidedioxiden met een beperkte stabiliteit en een hoge zuurstofpotentiaal door de beperkte controle van deze parameters. Toepassing van een hoge druk in de meetautoclaaf kan helpen om de verbindingen te stabiliseren bij hoge temperaturen, en kan nieuwe resultaten opleveren.

Maar zelfs met meer geavanceerd methoden voor smeltexperimenten zal twijfel en onzekerheid blijven bestaan als gevolg van de complexe natuur van de actiniden en de

extreme omstandigheden waaronder de experimenten worden uitgevoerd. Een verbetering van de kwaliteit van de resultaten kan alleen worden verkregen met de hulp van numerieke simulaties, zoals al toegepast in deze studie. De experimentele resultaten verkregen in deze studie zijn van groot belang voor de evaluatie van fasediagrammen met numerieke technieken zoals CALPHAD. Tegelijkertijd kunnen deze technieken sterk bijdragen aan de interpretatie van experimenten bij zeer hoge temperaturen, zoals in dit werk is aangetoond voor mengoxiden. Verdere verbeteringen van de smeltexperimenten kan worden verkregen met behulp van aanvullende simulaties met de fase-field methode. Door een simulatie van het complete smeltexperiment is aangetoond dat deze techniek geëigend is om faseveranderingen te beschrijven. Eenvoudige modellen kunnen al een inzicht geven in de processen en aanpassing van de experimentele aanpak. Complexe model veranderingen zijn echter nodig om het smeltgedrag van de actinideverbindingen beter te beschrijven. De onzekerheden in de metingen kunnen verder worden teruggebracht door verbeteringen van de detectietechnieken in het bijzonder de directe meting van de emissiviteit. Het was ook niet mogelijk om in de experimenten systematisch een indicatie voor de liquidus te bepalen. De resolutie van de pyrometers en de snelheid van de experimenten zou ongeschikt kunnen zijn voor het bepalen van dat effect in de bestudeerde keramische materialen. Een combinatie van experimenten aan zorgvuldig gekarakteriseerde materialen met simulatietechnieken kan noodzakelijk zijn om de huidige aanpak te optimaliseren.

Ook de materiaalanalyse moet verder verbeterd worden voor de bepaling van de stoichiometrie van de monsters. Nieuwe methoden zoals Röntgen absorptie spectroscopie kan betere resultaten opleveren door de bepaling van de valentietoestanden van de kationen in de materialen. Desalniettemin, de karakterisering met behulp van Raman spectroscopie van enkele mengoxiden is met succes toegepast in dit werk. Het is aangetoond dat Raman spectroscopie gevoelig genoeg is om verschillen in samenstelling te detecteren, en mogelijk ook veranderingen in stoichiometrie. Maar de spectra van de actinidedioxiden zijn nog onvoldoende begrepen. Diverse pieken konden nog niet worden toegekend. Spectroscopische analyse van zuivere oxiden en mengoxiden moet voortgezet worden om de oorsprong van deze pieken te ontrafelen.

BELANG VAN DE RESULTATEN

De toepassing van de resulltaten is overduidelijk voor ongevalssituaties met nucleaire splijtstoffen waarbij zeer hoge temperaturen ontstaan, bijvoorbeeld gedurende vermogensexcursies, waarbij het smeltpunt kan worden bereikt:

- Bij mogelijke toekomstige toepassingen van splijtstoffen zoals uranium-plutonium dioxiden met een hooog plutonium gehalte moet rekening worden gehouden met het niet ideaal gedrag bij hoge temperaturen. Daar staat tegenover dat er geen aanwijzing gevonden zijn voor ontmenging vanuit de vloeibare fase in dit systeem.

- Thorium splijtstoffen kunnen in bestaande en nieuwe reactor concepten worden toegepast. De resultaten uit dit proefschrift laten zien dat alleen voor lage thoriumgehalte het smeltgedrag afwijkt van ideaal, maar dat voor thoriumsplijtstof een grotere kans op ontmenging vanuit de vloeistof bestaat. Dit is van belang voor de analyse van ongevalssituaties waarbij smelten splijtstof plaatsvindt.

- De aanwezigheid van transuranium elementen in de splijtstof heeft een geringere invloed op het smeltgedrag dan tot nu toe aangenomen, als gevolg van de beduidend hogere smeltpunten voor de zuivere oxiden die in dit werk zijn verkregen.

- Dit werk heeft uitgebreid de mogelijkheden van de lasertechniek laten zien, in combinatie met verschillende karakteriseringsmethoden van de materialen, om faseveranderingen in complexe materialen bij hoge temperaturen te bepalen.

Ten slotte, de fysisch-chemische eigenschappen die in dit proefschrift zijn gepresenteerd hebben sterk bijgedragen aan een beter begrip van het gedrag van actinideoxiden bij hoge temperaturen.

Curriculum Vitæ

Robert Böhler

07-05-1983   Born in Karaganda, Kazakhstan.

Education

2010–2014   Ph.D. Material Sciences
Technische Universiteit Delft
Faculty of Applied Sciences

Thesis:	High temperature phase transitions of actinide dioxides
Promotor:	Prof. dr. H. T. Wolterbeek
	Prof. dr. R. J. M. Konings

2003–2009   Diploma in Aviation and Space Engineering
University of Stuttgart, Germany

1994–2002   High School
Kepler Gymnasium, Pforzheim, Germany

Training

2010   Traineeship
Institute for Transuranium Elements
JRC, European Commission, Karlsruhe, Germany

2006   Internship
Audi AG, Ingolstadt, Germany

2002   Social Service
Heilpädagogisches Zentrum, Pforzheim, Germany